

5-21-2024

# Geochemistry and Geochronology of the Steens and Monument Dike Swarm: Implications and Relationships to Magmatic Storage and to Lava Flows of the Picture Gorge and Steens Basalt

Rachel Anne Sweeten  
*Portland State University*

Follow this and additional works at: [https://pdxscholar.library.pdx.edu/open\\_access\\_etds](https://pdxscholar.library.pdx.edu/open_access_etds)



Part of the [Geochemistry Commons](#), and the [Geology Commons](#)

Let us know how access to this document benefits you.

---

## Recommended Citation

Sweeten, Rachel Anne, "Geochemistry and Geochronology of the Steens and Monument Dike Swarm: Implications and Relationships to Magmatic Storage and to Lava Flows of the Picture Gorge and Steens Basalt" (2024). *Dissertations and Theses*. Paper 6673.

This Thesis is brought to you for free and open access. It has been accepted for inclusion in Dissertations and Theses by an authorized administrator of PDXScholar. Please contact us if we can make this document more accessible: [pdxscholar@pdx.edu](mailto:pdxscholar@pdx.edu).

Geochemistry and Geochronology of the Steens and Monument Dike Swarm:  
Implications and Relationships to Magmatic Storage and to Lava Flows of the Picture

Gorge and Steens Basalt

by

Rachel Anne Sweeten

A thesis submitted in partial fulfillment of the  
requirements for the degree of

Master of Science  
in  
Geology

Thesis Committee:  
Martin Streck, Chair  
John Wolff  
Barry Walker

Portland State University  
2024

© 2024 Rachel Anne Sweeten

## ABSTRACT

The Columbia River Basalt Group (CRBG) is the youngest and best-preserved example of a continental flood basalt province. Vents and dikes for the four main eruptive units (Steens, Imnaha, Grande Ronde, and Picture Gorge Basalt) are the Monument, Steens and Chief Joseph Dike Swarms located in eastern Oregon, southeastern Washington, and northern Nevada.

Here we report on the compositions and timing of the dikes and sills of the Monument Dike Swarm (MDS), as well as their relationship to the subaerial lava flows of the Picture Gorge Basalt (PGB) with implications for crustal storage of these magmas. We evaluate data from 48 dikes and several small sills of this study, 21 dikes from Cahoon (2020), as well as 10 new  $^{40}\text{Ar}/^{39}\text{Ar}$  ages of select MDS dikes. With these data, we show that the age range of the Picture Gorge Basalt and the MDS span from  $17.27 \pm 0.05$  Ma to  $15.61 \pm 0.22$  Ma. These ages agree with ages determined by Cahoon et al. (2020), thus extending the temporal range of the PGB. Based on new geochronological and geochemical data (e.g., Zr vs Nb,  $\text{TiO}_2$  vs  $\text{SiO}_2$ , Y vs  $\text{TiO}_2$  and MgO vs  $\text{SiO}_2$ ) of intrusives, we propose to subdivide PGB into two compositional subunits, Twickenham and Dayville. This simplification resolves issues with ages and distribution of Cahoon et al. 2020, this study, and the stratigraphy established by Bailey, 1989.

This study also adds data of 26 newly sampled Steens Basalt dikes to existing dike data (Moore et al., 2018). We evaluate compositional relationships of these dikes to subaerial Steens Basalt flows, in part searching for evidence of crustal magma storage locations. Relevant to this, we also report on 16 samples of a newly discovered, compositionally

zoned, mafic intrusive body related to the Steens Basalt. This intrusive body is currently estimated to have a minimum area of 125 km<sup>2</sup>, with lithologies including anorthosite, leucogabbro, and troctolite. Steens Basalt dikes and others intrusives have compositions that match lava flows except in cases where crystal accumulation is likely to dictate bulk compositions. This new intrusive data acquired from both the Picture Gorge and Steens Basalt was integrated with available geochemical, geophysical, and geographic data to determine a model of Columbia River Basalt Group mid- and upper- crustal magma storage.

*Dedicated to my Dad*  
*January 19, 1963 – April 25, 2023*

## ACKNOWLEDGEMENTS

No large project is ever done alone, and as such, I would like to acknowledge the assistance and contributions from the following:

- The Geologic Society of the Oregon Country and the Bev Vogt Grant, which assisted with some of the summer field expenses, as well as Dr. Michael Cummings and the Cummings Endowed Scholarship for field expenses from the prior year.
- My graduate cohort, especially Mary Mass, and all of our discussions over beers.
- Victor Camp in aiding in locating other possible outcrops of the Streck LMI after Heather and I found our first exposure.
- My boyfriend Stuart and his endless patience with all my fieldwork, and the late nights he loses me to my research.
- My children for all their field assistance, as well as excitement about my research, and always giving me a reason to keep going no matter how hard the work is.
- Professors John Wolff, Barry Walker, and John Bershaw, and all of our discussions and postulations over beers, as well as serving on my committee.
- My trusty dusty field assistant Heather Ziff. You are a badass, and you motivated me to push harder to stay ahead of you (both for hiking/climbing, and to answer all your questions). Also, your sighting of the house sized anorthosite chunk was the key that was needed to crack the mystery of the Streck LMI location. I am so proud and honored to have gotten to share the experience of that discovery with

you! The adventures and memories we built over the past few years of fieldwork are some of the best memories of my life.

- And last, but certainly not least, my advisor, Professor Martin Johannes Streck. You gave me the chance and opportunity to seize my dreams, and you always believed in me, even when my arm waving was driving you a little nuts. Your support and mentoring has made me the scientist I am today, and I wouldn't be where I am without you. It has been my greatest honor to have been working with you these past few years, and I am looking forward to our adventures on my PhD.

Thank all of you for your hard work and contribution to the following work!

# TABLE OF CONTENTS

ABSTRACT .....	I
ACKNOWLEDGEMENTS .....	IV
LIST OF TABLES .....	VIII
LIST OF FIGURES .....	IX
INTRODUCTION .....	1
<b>BACKGROUND</b> .....	2
<b>GEOLOGIC CONTEXT OF THE CRBG</b> .....	6
<b>PALEOZOIC AND MESOZOIC TERRANES:</b> .....	7
<i>Wallowa Terrane</i> .....	7
<i>Baker Terrane</i> .....	7
<i>Izee Terrane</i> .....	7
<i>Olds Ferry Terrane</i> .....	8
<i>Black Rock-Jackson Terrane</i> .....	8
<b>JOHN DAY-CLARNO ERUPTIONS</b> .....	10
<b>COLUMBIA RIVER RHYOLITES</b> .....	12
<b>REGIONAL TECTONICS</b> .....	14
<b>MONUMENT DIKE SWARM/PICTURE GORGE BASALT</b> .....	18
<b>STEENS DIKE SWARM/STEENS BASALT</b> .....	22
<b>METHODS</b> .....	<b>27</b>
<b>FIELD WORK</b> .....	27
<b>PETROGRAPHY</b> .....	28
<b>GEOCHEMISTRY</b> .....	28
<b>GEOCHRONOLOGY</b> .....	29
<b>GEOCHEMICAL MODELING</b> .....	31
<b>RESULTS</b> .....	<b>33</b>
<b>CLASSIFICATION</b> .....	33
<b>MONUMENT DIKE SWARM</b> .....	33
<b>STEENS DIKE SWARM</b> .....	34
<b>GEOCHEMISTRY</b> .....	35
<b>MONUMENT DIKE SWARM</b> .....	35
<b>STEENS DIKE SWARM</b> .....	45
<b>GEOCHRONOLOGY</b> .....	53
<b>FIELD</b> .....	54
<b>MONUMENT DIKE SWARM</b> .....	54
<b>STEENS DIKE SWARM</b> .....	61
<b>PETROGRAPHY</b> .....	68
<b>MONUMENT DIKE SWARM</b> .....	68
<b>STEENS DIKE SWARM</b> .....	72
<b>STRECK LAYERED MAFIC INTRUSION</b> .....	73
<b>DISCUSSION</b> .....	<b>76</b>
<b>PICTURE GORGE BASALT/MONUMENT DIKE SWARM</b> .....	76

<i>CLASSIFICATION, GEOCHEMISTRY, AND GEOCHRONOLOGY</i> .....	76
<i>Twickenham Trend</i> .....	83
<i>Dayville Trend</i> .....	86
<b>STEENS BASALT/STEEN DIKE SWARM</b> .....	88
<i>CLASSIFICATION AND GEOCHEMISTRY</i> .....	88
<b>REGIONAL CONTEXT</b> .....	92
<i>IMNAHA - PICTURE GORGE GEOCHEMICAL RELATIONSHIP</i> .....	92
<i>STEENS – PICTURE GORGE GEOCHEMICAL RELATIONSHIPS</i> .....	98
<b>MAGMA STORAGE AND TRANSPORT</b> .....	104
<b>CONCLUSION</b> .....	<b>113</b>
<b>WORKS CITED</b> .....	<b>115</b>
<b>APPENDIX</b> .....	<b>131</b>

## LIST OF TABLES

Table 1: Calculated accuracies and distribution of subunit classification using a random forest machine learning model.....	33
Table 2: Calculated accuracies and distribution of flow member classification using the tree machine learning model.....	34
Table 3: Calculated accuracies and subunit distribution of Steens samples using the random forest machine learning model.....	35
Table 4: Calculated accuracies and flow member distribution of Steens samples using the random forest machine learning model.....	35
Table 5: Geochronology results from Monument Dike Swarm samples. ....	53
Table 6: Partition coefficients of selected trace elements compiled from McKenzie and O’Nions (1991); Hart and Dunn (1993); Green (1994); Dunn and Sen (1994). ...	90

## LIST OF FIGURES

Figure 1: Map and Stratigraphy of Columbia River Basalt Group Deposits:.....	5
Figure 2: Terrane boundaries of eastern Oregon, northern Nevada, and western Idaho. ....	9
Figure 3: Map of John Day and Clarno volcanic deposits:.....	11
Figure 4: Map of co-eval mid-Miocene felsic volcanic deposits of Streck et al., (2023). 13	
Figure 5: Map of normal and oblique faults in the Pacific Northwest. ....	16
Figure 6: Map of major linear aeromagnetic, fault, and gravity lineaments.....	17
Figure 7: Map of sampled Monument Dike Swarm dikes.....	21
Figure 8: Dike map of historical and sampled dikes of this study of the Steens Dike Swarm (SDS). ....	26
Figure 9: Part of the Total alkali-silica diagram (Le Bas et al., 1986). ....	38
Figure 10: Incompatible element and REE diagrams of Monument Dikes.....	39
Figure 11: Plots of major element vs. SiO <sub>2</sub> wt. % of Picture Gorge Basalt and Monument dike samples. ....	40
Figure 12: Plots of major element vs MgO wt. % of Picture Gorge Basalt and Monument dike samples. ....	41
Figure 13: Plots of compatible and incompatible trace element vs. SiO <sub>2</sub> of Picture Gorge Basalt and Monument dike samples ....	42
Figure 14: Plots of trace element vs. TiO <sub>2</sub> of Picture Gorge Basalt and Monument dike samples ....	43
Figure 15: Plots of incompatible trace element vs SiO <sub>2</sub> of Picture Gorge Basalt and Monument dike samples.....	44
Figure 16: Part of the Total alkali-silica diagram (Le Bas et al., 1986). ....	47
Figure 17: Trace and REE element diagrams of Steens dikes. ....	48

Figure 18: Plots of major element vs. SiO <sub>2</sub> wt. % of Steens Basalt and dike samples.....	49
Figure 19: Plots of Major element vs MgO wt. % of Steens Basalt and dike samples. ....	50
Figure 20: Plots of compatible and incompatible trace element vs. SiO <sub>2</sub> of Steens Basalt and dike samples. ....	51
Figure 21: Plots of incompatible trace element vs SiO <sub>2</sub> of Steens Basalt and dike samples. ....	52
Figure 22: Map of the MDS field area, with geologic context. ....	55
Figure 23: Subunit width distribution for sampled Monument Dikes.....	57
Figure 24: Rose diagram and distribution of sampled MDS dike strikes.....	58
Figure 25: Monument dikes in situ.....	60
Figure 26: Map of Steens Dike Swarm field area. ....	62
Figure 27: Rose diagram and distribution of strike and width of sampled Steens Dikes. .	64
Figure 28: Steens dikes, in situ.....	65
Figure 29: The Streck layered mafic intrusion.....	66
Figure 30: Google Earth view of the Streck LMI. ....	67
Figure 31: Petrographic images of fine grained, coarse grained, and porphyritic MDS samples. ....	71
Figure 32: Petrographic images of select Steens dikes.....	73
Figure 33: Petrographic images of select Streck LMI samples.....	75
Figure 34: Elemental comparison diagrams of Twickenham, and Dayville trends. ....	80
Figure 35: Total alkali-silica diagram (Le Bas et al., 1986) of PGB samples using new subunit classification.....	81
Figure 36: Element vs Age diagrams using revised subunit classification.....	82
Figure 37: MELTS modelling of Steens Basalt. ....	91

Figure 38: Ba/Nb and Ba/Zr vs SiO <sub>2</sub> comparison diagram of Picture Gorge and Innaha Basalt.....	95
Figure 39: Ba/Zr vs SiO <sub>2</sub> comparison diagram of Picture Gorge and Innaha Basalt. ....	96
Figure 40: Geographic distribution of Ba/Nb ratios of primitive main phase Columbia River Basalt lavas and intrusives.....	97
Figure 41: Zr/Y and La/Nb vs SiO <sub>2</sub> comparison diagram of Steens and Picture Gorge Basalt.....	101
Figure 42: Th/Yb vs SiO <sub>2</sub> and Ba/Nb vs La/Yb comparison diagram of Steens and Picture Gorge Basalt. ....	102
Figure 43: Geographic distribution of Zr/Y ratios of primitive main phase Columbia River Basalt lavas and intrusives.....	103
Figure 44: Regional mid- and upper- crustal storage locations for CRBG magmas.....	110

## INTRODUCTION

The Columbia River Basalt Group (CRBG) (Figure 1) is the youngest example of a large igneous province (LIP), and as such is exquisitely preserved compared to other LIP's. Furthermore, differential faulting and uplift throughout this province provide an unique opportunity to sample and analyze the internal geometry, geochemistry, and magma transport of this young LIP. Eruptions of the CRBG lavas began 17.23 Ma (Cahoon et al., 2020) and activity continued to 6 Ma (Carson and Pogue, 1996), with the bulk of the activity occurring within the first million years (main phase). These main phase units are the Picture Gorge, Steens, Imnaha, and Grande Ronde basalts and basaltic andesites. The CRBG is considered by many workers to be the result of re-emergence of the Yellowstone Hotspot (YH) plume on the North American continent. Vents and dikes for the four main eruptive units (main phase, Figure 1) are located within northern Nevada, eastern and northeastern Oregon, and eastern Washington, and are the Steens, Monument, and Chief Joseph Dike Swarms (SDS, MDS, CJDS, respectively). Basaltic and basaltic andesite eruptions began in the MDS and SDS, as the Picture Gorge and Steens Basalt, respectively, with later eruptions focused on the CJDS, roughly following the suture of accreted terranes with Precambrian craton. Subsequently, the plume tail moved relatively northeast creating the Snake River Plain-Yellowstone (SRP-Y) hotspot track. The degree of spatial separation between these dike swarms raises the question as to whether they represent discrete, semi-localized magma storage locations in the crust or rather was there one central storage location with lateral transport occurring in dikes along pre-existing structures.

This study will have several foci. We compositionally classify dikes and other intrusive units sampled in this study by main phase unit and geochemical subunit where applicable. We use new geochemical and radiometric age data to investigate possible geographic trends. And finally, we connect field observations and dike compositions with available geophysical data to determine potential locations for magma storage for both the MDS and SDS feeder dike systems.

## **BACKGROUND**

The most voluminous basalt eruptions in the geologic record are generated by Large Igneous Provinces (LIPs) that occur in both oceanic and continental intraplate settings (Sheth 2007). These are characterized by voluminous deposits ( $>100,000 \text{ km}^3$ ) of basalt and basaltic andesites that are emplaced within a relatively short amount of time (often  $<1,000,000$  years) and are associated with continental rifting or adiabatic rise of mantle plumes (Sheth 2007; Camp and Hanan, 2008). These qualifications, namely eruptive volume and eruptive rate, firmly places the Columbia River Basalt Group within the LIP category. Along with voluminous basaltic eruptions, there are abundant co-eval rhyolitic provinces throughout eastern Oregon, northern Nevada, and western Idaho. Recent research has shown a broad, 300-400 km diameter, co-eval footprint of felsic eruptions centered on a location near the Oregon-Idaho Graben (Coble and Mahood, 2016; Streck et al., 2023), indicating that the CRBG LIP is a strongly bimodal LIP, with crustal melts being generated and erupting in response to the intrusion of voluminous basalt magmas associated with the impingement of the Yellowstone Hotspot (YH) mantle plume (Streck et al., 2023). As a bimodal LIP, the Columbia River Basalt Group (CRBG) is most

accurately classified as a Large Basaltic-Rhyolitic Province (LBRP), following the LIP classification system of Sheth, 2007. Of these LBRP's, the Columbia River Basalt Group (CRBG) represents the youngest known, and best preserved, continental flood basalt, with differential faulting and uplift in eastern Oregon, southeastern Washington and northwestern Nevada exposing the entirety of the stratigraphy of the flows (Camp and Hanan, 2008).

The CRBG eruptions extruded an estimated lava volume of 220,500 km<sup>3</sup> (Reidel et al., 2013) of basalt to basaltic andesite, with 99% of the total volume erupted between 17.2-15.8 Ma. This is considered the “main phase” of the CRBGs and comprises the Picture Gorge, Steens, Innaha, Grande Ronde, and Wanapum Basalts (Figure 1). These lavas were likely sourced from 3 major dike swarms: the Monument Dike Swarm (MDS), associated with the Picture Gorge Basalts; the Steens Dike Swarm (SDS), associated with the Steens Basalt; and the Chief Joseph Dike Swarm (CJDS), associated with the Innaha, Grande Ronde, and Wanapum Basalt, as well as the younger CRBG formations. These dike swarms were emplaced in eastern Oregon (MDS, SDS, and CJDS), southeastern Washington (CJDS), and northwestern Nevada (SDS). The co-eval northern Nevada Rift intrusives of north and central Nevada are also believed by some workers to be a result of YH emergence on the North American continent (e.g., Zoback et al., 1994; Ponce and Glen, 2001; Ponce and Glen 2002; Camp and Wells, 2021). Most workers agree that this continental flood basalt is associated with the interactions of the YH on the North American continent in a back arc extensional environment (e.g., Camp and Ross 2004; Camp et al. 2008; Wolff et al., 2008; Camp et al. 2013; Cahoon et al. 2020; Moore et al.,

2020). While plume models show that the most intense activity is above the plume tail, impingement of the hotspot at the base of the lithosphere and subsequent spreading can initiate volcanism over a much larger extent (Hill et al. 1992; Thomas, 2007). New data suggest that eruptions initiated within the MDS at 17.2Ma producing the Picture Gorge Basalts (Cahoon et al., 2020) followed closely by the SDS at 16.9-16.6 Ma that produced the Steens Basalts (Camp et al., 2013; Moore et al., 2020), rapidly followed by eruptions from the CJDS at 16.6-15.8 Ma to produce the Imnaha, Grande Ronde, and Wanapum Basalts (Camp et al. 2013). Distribution of the CJDS suggests that this phase of dike emplacement exploited the suture between the North American craton and “exotic” terranes to the west (Camp et al., 2013). To the south and east of the CJDS the CRBG activity is represented by the Santa Rosa-Calico volcanic field as well as the intrusions and basaltic eruptions of the northern Nevada rift (Zoback et al., 1994; Ponce and Glen, 2001; Ponce and Glen, 2002; Breuseke et al., 2007; Camp and Wells 2021). During the waning phase of emplacement, eruptions were sourced from the northernmost CJDS, producing the Saddle Mountain Basalt between 15.9-6 Ma (Carson and Pogue, 1996). This study will focus primarily upon the earliest of the main phase dike swarms, the MDS and SDS.

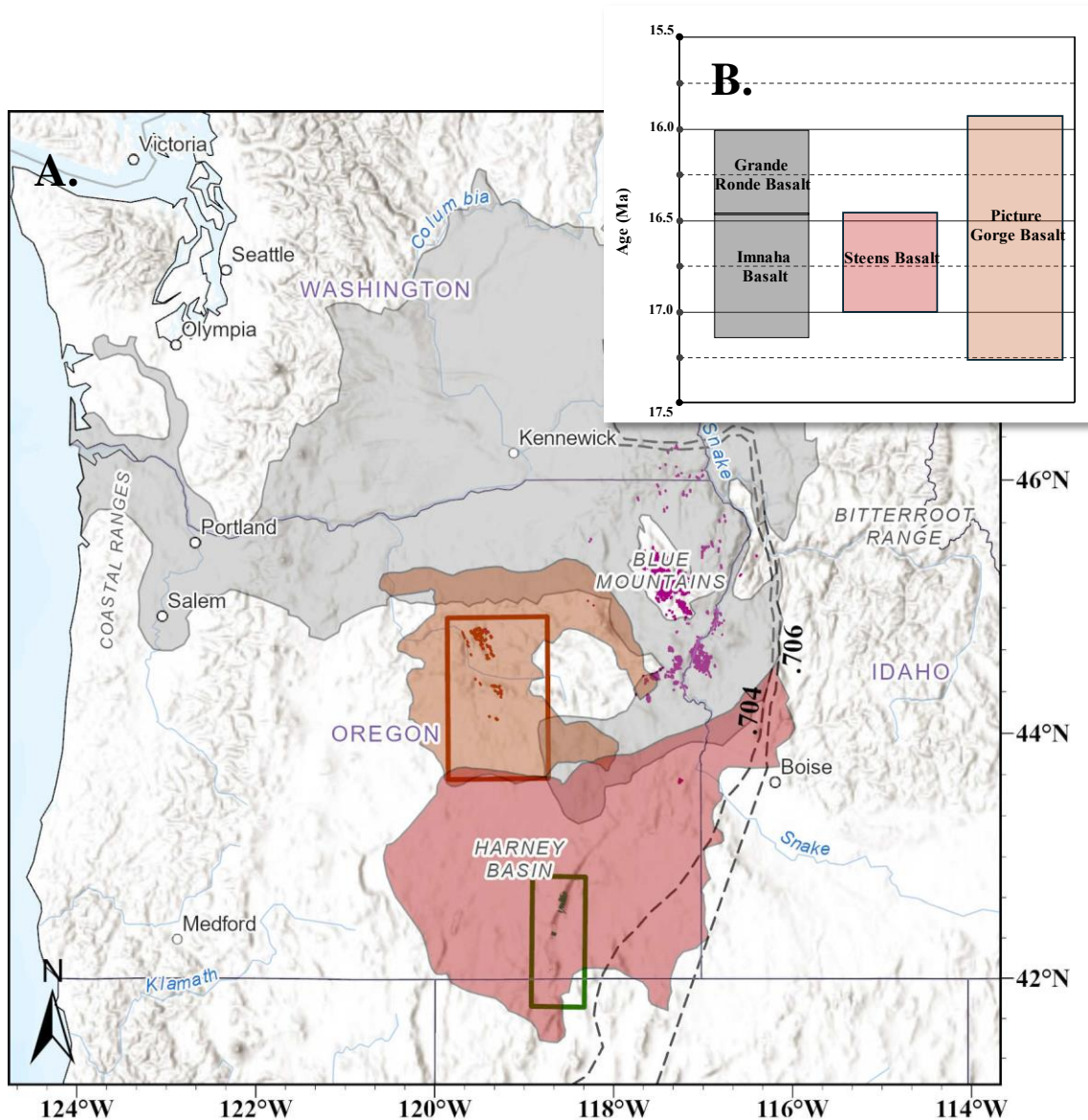


Figure 1: Map and Stratigraphy of Columbia River Basalt Group Deposits:

A. Map of the extent of main phase Columbia River Basalt Group deposits. Grey polygon: Innaha and Grande Ronde extents (modified from Camp et al., 2017); Tan polygon: Picture Gorge Basalt extent (modified from Cahoon et al., 2023); Red polygon: Steens basalt extent. Pink dots indicate dikes of the Chief Joseph Dike Swarm (CJDS)(Morriss et al., 2020); Red lines: Monument dike swarm (MDS) (Cahoon, personal communication); Green dots indicate dikes of the Steens dike swarm (SDS), mapped through orthoimagery; Gray dashed line : .704 (westernmost) and .706 (easternmost)  $^{87}\text{Sr}/^{89}\text{Sr}$  isopleths (modified from Camp et al., 2017); Orange rectangle: MDS field area; Green rectangle: SDS field area. B. Stratigraphy of the main phase Columbia River Basalt Group (modified from Cahoon et al. 2020)

## **GEOLOGIC CONTEXT OF THE CRBG**

The bedrock geology of eastern Oregon and adjacent areas to the north and south consists of a number of tectonic elements, namely accreted terranes, volcanic, and sedimentary deposits. Paleozoic and Mesozoic accreted terranes and stitching plutons of the Blue Mountains form the basement west of the .706 line (Figure 2) (Brooks, 1994; Dorsey and LaMaskin, 2008; Jones-Crafford, 2008; Colby et al. 2018). Paleozoic and Proterozoic terranes, composed of metasedimentary and volcanic facies, form the basement east of the .706 line. This will be referred to as cratonic margin hereafter (Brooks, 1994; Dorsey and LaMaskin, 2008; Jones-Crafford, 2008; Camp et al., 2013; Colby et al., 2018). The Eocene-Oligocene volcanic and volcanoclastic deposits of the Clarno and John Day formations of central and eastern Oregon and scattered Oligocene volcanics of southeastern Oregon and northern Nevada (Figure 3) are nonconformably deposited on Mesozoic accreted terranes (Figure 2) (McCloughrey et al., 2009; Isom and Streck, 2017; Cruz and Streck, 2017). These volcanics are primarily related to the mid-Tertiary ignimbrite flare-up and the rollback and foundering of the Farallon plate (McCloughrey et al., 2009; Best et al., 2016). Co-eval and slightly predating the CRBG are numerous rhyolitic centers throughout the study area (Streck et al. 2023). The region is structurally dominated by north-northeast Basin and Range extension, as well as west-northwest trending extension related to the rotation of the PNW around a pole located in northeast Oregon (Wells and McCaffrey 2013), suture zones between terranes (Dorsey and LaMaskin 2008), and shear zones between terranes (Jones-Crafford, 2008; Colby et al., 2018).

## ***PALEOZOIC AND MESOZOIC TERRANES:***

### ***Wallowa Terrane***

The Wallowa Terrane is composed of a thick sequence of Permian to early Jurassic volcanic, carbonate, and sedimentary rocks that record the evolution of an intra-oceanic island arc system (Brooks, 1994; Dorsey and LaMaskin, 2008). This terrane has been correlated with the Wrangellia Terrane, which contains exposures on Vancouver Island, Queen Charlotte Islands and the Wrangell Mtns. of Alaska (Brooks, 1994).

### ***Baker Terrane***

The Baker Terrane is a wide belt of sheared Permian to Early Jurassic argillite and chert, Devonian to Triassic limestone, serpentized forearc and oceanic crustal fragments and locally developed blueschist facies rocks of a long-lived subduction zone complex (Dorsey and LaMaskin, 2008).

### ***Izee Terrane***

The Izee Terrane is composed of a thick succession of Triassic and Jurassic sedimentary rocks that lie in depositional contact on older rocks of the Baker, Wallowa and Olds Ferry Terranes (Dorsey and LaMaskin 2008). This terrane represents the remnants of a doubly vergent accretionary wedge between subduction occurring between the Wallowa and Olds Ferry volcanic arcs, similar to the modern-day Moluccan thrust belt (Dorsey and LaMaskin, 2008)

### ***Olds Ferry Terrane***

The Olds Ferry Terrane is composed of Middle to Late Triassic volcanic and volcanoclastic rocks, and is correlated with the Quesnel terrane in British Columbia and the Cordilleran fringing-arc system in Nevada and California, namely the Black Rock-Jackson Terrane (Dorsey and LaMaskin, 2008)

### ***Black Rock-Jackson Terrane***

The Black Rock-Jackson Terrane is composed of volcanic arc, carbonate, and sedimentary sequences (Jones-Crafford 2008; Colby et al., 2018). This terrane has been correlated with the Olds Ferry Terrane, and likely represents a fragment of the original Mesozoic fringing arc (Jones-Crafford2008; Colby et al., 2018). According to Colby et al., 2018, the Olds Ferry Terrane likely represents the southern portion of the original Mesozoic arc and has been translated ~400km along a Cretaceous age dextral strike slip zone, of which the Mojave-Snow Lake Fault and Western Nevada Shear Zone are likely remnant strands of this Cretaceous strike slip zone.

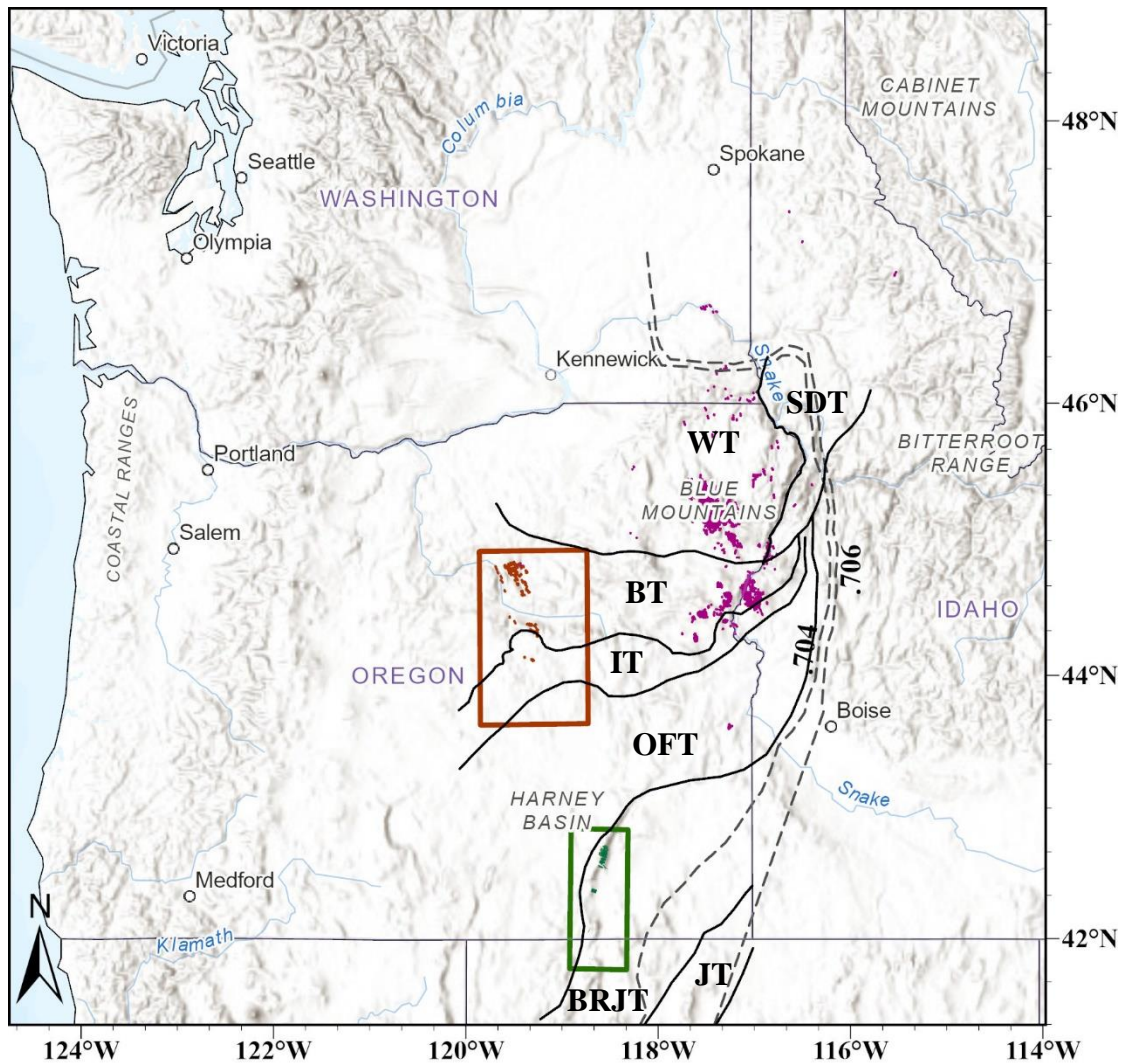


Figure 2: Terrane boundaries of eastern Oregon, northern Nevada, and western Idaho. Boundaries (solid black lines) are approximated from Dorsey and La Maskin, 2008, as well as Horton 2017. SDT: Seven Devils Terrane; WT: Wallowa Terrane; BT: Baker Terrane; IT: Izee Terrane; OFT: Olds Ferry Terrane; BRJT: Black Rock-Jackson Terrane; JT: Jungo Terrane; Black dashed line: .704 (westernmost) and .706 (easternmost) <sup>87</sup>Sr isopleths; Pink points: Chief Joseph Dike Swarm (Morriss et al., 2020); Orange points: Monument dike swarm (Cahoon, personal communication); Green points: Steens dikes (orthoimagery); Orange rectangle indicates MDS field area; Green rectangle indicates SDS field area.

### ***JOHN DAY-CLARNO ERUPTIONS***

The John Day and Clarno formations of central eastern Oregon (Figure 3) are an assemblage of ash-flow and airfall tuffs, lavas, and other volcanic deposits that are Eocene (Clarno volcanics) to Oligocene (John Day volcanics) age (McClaughrey et al., 2009). These deposits were formed from lavas and ejecta erupted from at least 3 calderas along a northeast trending axis, namely, the Wildcat, Crooked River, and Tower Mountain calderas, with two possible unnamed calderas near the Western Cascades (McClaughrey et al., 2009). These calderas make up the northern edge of a broad sweep of ignimbrite volcanism, the Mid-Tertiary ignimbrite flare up, that originates in Absaroka, Wyoming, and time-progressively sweeps through much of the American West (McClaughrey et al., 2009; Best et al., 2016). Recent mapping of the northeastern section of the Harney Basin and Strawberry Volcanics (Isom and Streck, 2017; Cruz and Streck, 2018), as well as exposures of calc-alkaline, I type rhyolites at the base of Steens Mtn and McDermitt Caldera (Henry et al., 2017) indicate that this late Oligocene to early Miocene volcanism was widespread throughout southeastern Oregon. Camp and Wells (2021) states that the John Day volcanics and widespread late Oligocene-early Miocene volcanics are related to the interaction between the YH plume tail and the thermomechanical erosion of the Farallon plate during delamination and rollback of the Farallon plate. Late Oligocene and early Miocene rhyolite and basaltic eruptions of the John Day formation and other southeastern Oregon volcanics likely represent the initiation of the influence of the YH upon eastern Oregon volcanism (Camp and Wells, 2021).

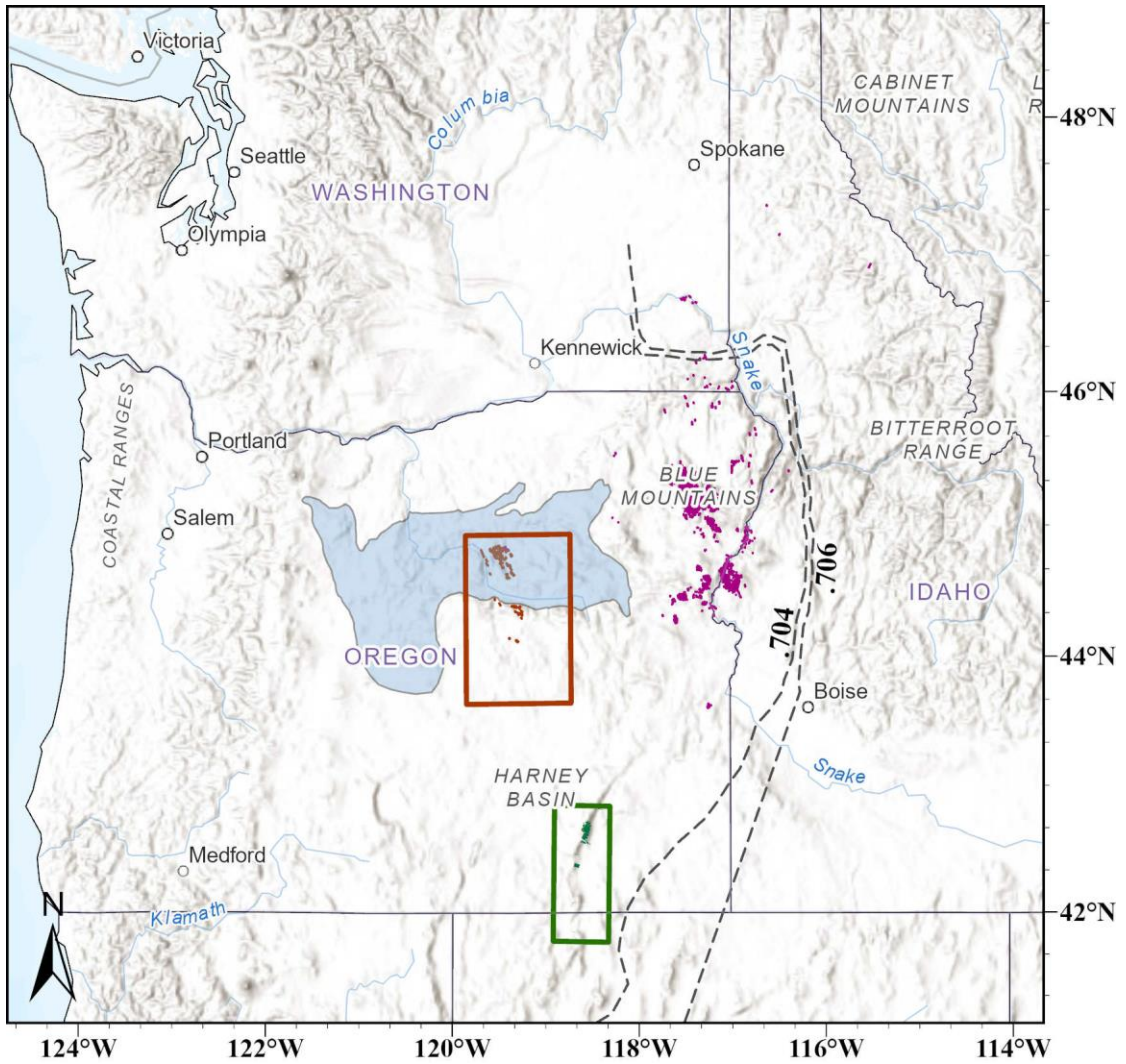


Figure 3: Map of John Day and Clarno volcanic deposits: Blue polygon: volcanic deposits (McClaughrey et al., 2009); Black dashed line indicates .704 (westernmost) and .706 (easternmost)  $^{87}\text{Sr}/^{89}\text{Sr}$  isopleths; Pink shapes: Chief Joseph Dike Swarm (Morriss et al., 2020); Orange shapes: Monument dike swarm (Cahoon, personal communication); Green shapes: Steens dikes (orthoimagery); Tan rectangle indicates MDS field area; Red rectangle indicates SDS field area. Not pictured are exposures of late Eocene-Oligocene volcanism in southeast Oregon, as they are not visible at the map scale.

### ***COLUMBIA RIVER RHYOLITES***

Largely co-eval with effusive basaltic eruptions of the CRBG were widespread rhyolitic eruptions from volcanic centers on the Oregon-Nevada border, closely paralleling the SDS and the cratonic boundary, representing the first rhyolitic eruptions along the Snake River Plain-Yellowstone Hotspot (SRP-Y) track (Camp et al., 2013) (Figure 4). Recent research (Streck et al. 2023) has shown, however, that this rhyolitic footprint is much bigger than earlier estimates, and encompasses a broad area 300-400 km in diameter, centered on the Oregon-Idaho Graben, Snake River Plain, and linear aeromagnetic anomalies (Zoback et al., 1994; Glen and Ponce, 2002; Wolff et al. 2008; Streck et al., 2023). Rhyolitic activity occurred 17.5-14.5 Ma, slightly pre and postdating the main phase of the CRBG eruptions (Streck et al., 2023). These rhyolites range from Fe-rich, A type rhyolites to calc-alkaline rhyolites (Streck et al., 2023), of which the former are primarily associated with intraplate volcanism and rifting (Eby, 1992). The overall footprint of these co-eval rhyolite fields is thought to be indicative of the broad area of basalt intrusions and crustal storage of CRBG magmas (Streck et al., 2023).

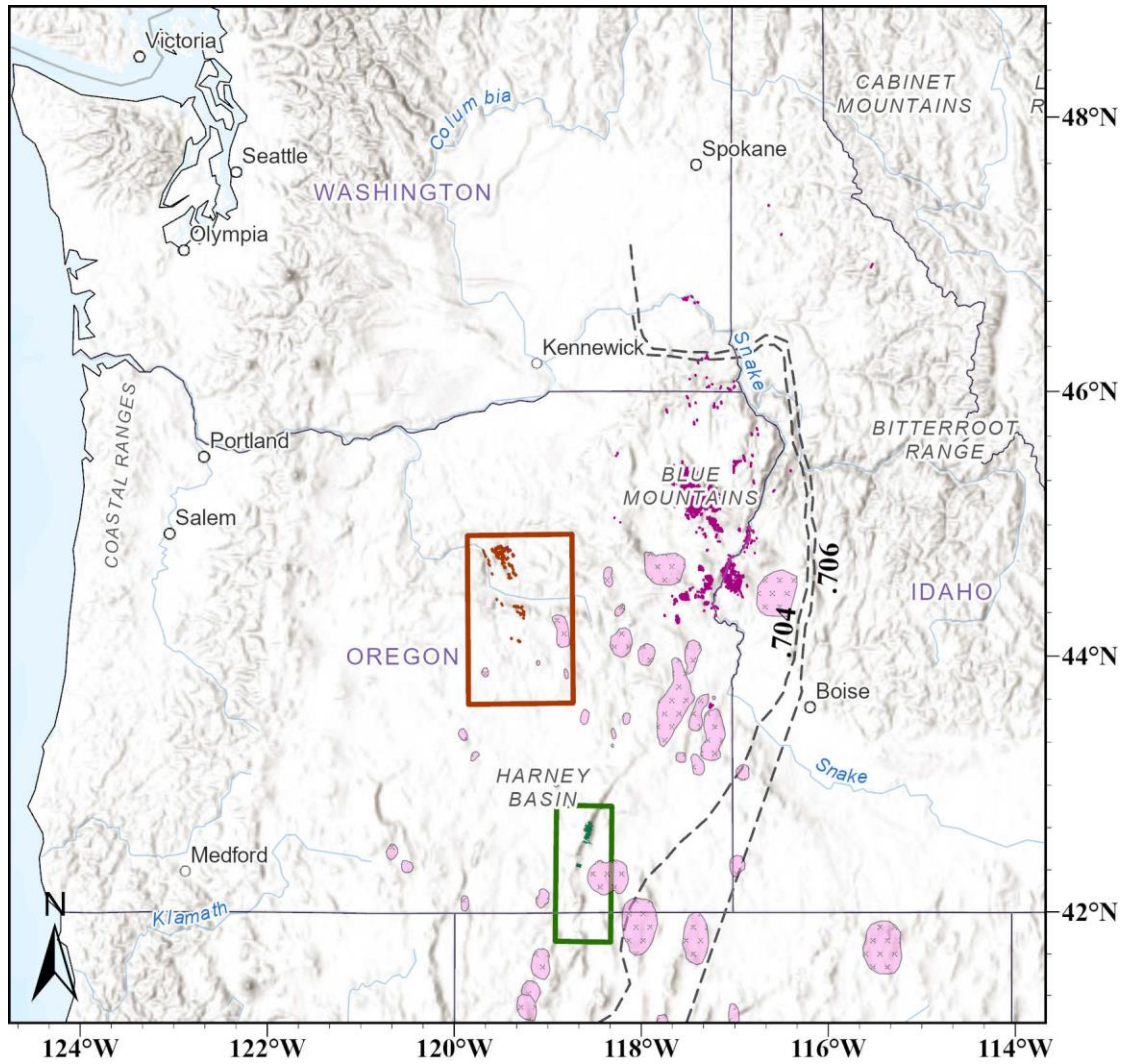


Figure 4: Map of co-eval mid-Miocene felsic volcanic deposits of Streck et al., (2023). Pink polygons: mid-Miocene felsic volcanics (Streck et al., 2023); Purple points: Chief Joseph Dike Swarm (Morriss et al., 2020); Orange points: Monument dike swarm (Cahoon, personal communication); Green points: Steens dikes (orthoimagery); Tan rectangle indicates MDS field area; Green rectangle indicates SDS field area. ); Black dashed line indicates .704 (westernmost) and .706 (easternmost)  $^{87/89}\text{Sr}$  isopleths

## ***REGIONAL TECTONICS***

The tectonics of eastern Oregon and the adjacent areas to the north, east, and south are complex. In the Mesozoic, the Blue Mountains Province (consisting of the Wallowa, Seven Devils, Baker, Izee, and Olds Ferry Terranes) was a site of protracted arc-arc and terrane-continent collision (Dorsey and LaMaskin, 2008). This resulted in crustal thickening throughout the province, as well as a doubly vergent thrust fault belt within the facing accretionary wedges (resulting in the Izee Terrane) (Dorsey and LaMaskin, 2008). In the later Mesozoic, low angle (“flat slab”) subduction of the Farallon slab resulted in translation of the Blue Mountains Province (BMP) ~400 km along a north-northeast dextral shear zone, of which the Mojave-Snow Lake Fault and Western Nevada Shear Zone are likely remnant strands (Colby et al., 2018), placing the BMP in its current position. Accretion of these allochthonous terranes and the development of the Cordilleran orogenic belt resulted in significant crustal shortening along north-northeast trending thrust faults in the southern portion of the study region through the Cretaceous (Humphreys 2006). This is due to flat slab subduction of the Farallon plate (Humphreys 2006; Best et al., 2016). This period of thickening ended in the Eocene, with the accretion of the Siletzia LIP. This caused a break in the Farallon plate, and a migration of the subduction zone to its current position (Humphreys 2006; Best et al., 2016). Foundering and rollback of the Farallon plate, and subsequent migration of subduction zone and angle lead to a reorientation of the stress regime, initiating gravitational collapse and extension along northwest trending normal faults in the Oligocene and early Miocene (Figure 5) (Humphreys et al., 2006). In the mid-Miocene, two major tectonic processes occurred: the increasing influence of the YH on the North American plate (Zoback et al.,

1994; Ponce and Glen 2001; Ponce and Glen 2002; Thomas and Sears 2007; Camp and Wells 2021) and the oblique subduction of the Pacific Plate (Dickinson 2006) as well as the continuing effects of slab rollback (Wells and McCaffrey 2013). YH impingement resulted in a radial trend of normal faulting (of which the Snake River Plain and Oregon-Idaho Graben are prominent examples), aeromagnetic anomalies interpreted to be mid-crustal keel dikes, and rapid Basin and Range extension centered near the Oregon-Idaho Graben (Figures 5,6) (Zoback et al., 1994; Ponce and Glen 2001; Ponce and Glen 2002; Thomas and Sears 2007; Camp and Wells 2021). Oblique subduction of the Pacific Plate and Farallon rollback resulted in the initiation clockwise rotation of western Oregon, expressed in the study area as west-northwest trending dip-slip faults related to the Brothers and Eugene-Denio Fault Zone (BFZ and EDFZ respectively) (Figures 5,6) (Dickinson 2006; Wells and McCaffrey 2013).

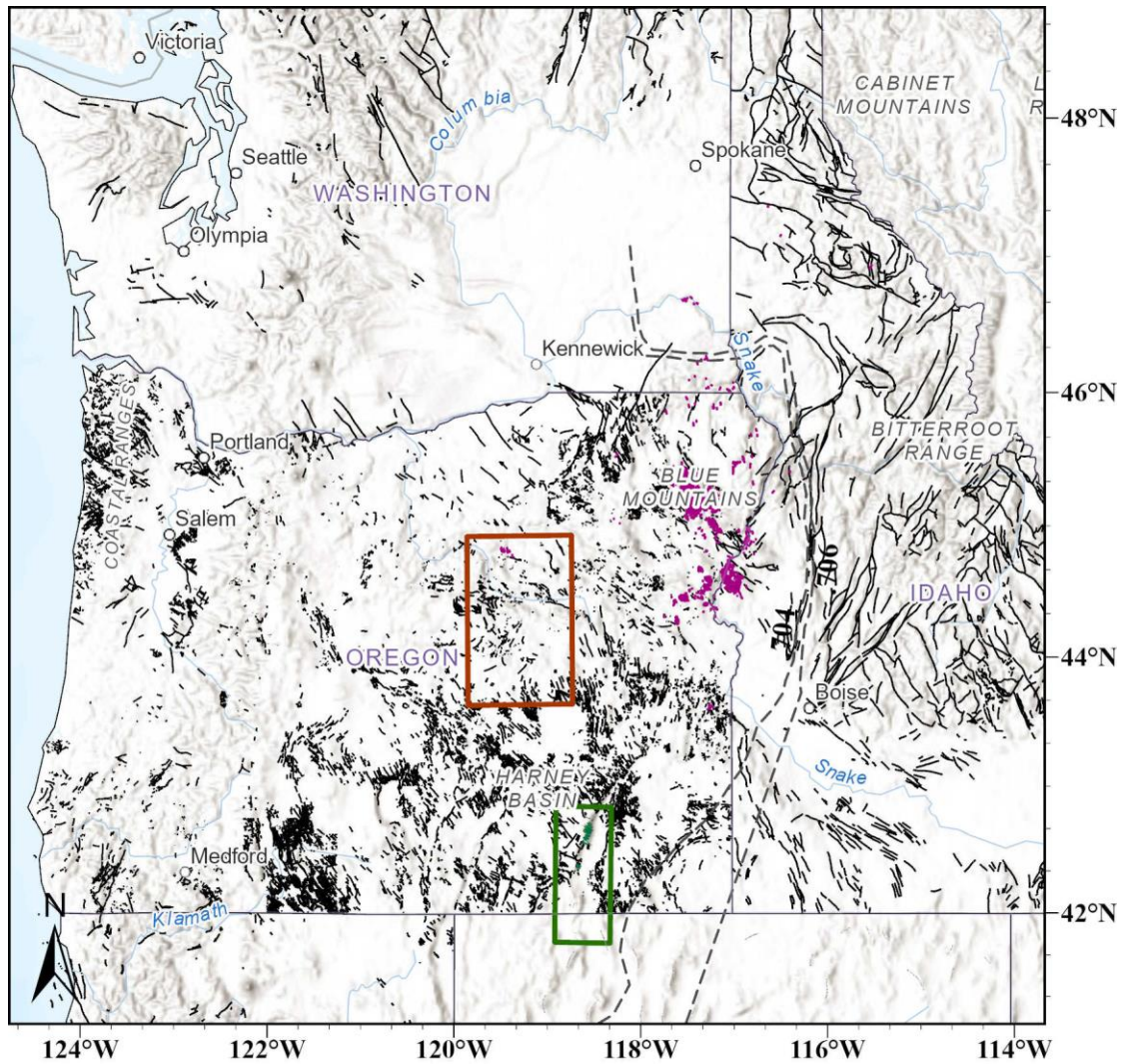


Figure 5: Map of normal and oblique faults in the Pacific Northwest. Solid gray lines indicate mapped faults of unknown age (Horton 2017); Solid red lines indicate Quaternary active faults (Machette et al., 2003). Black dashed line indicates .704 (westernmost) and .706 (easternmost) <sup>87/89</sup>Sr isopleths; Pink shapes: Chief Joseph Dike Swarm (Morriss et al., 2020); Orange shapes: Monument dike swarm (Cahoon, personal communication); Green shapes: Steens dikes (orthoimagery); Red rectangle indicates MDS field area; Green rectangle indicates SDS field area.

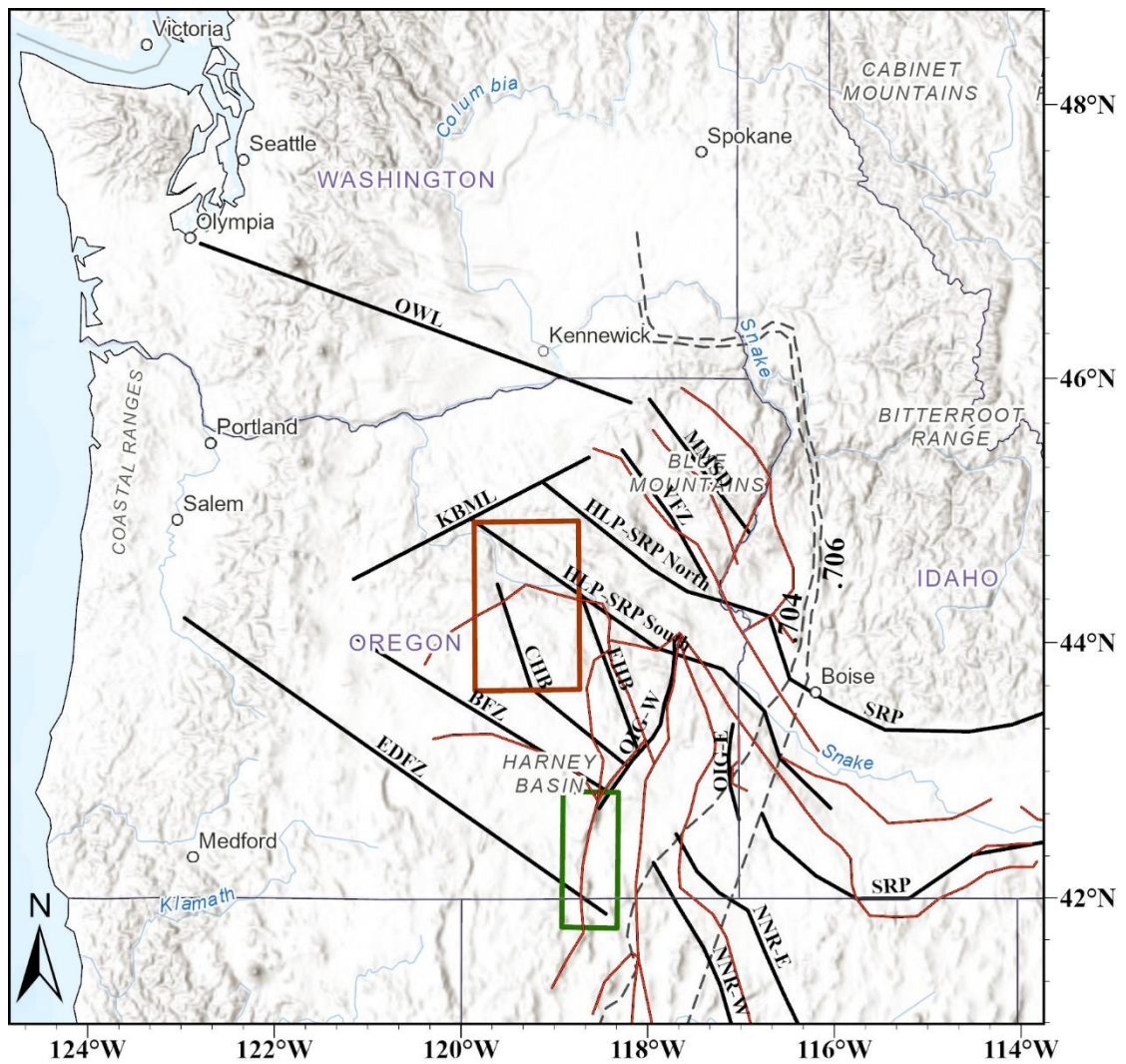


Figure 6: Map of major linear aeromagnetic, fault, and gravity lineaments.

Linear aeromagnetic: red lines; Fault and gravity lineaments (heavy black lines); EDFZ: Eugene-Denio Fault Zone; BFZ: Brothers Fault Zone; OIG: Oregon-Idaho Graben; OWL: Olympic-Wallowa Lineament; SRP: Snake River Plain; NNR: northern Nevada rift; KBML: Klamath-Blue Mountains Lineament (gravity); HLP-SRP: High Lava Plains-Snake River Plain; CHB & EHB: Central and eastern Harney Basin normal fault lineaments; MMSD: Fault lineament paralleling VFZ and other mid-Miocene stress direction normal fault lineaments; Black dashed line indicates  $.704$  (westernmost) and  $.706$  (easternmost)  $^{87}\text{Sr}/^{89}\text{Sr}$  isopleths; Pink shapes: Chief Joseph Dike Swarm (Morriss et al., 2020); Orange shapes: Monument dike swarm (Cahoon, personal communication); Green shapes: Steens dikes (orthoimagery); Tan rectangle indicates MDS field area; Red rectangle indicates SDS field area. Fault lineaments adapted from Horton et al., 2017, aeromagnetic lineaments adapted from Bankey et al., 2002 and Glen and Ponce 2002, and gravity lineaments from Schweitzer et al., 2020.

### ***MONUMENT DIKE SWARM/PICTURE GORGE BASALT***

Lavas that formed the Picture Gorge Basalt are the earliest and longest erupting of the main phase CRBG eruptions, from 17.2-16.0 Ma, and are largely contemporaneous with lavas of the Steens and Imnaha Basalt (Figure 1-B) (Cahoon et al., 2020). The Picture Gorge Basalt (PGB) lavas were sourced from the Monument Dike Swarm (Figures 1,7) in eastern Oregon, west of the town of John Day and north of the town of Burns in the Aldrich Mountains and John Day Basin, and represent ~1.1 (original) to 3.5% (revised, Cahoon et al. 2023) of the total eruptive volume of the CRBG (Fruchter and Baldwin 1976; Brandon et al., 1993; Cahoon et al., 2020, 2023), with recent revised estimates of eruptive volume ranging between 3500 and 8000 km<sup>3</sup> (Cahoon et al., 2023). The dikes of the MDS trend generally NW to NNW, and crosscut the Baker and Izee accreted terranes (Fruchter and Baldwin, 1976; Bailey, 1989; Brandon et al., 1993; Dorsey and La Maskin 2008), as well as volcanic deposits of the Clarno and John Day formations (Fruchter and Baldwin, 1975; Bailey 1989; McClaughrey et al., 2009), within a zone of back arc extension (Brandon, 1993; Cahoon et al., 2020). The majority of exposures of the MDS forms a narrow belt ~30 km wide by ~ 100 km long, trending NNW-SSE from ~44°N to ~45°N and 119°W-119.5°W. The dikes crosscut accreted the Izee and Baker Terranes south of US-26 and north of the town of Silvies, Olds Ferry Terrane south of the town of Silvies, and intrude into Baker Terrane and the Clarno and John Day volcanic deposits north of US 26.

Geochemically, the PGB are most similar to the Lower B Steens subunit of the Steens Basalts and the earliest Imnaha flows, as represented by the basal flows of the American Bar subgroup (Cahoon et al., 2020). Picture Gorge Basalt lavas are geochemically characterized by gently sloping to near flat REE profiles and are enriched in large ion lithophile elements (LILE's) compared to REE (Cahoon 2020). These lavas are the most MORB-like main phase unit (Cahoon, 2020), with some influence of subduction modified mantle, as evidenced by the enrichment of LILEs. Recent studies by Cahoon et al., (2023), however, show that the extent of PGB/MDS chemistry dikes may have a much wider footprint than previously realized, with lava flows found at Hart Mountain and several dikes within the Lake Owyhee Volcanic Field that share characteristic PGB/MDS geochemical parameters. The dikes from the Lake Owyhee Volcanic Field, while not shown directly in Figure 7, are part of the geochemical dataset that is used in this study.

The PGB is further subdivided into the geochemical and petrographic subunits, distinguished by plagioclase phenocryst size, modal mineral abundance, major element concentrations of  $\text{TiO}_2$  and  $\text{MgO}$ , and magnetic polarity. These are Twickenham, Monument Mtn., and Dayville subunits. These are then further split into 17 flow members (Bailey 1989), with the addition of a high  $\text{MgO}$  flow member believed to be parental magmas (Cahoon, 2020), for a total of 18 flow members. The Twickenham unit is largely characterized by being plagioclase phyric (Bailey, 1989; Cahoon, 2020), normally magnetized (Bailey, 1989), and contain  $>1.5$  and  $>6$  weight percent  $\text{TiO}_2$  and  $\text{MgO}$ , respectively (Bailey, 1989; Cahoon, 2020). This unit is the oldest, and contains the

Donnelly Basin, Bologna Creek, and Muleshoe Creek flow members (Bailey 1989). Following Twickenham is the Monument Mountain unit. This unit is characterized by aphyric to very sparsely phyric (<1% phenocrysts), fine grained basalt (Cahoon et al., 2023), normally magnetized (Bailey,1989; Cahoon 2020), and exhibits 1.4-1.7 and 5.0-8.0 weight percent TiO<sub>2</sub> and MgO respectively. The Monument Mtn subunit is further divided into four flow members: Stony Creek, Camas creek, Holmes Creek and Franklin Mtn (Bailey, 1989). The youngest unit, Dayville, is characterized by being variably plagioclase phyric with fine groundmass (Bailey, 1989), and includes the most evolved lavas (<6.0% MgO) and, compared to the other subunits, contains the most varied compositions overall (Cahoon,2020). This unit is normally magnetized through the first four flow members, transitional in one flow member (Branson Creek), and then reverse polarized through the remaining flow members of this subunit (Cahoon 2020). This unit is divided into 10 flow members, based on geochemical signatures. They are: Alder Mtn, Windy Canyon, Horse Canyon, Dale, Branson Creek, Johnny Cake, Little Tamarack, Tamarack Mtn., Hamilton, and the Monument Lookout members (Bailey, 1989). The Dayville subunit contains the greatest geochemical variability of all PGB subunits and encompasses nearly the whole compositional range of PGB lavas (Cahoon, 2020).

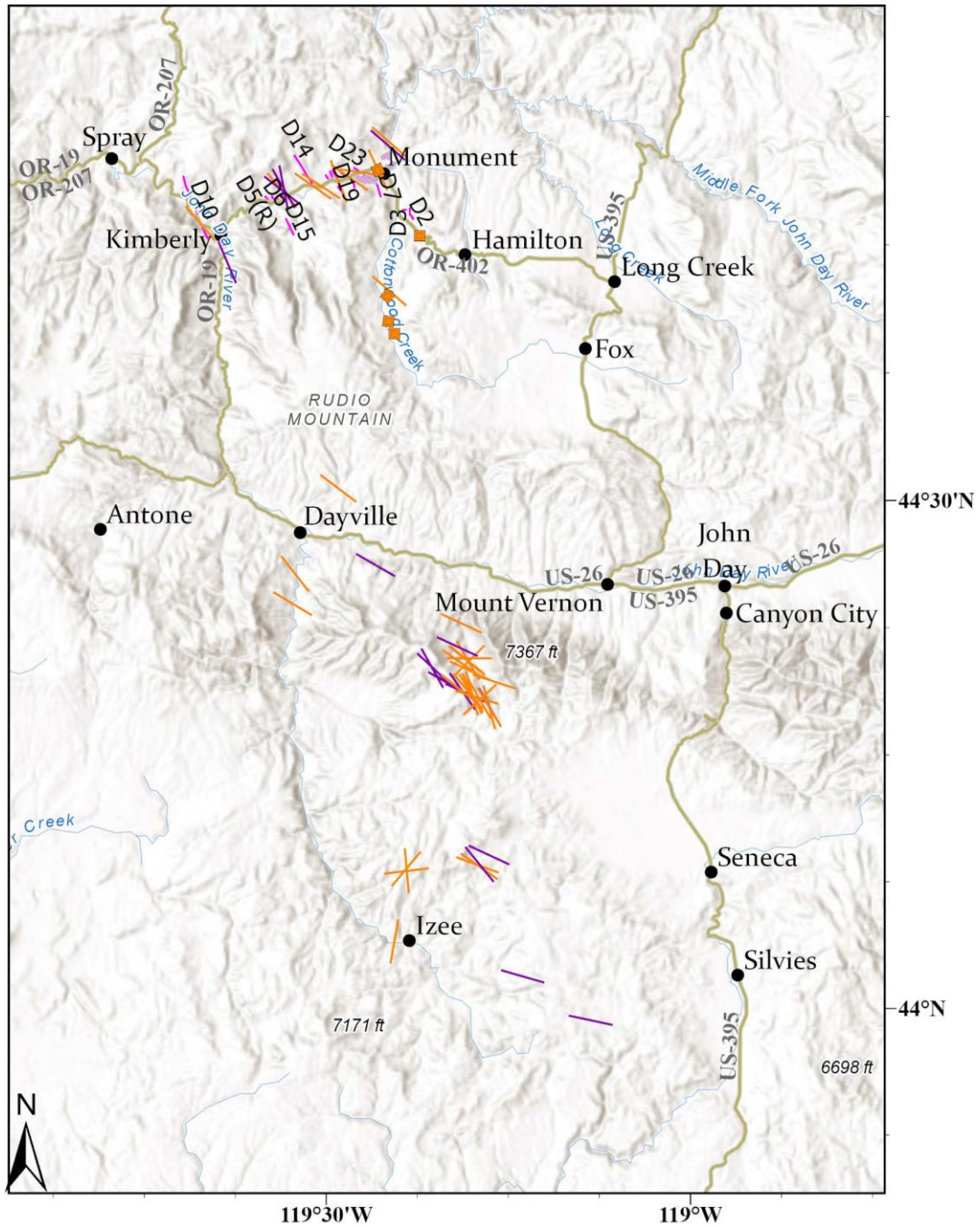


Figure 7: Map of sampled Monument Dike Swarm dikes. Brown lines: historical MDS dikes transcribed (Cahoon 2020) from topographic maps (Wallace and Calkins 1956) (Brown and Thayer, 1966)(Greene et al., 1972). Pink lines: Dikes mapped by Fruchter and Baldwin, 1973. Pink shapes: intrusive bodies mapped by Fruchter and Baldwin, 1973. Purple lines: dikes mapped by Cahoon, 2020, oriented along strike. Orange lines: dikes discovered in this study, oriented along strike.

### ***STEENS DIKE SWARM/STEENS BASALT***

Lava flows of the Steens Basalt were sourced from the Steens dike swarm (Figure 8) from 16.9-16.4 Ma, with the majority of emplacement occurring through 16.8-16.4 Ma (Moore et al., 2020) with an eruptive volume of 31,800km<sup>3</sup>, representing ~15% of the total eruptive volume of the CRBG (Moore et al., 2020). Early eruptions were likely fissure eruptions along a NNE trend starting to the south and west of the Pueblo Mountains, and is represented by feeder dikes, spatter ramparts and spatter cones, with later eruptions centralizing on the shield volcano at Steens Mountain (Camp et al., 2013), with near continuous eruptive activity from onset to cessation (Moore et al., 2020). The Steens Basalt and related intrusives are highly dissected from Basin and Range extension, with up to 2 km of exposure at the Steens escarpment (Moore et al., 2020; Camp et al., 2013). The type section for the Steens Basalt is Steens Mountain, a ~1 km thick stack of compound lava flows cut by dikes. Steens Mountain is an apparent shield volcano where the Steens eruptions localized (Camp et al., 2013; Moore et al., 2020a). The type location is well documented and studied with regard to stratigraphy, geochronology, and paleomagnetism of the flows, as well as numerous studies about the source of Steens Basalts (and the wider CRBG as a whole) (e.g. Camp et al., 2003; Camp and Ross, 2004; Breuseke et al., 2007; Wolff et al., 2008; Camp et al., 2013; Benson and Mahood, 2017; Moore et al., 2018; Moore et al., 2020). Work done by Moore et al., 2018 and Moore et al., 2020, however, shows compelling evidence of a complex, multitiered storage system through Os isotope analysis and stratigraphic changes in geochemistry.

The lavas of the Steens Basalt are primarily tholeiitic basalts, typical of most continental flood basalts, with waning stages weakly to moderately alkalic (Camp et al., 2013; Moore et al., 2020a; Moore et al., 2020b). Work done on this main phase unit has traditionally classified the Steens Basalt into two subunits, the Lower and Upper Steens Basalt (Camp et al. 2013). However, recent work by Moore et al., (2018) has shown that this unit is more appropriately split into three subunits, a Lower A, Lower B, and Upper Steens Basalt (Moore et al., 2018) These subunits are distinguished based on interpretations by Moore et al., (2020b) as to whether magma recharge or crustal assimilation + fractional crystallization (AFC) were the dominant processes responsible for compositional variation. Lower A Steens is characterized by heterogeneous and differentiated magmas, likely due to cool country rock and establishment of crustal storage (Moore et al., 2020b), and shows a mix between the processes of magma recharge and assimilation and fractional crystallization. Lower B Steens basalt is typified by primarily primitive compositions (higher MgO, low SiO<sub>2</sub>, lowest incompatible trace element concentrations), indicating that magmatic recharge was the dominant process in this subunit. Few to no weathering horizons and paleosols occur between flows, indicating that eruptions were near continuous (Moore et al., 2020b). Many lower A and B lavas are very plagioclase phyric (Camp et al., 2013; Moore et al., 2020a; Moore et al., 2020b and others), with up to 5cm long phenocrysts of plagioclase feldspars (Camp et al., 2013). The size and abundance of these plagioclase phenocrysts result in some Lower A and Lower B flows to be classified as giant plagioclase basalts (Sheth et al., 2016). Plagioclase phenocrysts show Sr isotope equilibration with whole rock values, indicating that these are phenocrysts rather than xenocrystic components (Moore et al., 2020). In the Upper Steens

Basalt crustal assimilation and fractional crystallization (AFC) rather than magmatic recharge is the dominant process. The most evolved (up to basaltic andesite), and alkalic (hawaiite-mugearite) occur within the Upper Steens Basalt subunit. This is a strong indicator of crustal storage of magmas and/or possible migration of storage location, with assimilation of more evolved crustal melts of the Black Rock-Jackson/Old's Ferry Terrane becoming progressively more important for the Upper Steens flows (Moore et al., 2020).

Lead, Sr, and Nd isotopic indicators show from early flows range in value from those typical of depleted Pacific mid-ocean ridge basalt (MORB) to a more ocean island basalt (OIB) and crustal contamination dominated trend in later flows (Wolff et al., 2008; Moore et al., 2020). High Os concentrations in some lavas sampled by Moore et al., (2020) indicate sulfide enrichment and saturation. Moore et al., (2020b) concludes that this is indicative of passage through a complex, multitiered magma storage system of multiple layered mafic/ultramafic intrusions, sills, and dikes through the middle and upper crust (Moore et al., 2020b).

The SDS dikes trend NNE (Figure 8), following the geophysical structures related to the suture zone of accreted terranes to the west and cratonic crust to the east (represented by the  $^{87}\text{Sr}/^{89}\text{Sr} = 0.704$  and  $^{87}\text{Sr}/^{89}\text{Sr} = 0.706$  lines) and largely parallels the western arm of the Oregon-Idaho Graben (Camp et al. 2013; Moore et al., 2020). Mapped basaltic dikes with a similar geochemical signature to Steens Basalt in the Santa Rosa-Calico volcanic field (SRCVF), to the east of Steens Mountain, all fall along the easternmost large scale aeromagnetic anomalies first described by Glen and Ponce in 2002 that may extend as far

as southern Nevada (Zoback, et al., 1994; Glen and Ponce 2002; Breuseke et al., 2008; Camp et al., 2013). This anomaly itself coincides with the eastern graben of the northern Nevada rift system and Oregon Idaho Graben. All other Steens dikes and vents lie along the trend of the westernmost anomalies that represent deep seated intrusions, i.e., large keel dikes (Zoback et al., 1994; Glen and Ponce 2002; Camp and Ross, 2004; Camp et al., 2013; Ernst et al., 2019). These keel dikes likely supplied many of the dikes associated with Steens Basalt volcanism (Camp et al., 2013).

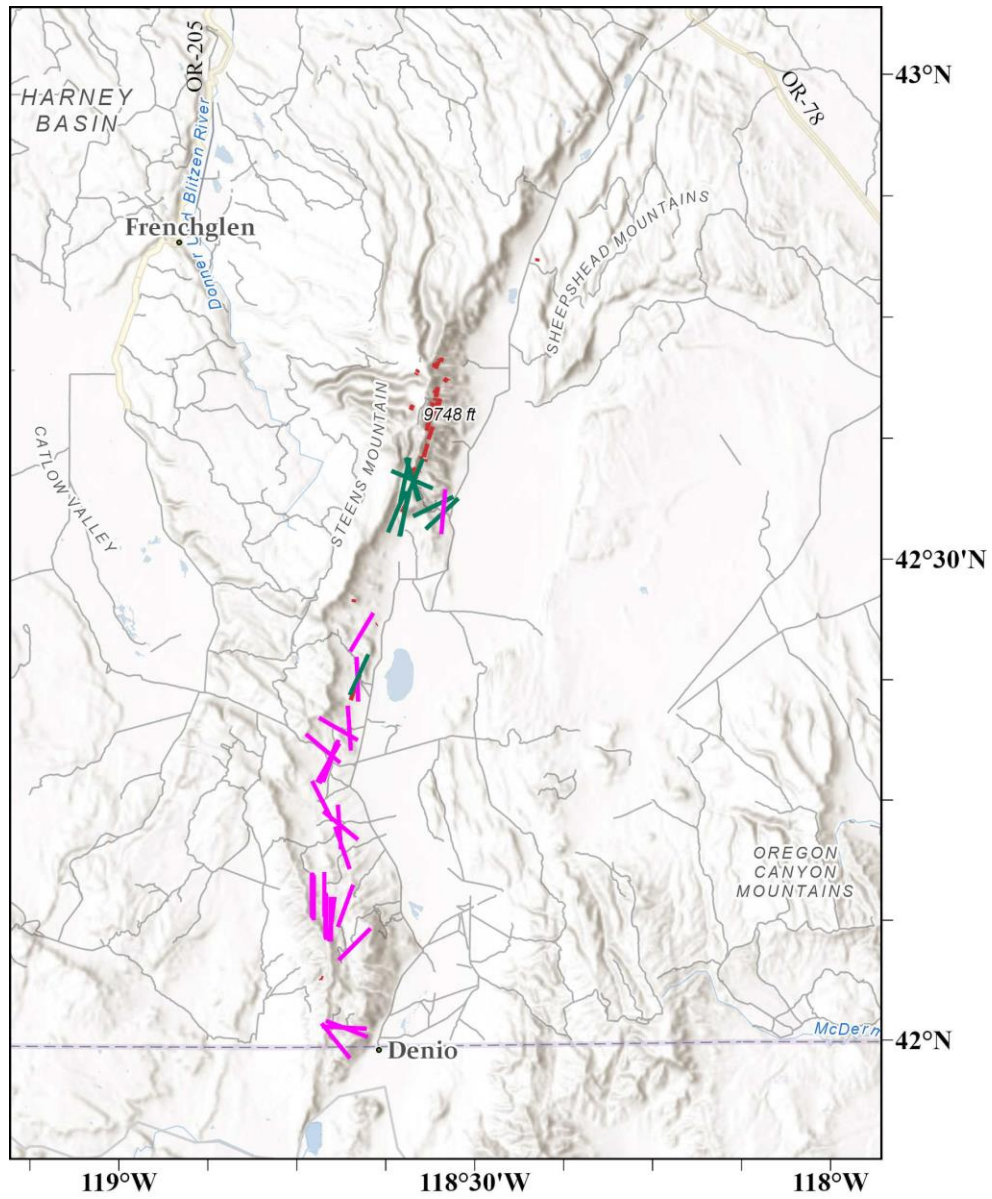


Figure 8: Dike map of historical and sampled dikes of this study of the Steens Dike Swarm (SDS). Red lines/shapes: dikes mapped through orthoimagery; Green lines: dikes sampled by Moore and Grunder 2020; Pink lines: dikes sampled and discovered in this study.

## METHODS

### FIELD WORK

Field work was conducted over the course of approximately 8 weeks, split between the 2021 and 2022 summer field seasons. Prior to fieldwork, an inventory of known dikes was established using previous research and ArcGIS files provided by Emily Cahoon (pers. comm., 2020), and Moore and Grunder (2020), and this included possible dikes as delineated in Google Earth orthoimagery. During the field season, some dikes were newly discovered and sampled. Dikes were accessed through a combination of hiking and driving on Jeep trails. One sampling of a dike consisted of collecting 2 to 4 approximately fist sized samples, with one sample used for billets, one for representative hand sample, and one for geochronology/geochemical sampling. Weathering surfaces on samples were removed while out in the field to streamline laboratory preparation. A total of 92 samples were collected across both dike swarms, consisting of: 5 country rock samples, 3 samples of co-eval mineralization of country rock, 4 hydrothermally altered dikes, 57 dikes, and 21 other intrusive bodies (sills and layered mafic-ultramafic intrusion). Field observations were made regarding country rock contacts and visible alteration or mineralization thereof where applicable. Width of dikes were measured using a pace method and converting to length, rounded to the nearest meter to account for foot length variation. Strike was measured on all dikes, utilizing the built in compass of the author's Samsung S20 Ultra 5g. Location, photographic, and field observations were recorded using Avenza Maps on the aforementioned Samsung device. At the conclusion of each field season, data was exported from Avenza Maps as a .csv file and imported into Microsoft Excel, where the data was organized and split into appropriate fields for

geochemical and geographic modelling. Data was then appended to the geochemical data supplied from the Peter K. Hooper Geoanalytical Laboratory, Washington State University-Pullman. Mapping of data for modelling was done through ArcGIS Pro.

### **PETROGRAPHY**

A total of 32 samples were cut into 3 x 2 x 1 cm billets and sent to Spectrum Petrographics in Vancouver, Washington. All samples were prepared as polished thin sections. Samples were embedded in a clear epoxy resin and ground to 30  $\mu\text{m}$  thickness. Spectrum Petrographics then performed full slide photography in both plane polarized and cross polarized light (PPL and XPL, respectively), with a 27 x 46 mm field of view. Samples were further analyzed using a Zeiss petrographic microscope.

### **GEOCHEMISTRY**

Samples were crushed to pebble size utilizing a Braun WD Chipmunk Crusher at Portland State University. The crushed samples were then taken to the Peter Hooper Geoanalytical Lab at Washington State University, Pullman (WSU) for further preparation for x-ray fluorescence (XRF) and inductively coupled plasma mass spectroscopy (ICP-MS) chemical analysis. At WSU, samples were pulverized into powders using a tungsten carbide swing mill, with the mill material low in Ta and Nb to avoid contamination of these elements. Four grams  $\pm$  0.002 g of the resulting powder was mixed with dilithium tetraborate ( $\text{Li}_2\text{B}_4\text{O}_7$ ) (LiTET) in a 2:1 ratio to the sample before fusing mixed samples into a glass bead. Samples were fused in graphite cups in an oven at a temperature of 1000 C. Glass beads were then re-ground into powder using the tungsten carbide swing mill after cooling. One half to one full gram of the powder is then

separated for ICPMS analysis. The remaining powder is then returned to the graphite cups for re-fusing. The resulting 2nd glass bead is then subjected to XRF analysis, using the Thermo-ARL Advant XP automated XRF machine. The other 0.5-1.0 g of powder was dissolved for ICPMS analysis, using an Agilent 7700 Inductively Coupled Mass Spectrometer (ICP-MS). Obtained chemical data was then appended to the master excel file and R database for use in geochemical and geographic modelling.

### **GEOCHRONOLOGY**

Ten dikes were selected from a southeast to northwest transect of the MDS, based on sample condition and differing MgO content. Samples were verified to contain no weathering surfaces, veins, or alteration products, and stored in plastic bags with unique sample numbers to prevent cross contamination.

Samples were prepared for Ar/Ar geochronology analysis primarily at the Oregon State University Argon Geochronology Laboratory (OSU AGL) and Portland State University Hard Rock Lab (PSU HRL). Samples were crushed using a Braun WD Chipmunk Crusher and a JC-300ST to obtain a grain size of <2 mm at the PSU HRL. The crushed material was washed with deionized water and an ultrasonic bath, and dried at 100°C. The cleaned and dried samples were then sieved to obtain a uniform size distribution of 100-300 µm at the PSU HRL. Samples were then transferred to the OSU AG and underwent magnetic separation using a Frantz Magnetic Barrier Laboratory Separator to remove Fe/Ti oxides and mafic minerals such as olivine, leaving only plagioclase groundmass separates (9 samples) and plagioclase phenocrysts (1 sample). Groundmass samples were then acid leached using five separate ultrasonic baths of different aqueous

solutions for approximately one hour. The solutions are as follows: 1M HCl, 6M HCl, 1M HNO<sub>3</sub>, 3M HNO<sub>3</sub>, and milli-Q water. The plagioclase phenocryst sample was acid leached using 2.5M HF and milli-Q water. Samples were then dried in an oven at 100°C for ~12 hrs. Approximately 22 mg of material were handpicked from each sample using binocular microscopes. Groundmass separates were picked preferentially choosing separates that had minimal mafic mineral intergrowth. Phenocryst separates were chosen based on lack of damage from acid leaching and visual purity (absence of mafic minerals).

Samples were then loaded into aluminum capsules for irradiation in the TRIGA CLICIT nuclear reactor at OSU, along with the Fish Canyon Tuff (FCT) sanidine ( $28.201 \pm 0.023$  Ma,  $1\sigma$ ) (Cahoon et al., 2015). The Ar/Ar analysis was performed using the ARGUS IV mass spectrometer at the Oregon State University Argon Geochronology Laboratory. The samples were loaded into Cu-planchettes in an ultra-high vacuum chamber and incrementally heated by a defocused 25 W CO<sub>2</sub> industrial engraving laser. After heating, gases were cleaned using a SAES-Zr-Al ST101 getter, operated at 400°C for 10 minutes, and two SAES Fe-V-Zr ST172 getters operated at 200°C and room temperature.

Age calculations were performed using the ArArCALC software (Koppers 2002) using the decay constants of Steiger and Jager (1977). The age spectrum for each sample was analyzed to determine the plateau age, which represents the time of last significant Ar loss from the sample.

## **GEOCHEMICAL MODELING**

Geochemical and location data of all intrusive samples of this study, as well as the intrusive and extrusive samples of: Fruchter and Baldwin (1979), Wolff and Ramos (2008), Cahoon (2020), and Moore and Grunder (2020a) were gathered into one dataset. Trace element and rare earth element (REE) diagrams were generated using Microsoft Excel, with trace element diagrams normalized to the primitive mantle (PM) values of Sun and McDonough (1989) and REE diagrams normalized to C1 chondrite values of Sun and McDonough (1989). Most binary plots and total alkali silica diagram were generated using the ggplot package in RStudio.

Geochemical correlations between intrusives samples of this study and the flows were done using Orange, a data mining and machine learning software. The only sample sets not included in this classification are the layered mafic intrusion samples, as these are crystal cumulates and as such, are not appropriate to classify into subunit/flow member. For PGB/MDS this is 3 subunits and 18 flow members, and for Steens/SDS this is a total of 4 subunits. A total of five separate datasets were created for this, as follows:

- One master PGB/MDS teaching dataset (n = 205) of all classified intrusive and flow samples of: Bailey (1989), Wolff et al., (2008), and Cahoon (2020)
- One master Steens/SDS teaching dataset (n = 91) of all classified intrusive and flow samples of Wolff et al., (2008) and Moore and Grunder (2020a)
- One subunit learner dataset of MDS (n = 39) samples of this study
- One subunit learner dataset of SDS (n = 17) samples of this study
- One flow member learner dataset of MDS (n = 39) samples of this study.

First, teaching datasets and subunit learner datasets were imported into Orange, and run through 3 machine learning models (tree, random forest and support vector machine learning), with the flow subunit as the target and all major element data, XRF trace elements (Ni, Cr, Sc, V, Cu, and Zn), and ICPMS data (La, Ce, Pr, Nd, Sm, Eu, Gd, Tb, Dy, Ho, Er, Tm, Yb, Lu, Ba, Th, Y, Hf, Ta, U, Pb, Cs, Sr, Sc, Zr, Rb, and Nb) used as classifying factors. The “Test and Score” option was used, and accuracy of the three models was determined using a random sampling of 100 train/test instances using 95% of the training data. The machine learning model with the highest calculated accuracy (CA) was used. The learner datasets were then appended with the flow subunit determined by the most accurate machine learning model. The PGB/MDS flow member dataset followed the same procedure as above, however, accuracy of the model was determined slightly differently. As several of the eighteen flow members had only a small number of samples (<5), accuracy was instead determined by testing the predictions against the test data, using cross fold stratification with 20 folds, with the machine learning model with the greatest CA selected.

## RESULTS

### CLASSIFICATION

#### *MONUMENT DIKE SWARM*

Calculated accuracy for subunit designation was determined by using a random sampling of 100 train/test instances utilizing 95% of the training data. The model with the greatest average calculated accuracy across the four subunits (Twickenham, Monument Mtn., Dayville, and the high MgO subunits), and was then applied to the learner dataset for use in flow member determination. The results for subunit distribution, with subunit calculated accuracy and machine learning model applied are in Table 1. Flow member calculated accuracy was determined using cross fold stratification, utilizing 20 folds. The machine learning model with the highest average calculated accuracy across all 18 flow members was chosen. Flow member distribution, flow member calculated accuracy, and learning model are reported in Table 2.

Subunit	Calculated Accuracy (CA)	n	Learning Model
Twickenham	0.88	17	Random Forest
Monument Mtn	0.865	6	Random Forest
Dayville	0.872	24	Random Forest

Table 1: Calculated accuracies and distribution of subunit classification using a random forest machine learning model.

Subunit	Member	Calculated Accuracy (CA)	n	Learning Model
Twickenham	Donnelly Basin	0.973	11	Tree
Twickenham	Bologna Creek	0.989	5	Tree
Monument Mtn.	Camas Creek	0.957	1	Tree
Monument Mtn.	Holmes Creek	0.952	4	Tree
Monument Mtn.	Franklin Mtn	0.962	1	Tree
Dayville	Horse Canyon	0.973	1	Tree
Dayville	Windy Canyon	0.968	3	Tree
Dayville	Alder	0.962	2	Tree
Dayville	Dale	0.968	1	Tree
Dayville	Branson Creek	0.984	4	Tree
Dayville	Johnny Cake Mtn.	0.984	2	Tree
Dayville	Tamarack Mtn.	0.935	2	Tree
Dayville	Hamilton	0.984	5	Tree
Dayville	Monument LO	0.973	4	Tree

Table 2: Calculated accuracies and distribution of flow member classification using the tree machine learning model.

### ***STEENS DIKE SWARM***

A total of 17 SDS dikes were introduced into the learner dataset and ran through 3 machine learning models, utilizing all major and trace element data. Calculated accuracy of the subunit designation was determined by using a random sampling of 100 train/test instances, utilizing 95% of the training data. The model with the greatest calculated accuracy across the two subunits (Lower and Upper Steens) was used. The results for subunit distribution, with subunit calculated accuracy and the machine learning model applied are reported in Table 3. The subunit was then appended to the flow member

learner dataset, with the average calculated accuracy determined by using as used in subunit accuracy. Flow member distribution, calculated accuracy, and learning model are reported in Table 4. Individual probability counts for all subunit and flow members of both dike swarms are included in the master dataset in Appendix A.

Subunit	Calculated Accuracy (CA)	n	Learning Model
Lower	0.820	13	Random Forest
Upper	0.822	4	Random Forest

Table 3: Calculated accuracies and subunit distribution of Steens samples using the random forest machine learning model.

Member	Calculated Accuracy (CA)	n	Learning Model
Lower A Steens	0.902	6	Random Forest
Lower B Steens	0.904	7	Random Forest
Upper Steens	0.989	4	Random Forest

Table 4: Calculated accuracies and flow member distribution of Steens samples using the random forest machine learning model.

## **GEOCHEMISTRY**

### ***MONUMENT DIKE SWARM***

Monument dikes are primarily basalt to basaltic andesite in the total alkali-silica diagram of Le Bas et al. (1986). Twickenham typically contains between 47.5-51 wt.% SiO<sub>2</sub>, with the bulk of samples falling between 2-4 wt.% total alkali content (Figure 9). Monument Mountain contains a more evolved composition with a range of ~49-52.5 wt.% SiO<sub>2</sub> and between 3-4% total alkali (Figure 9). Dayville compositions span the largest range of both SiO<sub>2</sub> and total alkali content, with ranges of 47.5-56 wt.% and ~2.5-5% respectively (Figure 9). Dikes classified as Twickenham typically contain between 6-8 wt. % MgO,

10-12 wt. % CaO, 10-12 wt. % FeO\*, 1.5-2 wt. % TiO<sub>2</sub>, and 0.3-0.7 wt. % K<sub>2</sub>O (Figures 11 and 12). Dikes classified as Monument Mountain contain between 5-7 wt. % MgO, 10-11 wt. % CaO, 10-12 wt. % FeO\*, 1.5-2 wt. % TiO<sub>2</sub>, and 0.5-1 wt. % K<sub>2</sub>O (Figures 11 and 12). Dikes classified as Dayville vary significantly more in compositional range, and contain 4-9 wt. % MgO, 6-13 wt. % CaO, 8-16 wt. % FeO\*, 1-2.5 wt. % TiO<sub>2</sub>, and 0.1-1 wt. % K<sub>2</sub>O (Figures 11 and 12). Subunits can be somewhat differentiated from one another in various trace element plots (Figures 13–15), with Twickenham generally being relatively more depleted in incompatible trace elements (i.e. Ba, Th, Zr, Y) and relatively more enriched in compatible ones (i.e. Cr, Ni) when compared to other subunits. Twickenham does, however, show an enrichment in Nb relative to SiO<sub>2</sub>, as well as a greater Zr/Y ratio relative to SiO<sub>2</sub> compared to the other two subunits. The Dayville subunit is the inverse of Twickenham, and is relatively enriched in incompatible trace elements, and more depleted in compatible ones, however some Dayville dikes, notably of the Horse, Dale, Alder, Windy and Branson Creek flow members strongly overlap Twickenham dikes in all binary plots. Monument Mountain often occupies the moderate values of both incompatible and compatible trace elements; however it can be distinguished by a relatively high Cr/Ni ratio, with a range of 3-4 (Figure 14).

All dikes show an “arc signature” on incompatible element diagrams when normalized by primitive mantle values of Sun and McDonough (1998), with enrichments relative to mid ocean ridge basalt (MORB) in Ba, K, Sr, and Pb (Figure 10). Rare earth element (REE) patterns are most consistent with E-type MORB concentrations levels (Sun and McDonough, 1989), with slight enrichment in light-REE (LREE) relative to heavy-REE

(HREE) (Figure 10). The Twickenham and Monument Mountain subunits show strong clustering in both the trace element and REE diagrams and also share a small, positive Eu anomaly (Figure 10). Dayville compositions are more variable, with enrichments between approximately 4 to 50 times that of the primitive mantle of Sun and McDonough (1989), and between 11-50 times that of the C1 chondrite of Sun and McDonough (1995) (Figure 10).

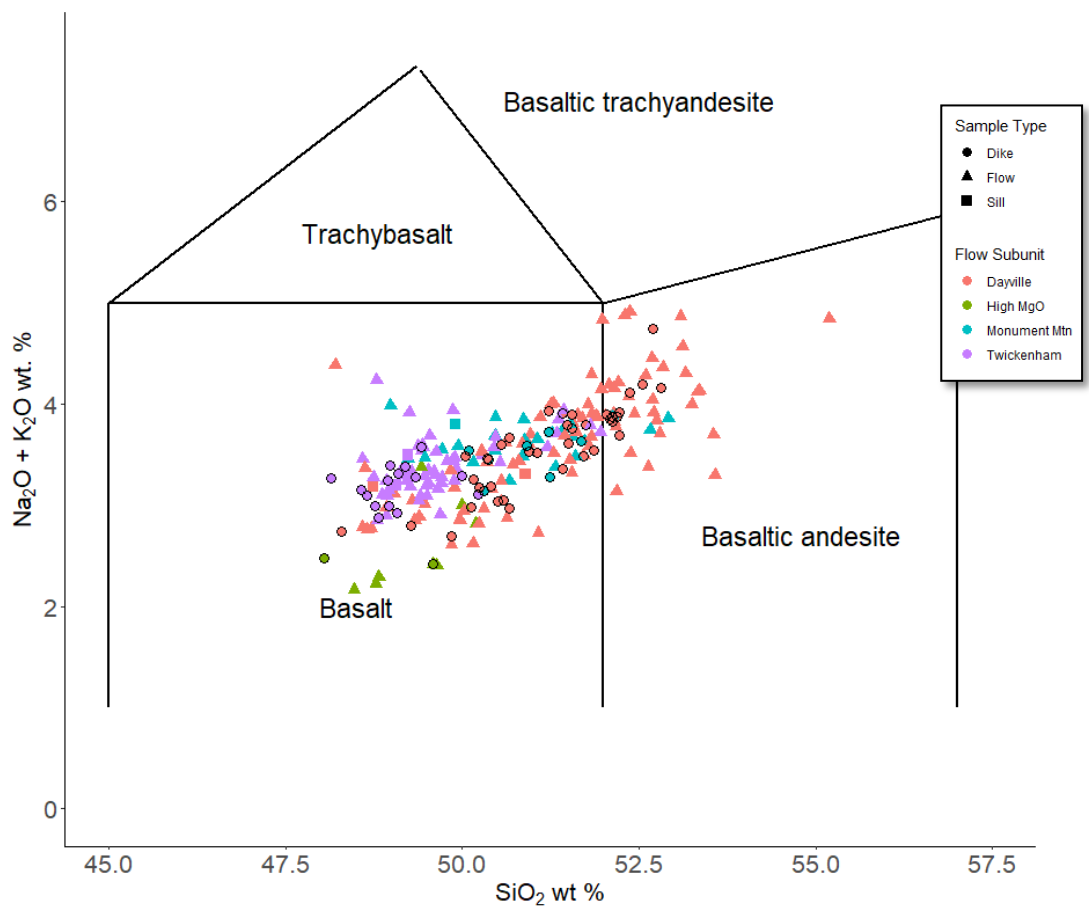


Figure 9: Part of the Total alkali-silica diagram (Le Bas et al., 1986).

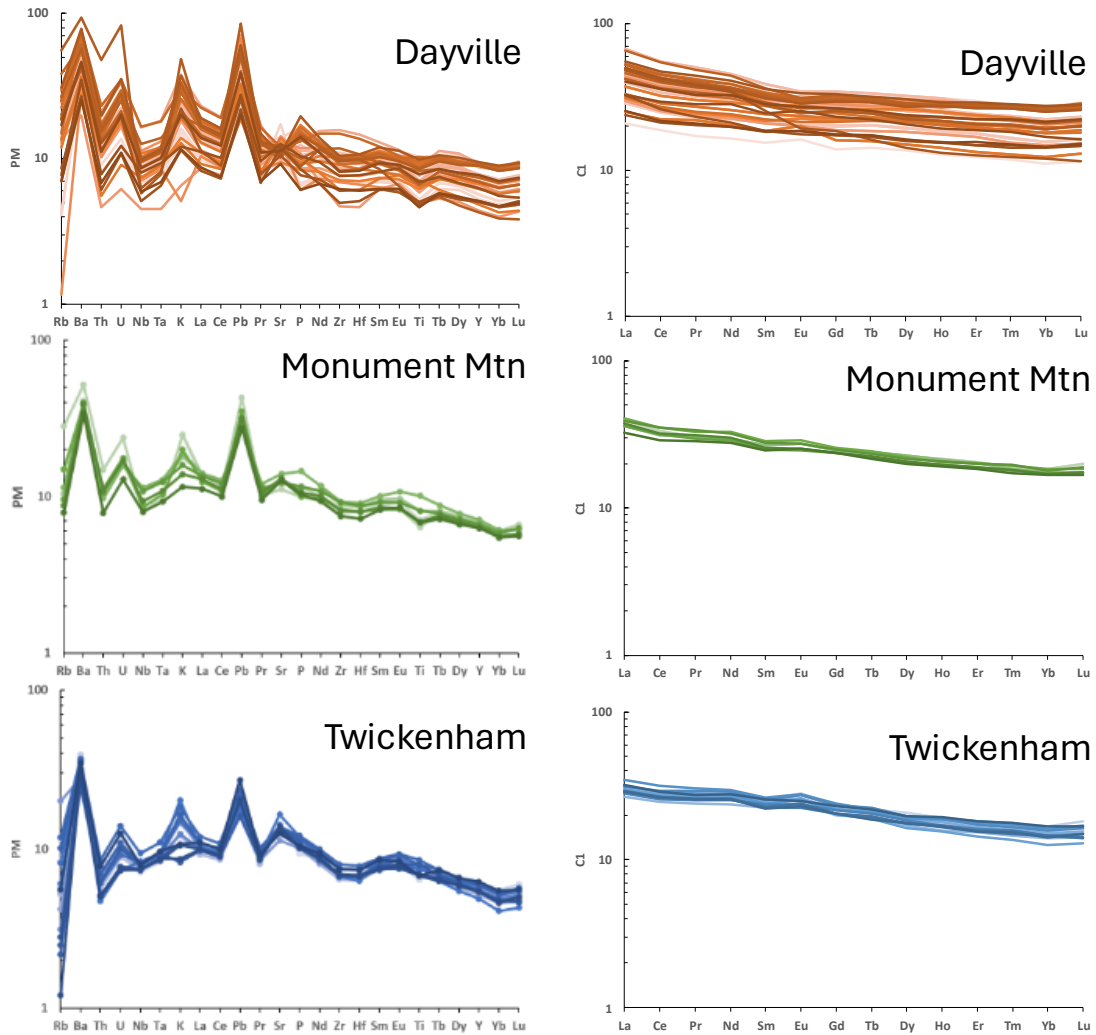


Figure 10: Incompatible element and REE diagrams of Monument Dikes.

Left hand column: incompatible element diagrams of Monument dikes, normalized to primitive mantle of Sun and McDonough (1989), by subunit. Right hand column: rare earth element diagrams of Monument dikes, normalized to C1 chondrite of McDonough and Sun (1995).

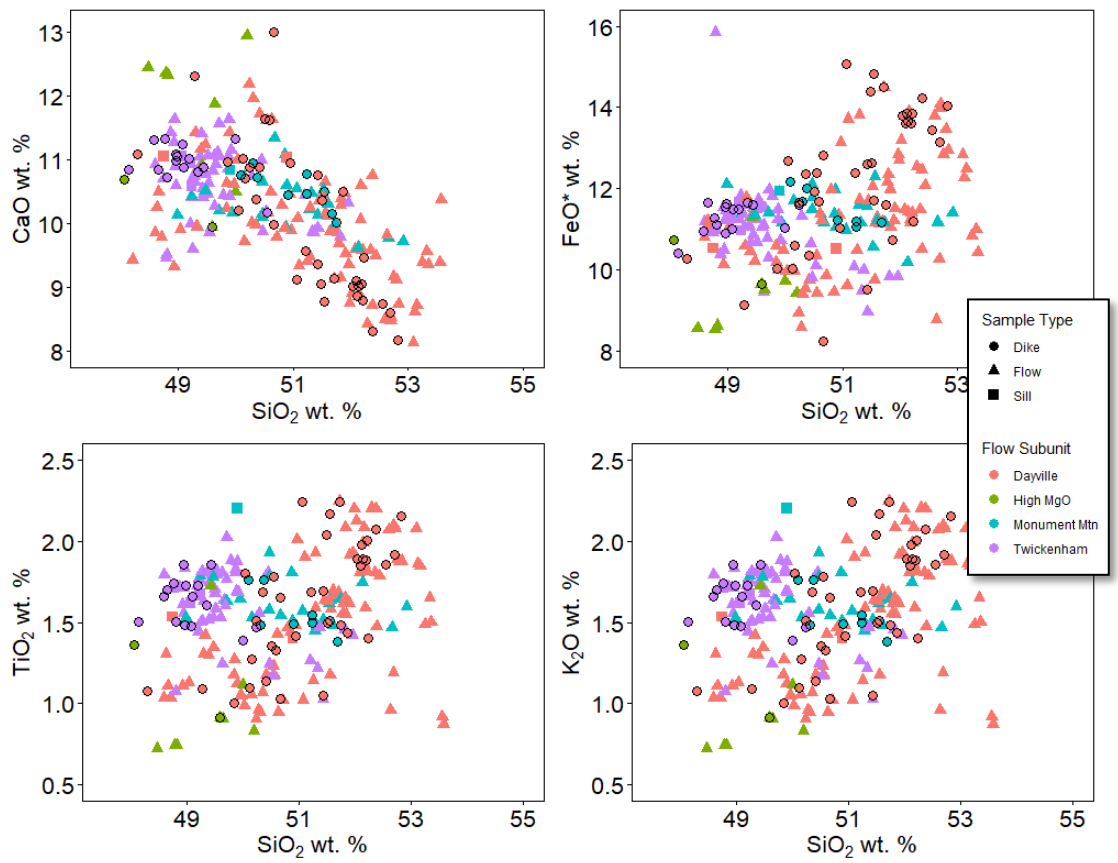


Figure 11: Plots of major element vs. SiO<sub>2</sub> wt. % of Picture Gorge Basalt and Monument dike samples.

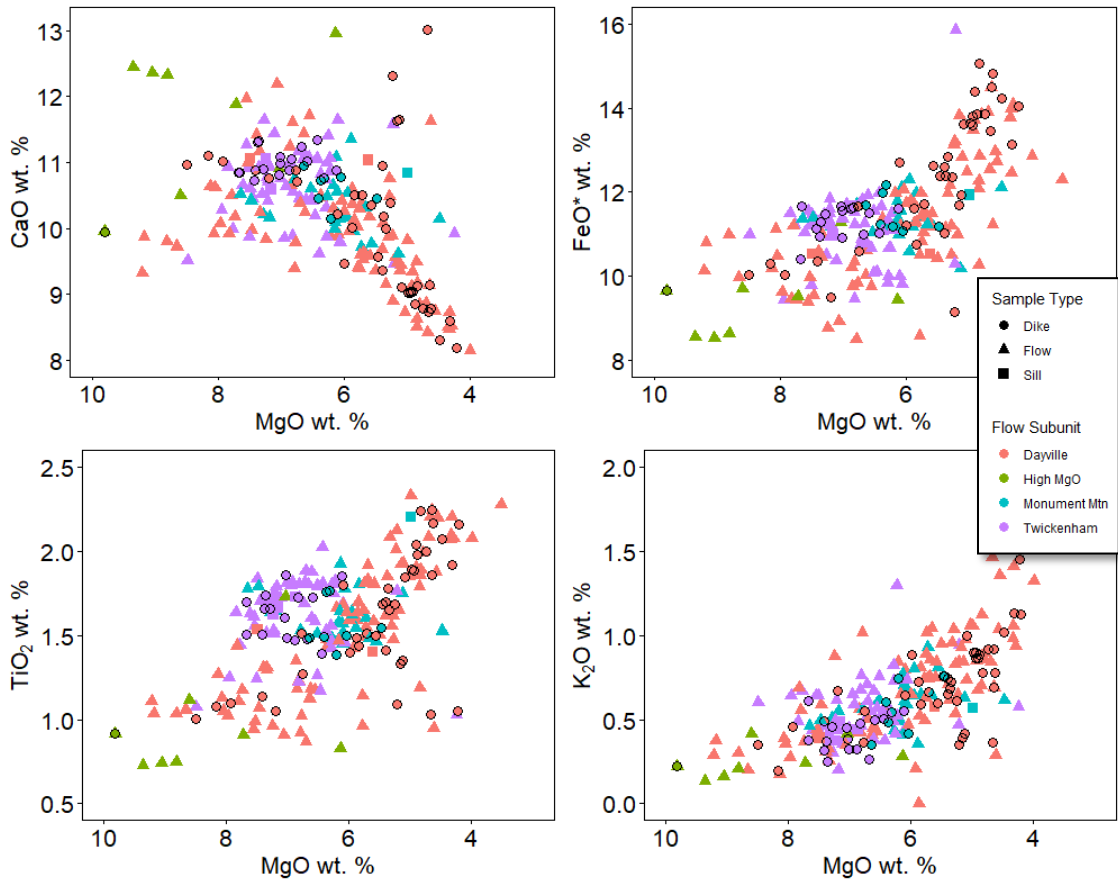


Figure 12: Plots of major element vs MgO wt. % of Picture Gorge Basalt and Monument dike samples.

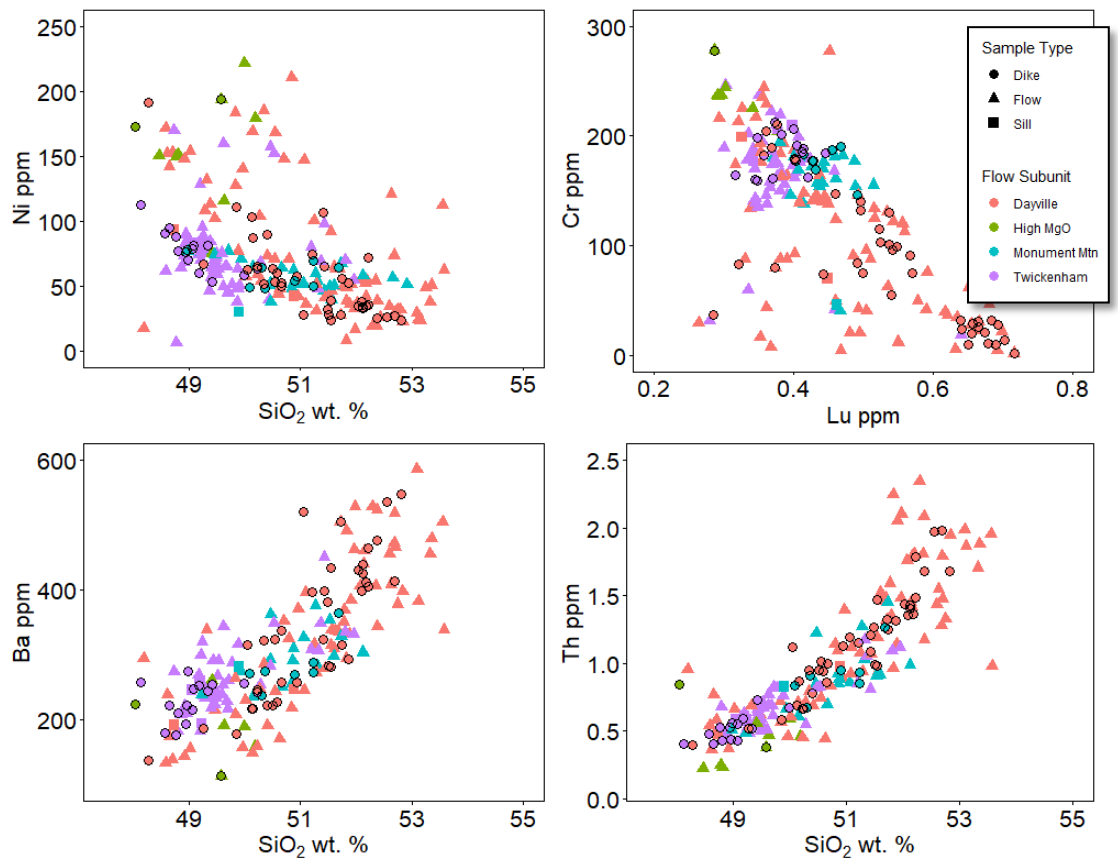


Figure 13: Plots of compatible and incompatible trace element vs. SiO<sub>2</sub> of Picture Gorge Basalt and Monument dike samples

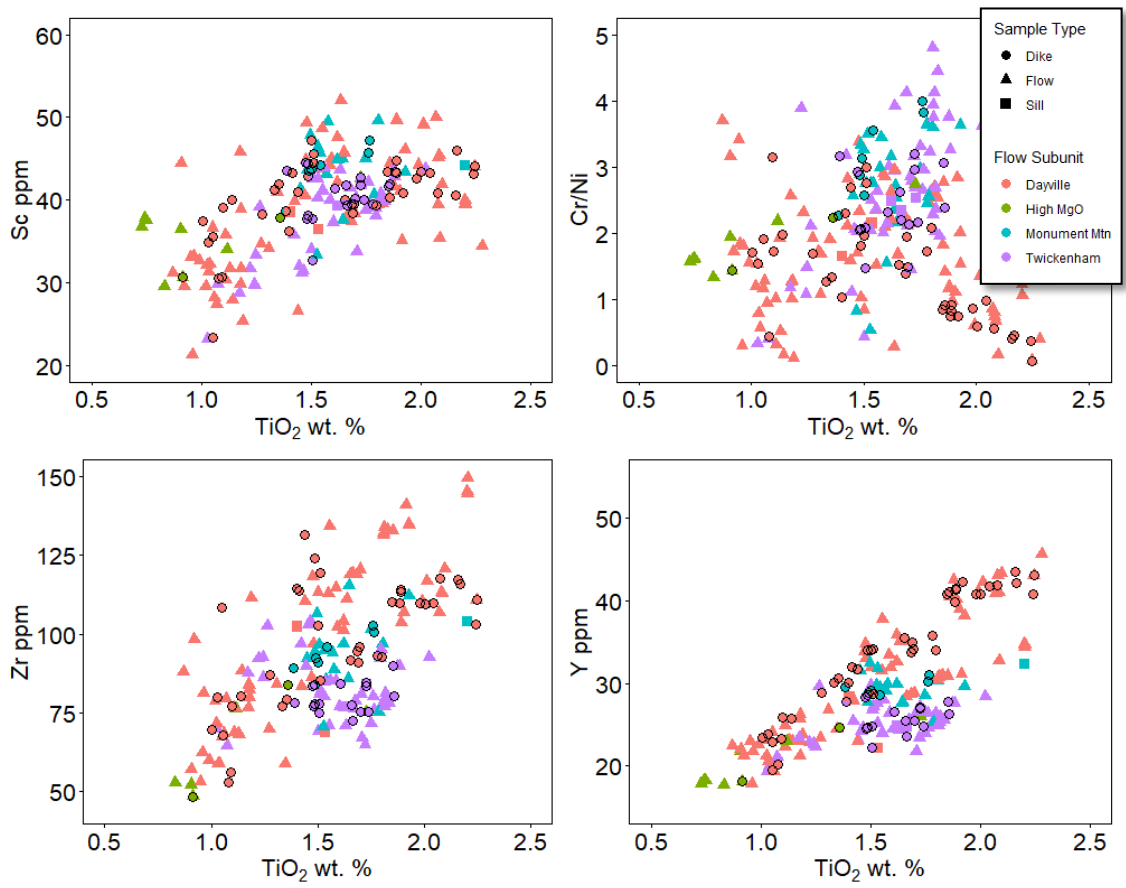


Figure 14: Plots of trace element vs.  $\text{TiO}_2$  of Picture Gorge Basalt and Monument dike samples

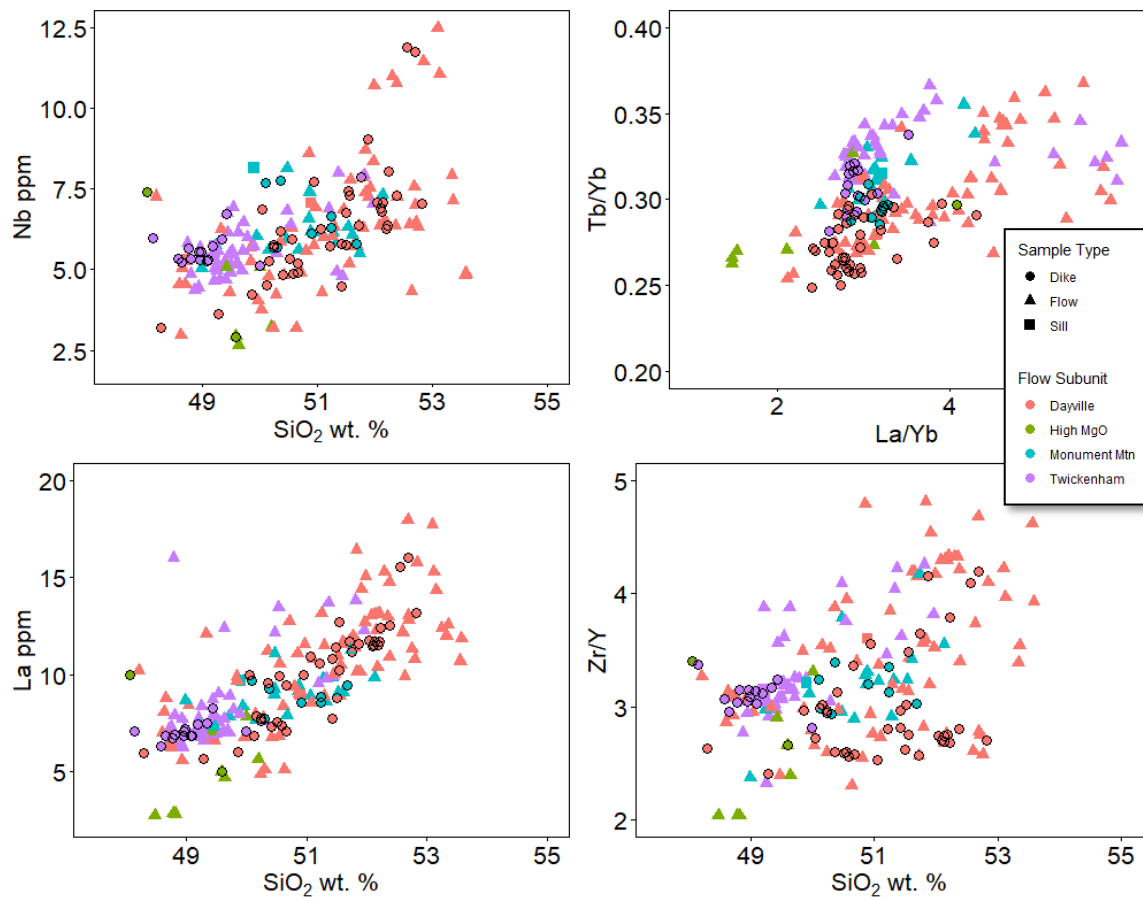


Figure 15: Plots of incompatible trace element vs SiO<sub>2</sub> of Picture Gorge Basalt and Monument dike samples

### ***STEENS DIKE SWARM***

Steens dikes range in composition from basalt, basaltic andesite, trachybasalt and basaltic trachy-andesite on a total alkali-silica (TAS) diagram (Le Bas et al., 1986) (Figure 16).

In addition, 15 samples along two transects of a newly discovered layered mafic-ultramafic intrusion (informally referred to as the Streck LMI) are included in the geochemical results. Samples of the Streck layered mafic intrusion (Streck LMI) range in composition from micro-basaltic and tephritic to trachy basalt and basaltic trachy-andesite. Steens dike samples are largely tholeiitic, with some Upper Steens and most Streck LMI samples being more alkalic, and are more accurately described as ankaramites, hawaiiites, and mugearites. This is defined by a  $\text{Na}_2\text{O}$  wt. % - 2.0 being greater than or equal to  $\text{K}_2\text{O}$  wt. % values (Le Bas et al. 1986). On major element vs  $\text{SiO}_2$  wt. % plots, samples of the Lower A and Lower B Steens contain between 5-11 wt. % MgO, 8-11 wt % CaO, between 9-13 wt. %  $\text{FeO}^*$ , 1.25-2.5 wt. %  $\text{TiO}_2$ , and generally less than 1.1 wt. %  $\text{K}_2\text{O}$  (Figures 18, 19). Upper Steens samples typically contains less than 6.5 wt. % MgO, less than 9 wt. % CaO, greater than 11.5 wt. %  $\text{FeO}^*$ , greater than 2.0 wt. %  $\text{TiO}_2$ , and greater than 1.0 wt. %  $\text{K}_2\text{O}$  (Figures 18,19). It should be noted that Lower A Steens dikes and flows fall on both the most primitive and evolved end of the compositional spectrum, and while the bulk of the samples fall within the Lower Steens spectrum, some Lower A Steens samples also fall within the more evolved end of the Upper Steens compositional spectrum. Streck LMI samples largely fall within the median to upper values, and largely overlap Upper Steens compositions, with the exception of the titanomagnetitic anorthosite layer (represented by sample RS22S28D) and the two micro-basaltic samples from the olivine melagabbro layer (represented by samples RS22S30B

and RS22S30C), which plot on the most primitive end of the Lower B Steens compositional spectrum. Lower Steens samples show a wide range of Ni and Cr content, containing between 50-300 and 100-800 ppm respectively. Upper Steens samples are typically more depleted in these elements, and in general contain less than 100 and 200 ppm Ni and Cr, respectively. This is reversed in incompatible trace elements vs SiO<sub>2</sub> plots, with Upper Steens generally occupying the more enriched space and Lower Steens occupying the more depleted space relative to SiO<sub>2</sub> (Figure 20, 21).

All dikes and intrusives show an “arc signature” when plotted on mantle-normalized incompatible element diagrams using values of Sun and McDonough (1998), with enrichments relative to mid ocean ridge basalt (MORB) in Ba, K, Sr, and Pb and depletions relative to MORB in Nb: Ta on a trace element diagram (Figure 17). Rare earth element (REE) patterns are in the range of ocean island basalt (OIB) values given by Sun and McDonough (1989), with significant enrichment in LREE relative to HREE (Figure 17).

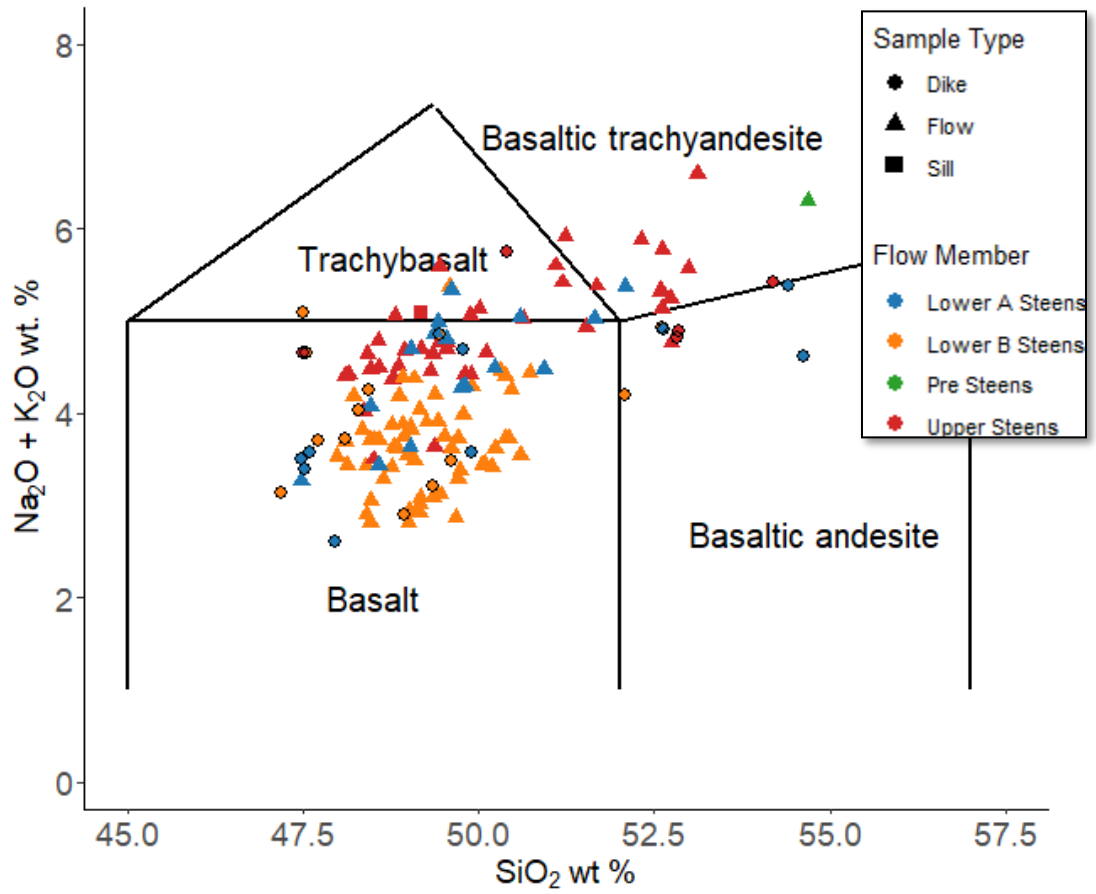


Figure 16: Part of the Total alkali-silica diagram (Le Bas et al., 1986).

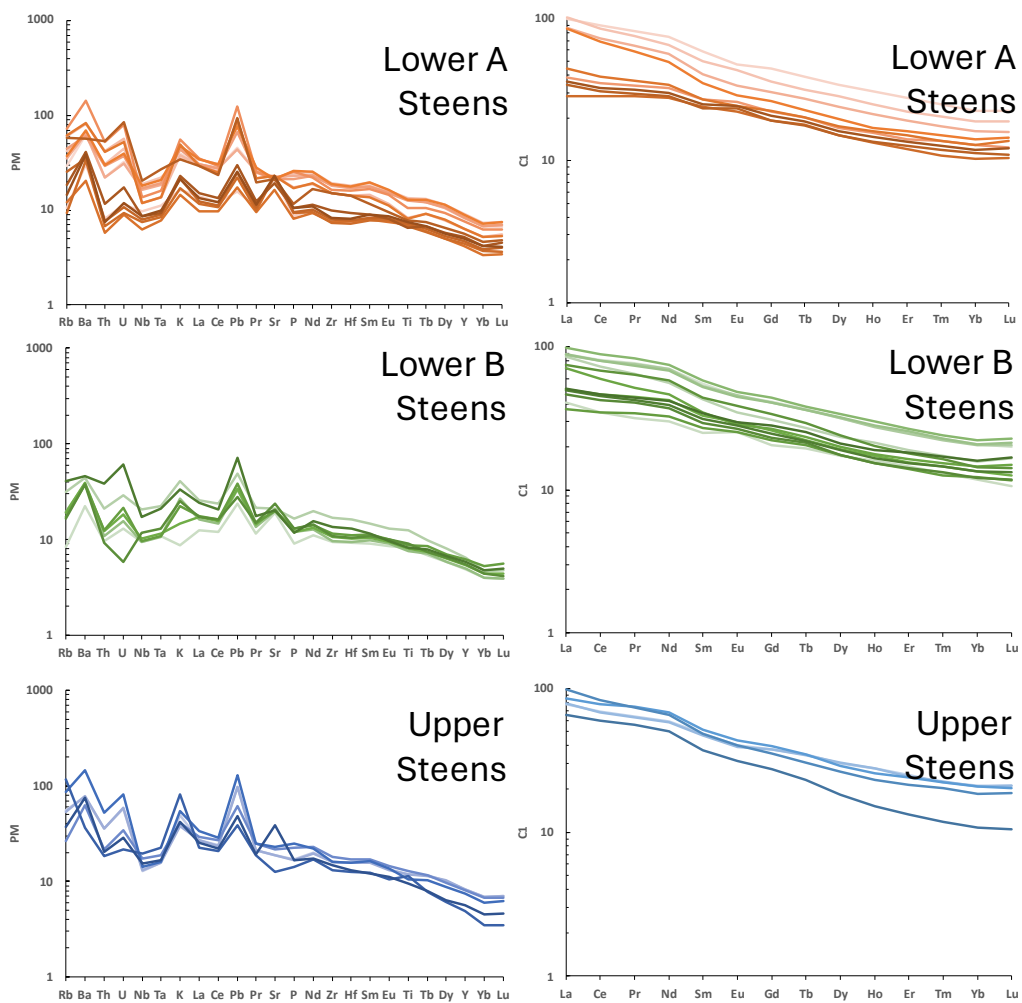


Figure 17: Trace and REE element diagrams of Steens dikes. Left hand column: trace element diagrams of Steens dikes, normalized to primitive mantle of Sun and McDonough (1989), separated by subunit. Right hand column: rare earth element diagrams of Steens dikes, normalized to C1 chondrite of Sun and McDonough (1995).

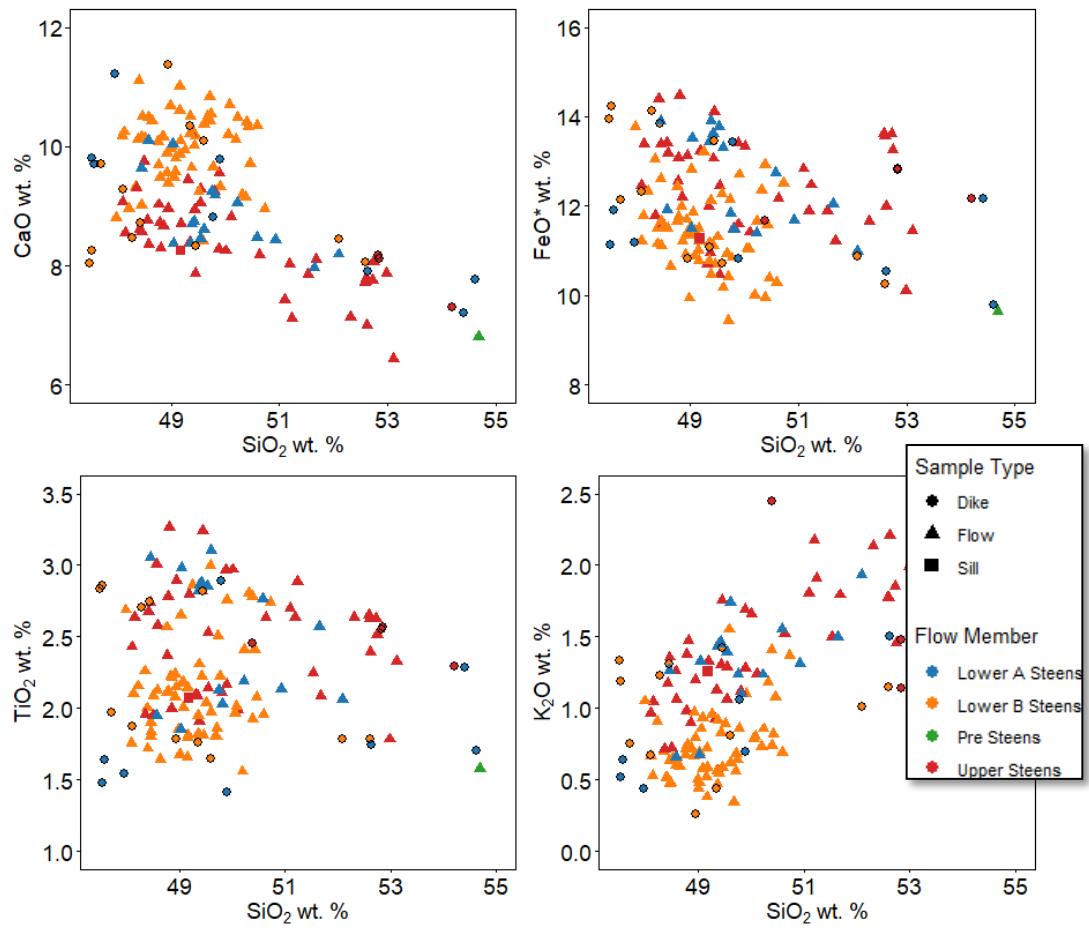


Figure 18: Plots of major element vs. SiO<sub>2</sub> wt. % of Steens Basalt and dike samples.

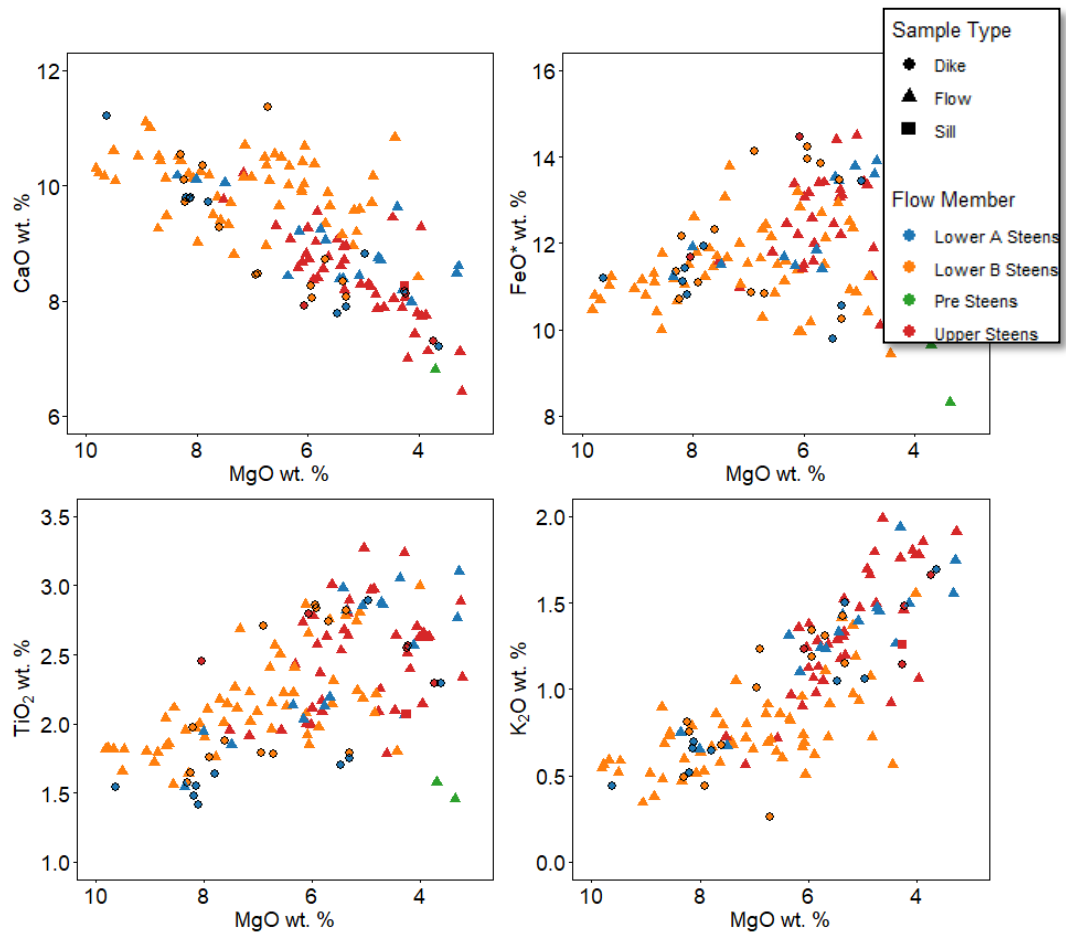


Figure 19: Plots of Major element vs MgO wt. % of Steens Basalt and dike samples.

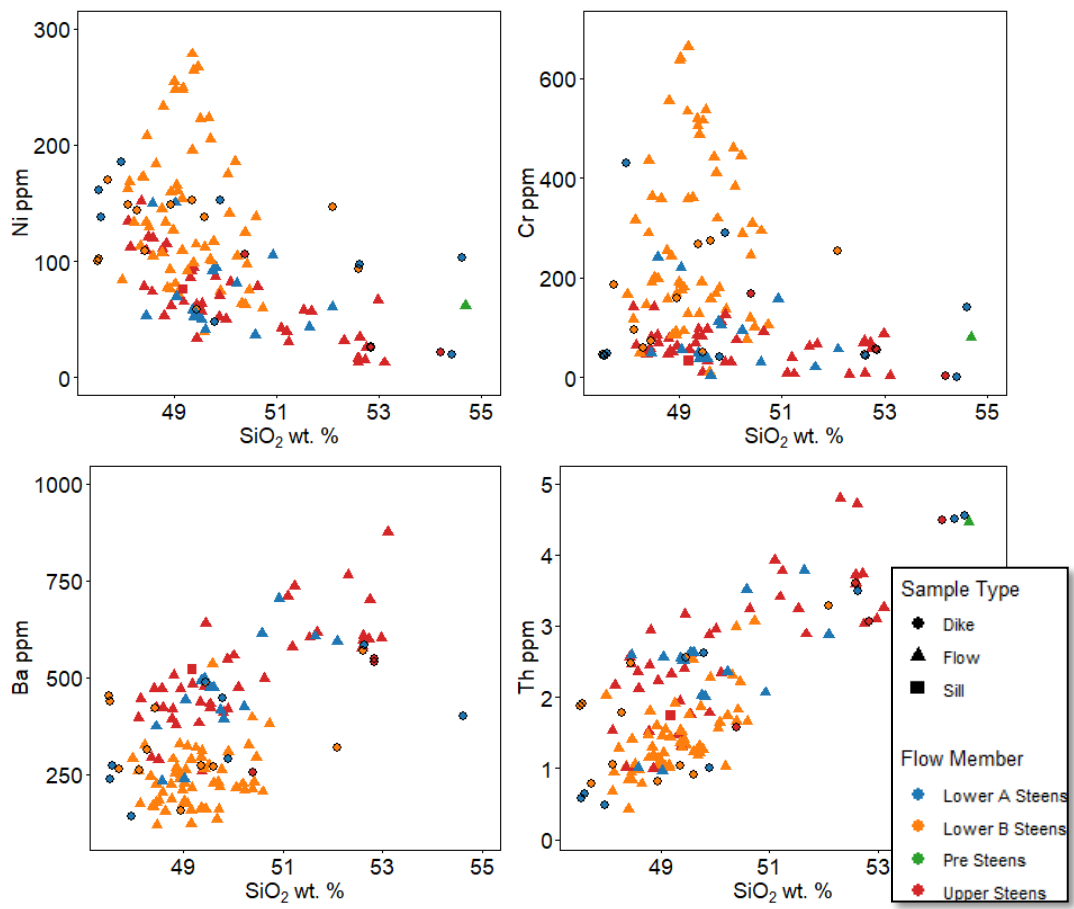


Figure 20: Plots of compatible and incompatible trace element vs. SiO<sub>2</sub> of Steens Basalt and dike samples.

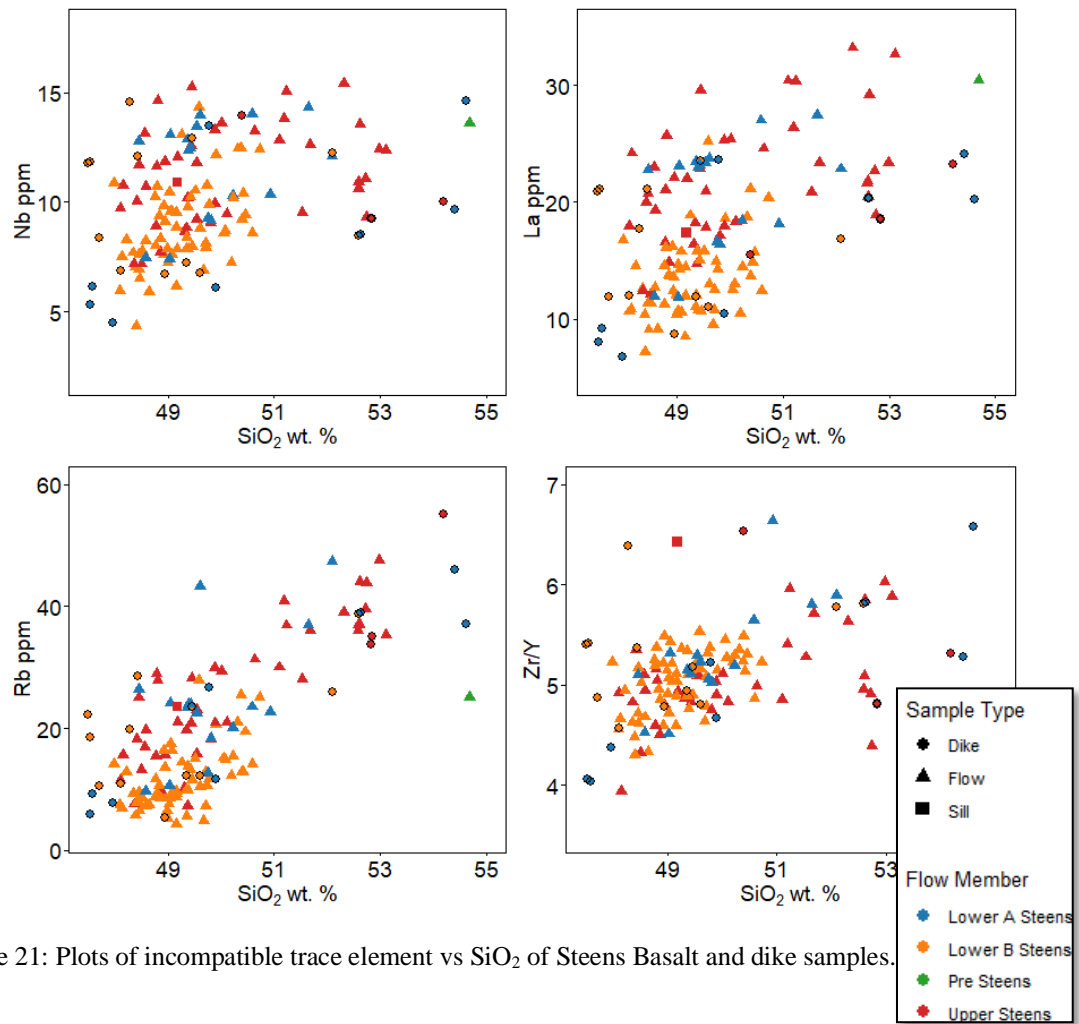


Figure 21: Plots of incompatible trace element vs SiO<sub>2</sub> of Steens Basalt and dike samples.

## GEOCHRONOLOGY

Groundmass and one phenocryst fraction were dated and reported on within the unpublished senior thesis of Ziff (2023) upon the samples listed in the previous methods section. Plateau ages for eight out of ten samples were concordant with their inverse isochron ages, with the exception of RS21M08 which was discordant by 0.02 Ma, and RS21M11A which only had a total fusion age due to a discordant spectrum. Samples with argon loss patterns (RS21M09, RS21M27, RS21M13) are regarded as minimum ages due to concave down spectra. It is indeterminate whether the age for RS21M28 is a maximum, minimum, or exact age due to discordant spectrum, however, it is statistically valid as there is agreement between plateau and isochron ages. All samples show recoil at high temperature heating steps, but due to low error, plateau creation, agreement between plateau and inverse isochrons, and agreeable mean standard weighted deviation (MSWD), recoil is not anticipated to have altered the results of the age dating. Results are listed in Table 5 below.

SAMPLE NAME	SELECTED PHASE	AGE (MA)	ERROR ( $\pm 2\Sigma$ )	MSWD
RS21M09	Phenocryst	15.61	0.22	1.48
RS21M27	Groundmass	15.99	0.05	0.59
RS21M26	Groundmass	16.18	0.17	1.58
RS21M08	Groundmass	16.35	0.03	1.01
RS21M21	Groundmass	16.58	0.03	0.77
RS21M30	Groundmass	16.59	0.03	0.77
RS21M28	Groundmass	16.64	0.07	1.19
RS21M15A	Groundmass	16.69	0.04	0.82
RS21M11A	Groundmass	17.00	0.04	N/A
RS21M13	Groundmass	17.27	0.05	1.12

Table 5: Geochronology results from Monument Dike Swarm samples.

## **FIELD**

With the above geochemical information and classification, field results can be presented with the geochemical identity of each sampled intrusive and are discussed and categorized as such below.

### ***MONUMENT DIKE SWARM***

A total of 37 new basaltic intrusive bodies in the form of dikes (31) and small sills (6) were sampled in this study, along with resampling of 6 dikes from Cahoon (2020) and six dikes of Fruchter and Baldwin (1979) (Figure 22). Strike and width for the other 16 dikes of Cahoon (2020) and Fruchter and Baldwin (1979) were assessed using Google Earth. Dikes primarily intrude into Izee, Baker, and Olds Ferry Terrane south of US 26, and through the John Day Formation and Clarno Formation volcanic deposits north of US 26. The only sills found in the region are along OR-409 between Monument and Hamilton, and along Little Cottonwood Road, near the towns of Monument and Hamilton.

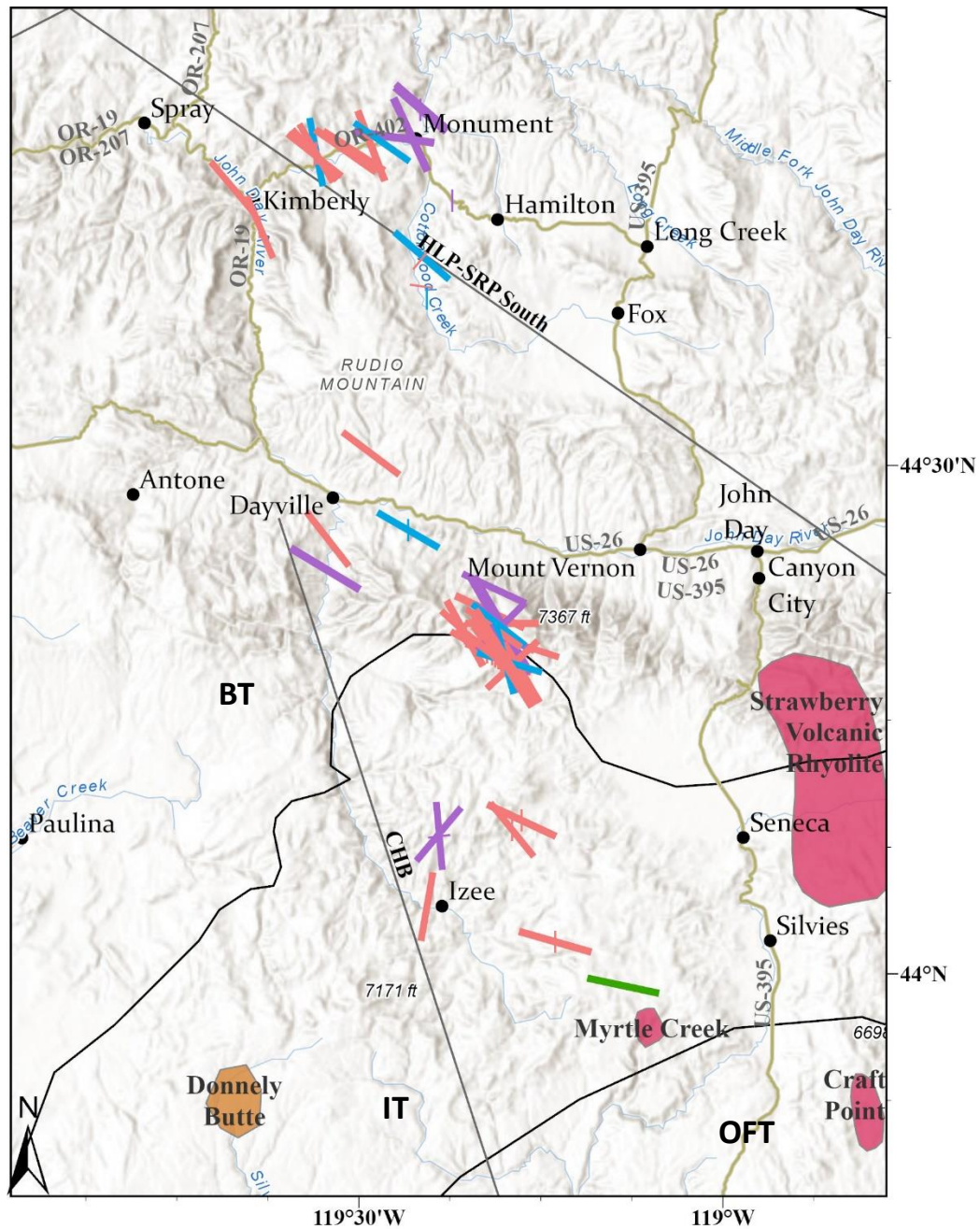


Figure 22: Map of the MDS field area, with geologic context. Blue polygon: Clarno and John Day formations; Pink polygons: co-eval felsic units up to 16.3 Ma (Streck et al., 2023); Orange polygon: co-eval felsic units up to 15.8 Ma (Streck et al., 2023); Purple lines: Twickenham subunit sampled dikes, oriented along strike; Blue lines: Monument subunit sampled dikes, oriented along strike; Salmon lines: Dayville subunit sampled dikes, oriented along strike; Green lines: High MgO subunit sampled dikes, oriented along strike; Black lines: terrane boundaries approximated from Dorsey and La Maskin, 2008, as well as Horton 2017; BT: Baker Terrane; IT: Izee Terrane; OFT: Olds Ferry Terrane; Black points: dikes from Cahoon et al., 2020; Stars: sampled during the 2021 & 2022 field season; Dashed gray lines: mapped normal faults of unknown age (Horton 2017).

Dikes ranged widely in width (Figure 23), with a largely bimodal distribution of widths in all four PGB subunits (Twickenham, Monument Mtn., Dayville, and high MgO). All dikes and sills of the Twickenham subunit belong to the Donnelly Basin flow member. These dikes were primarily between 8-10 m or ~30 m in width. The two Donnelly Basin sills sampled were outside of the town of Monument intruded in direct contact with one another (an upper and a lower, with an adjoining dike), represented as samples RS21M11B and RS21M11C, and were ~10-15 m in width respectively. Monument Mtn widths vary between flow members, primarily along a bimodal distribution. The Camas Creek flow member dikes are ~5 m in width or ~ 15 m in width. Franklin Mtn dikes are a bit larger, at 8 and 20 m widths, and virtually all Holmes Creek dikes range between 12-15 m. Only one Monument Mtn sill was sampled, of the Holmes Creek subunit, and was about 2-3 m in width. Dayville dikes were primarily ~8 m in width, however dikes of the Hamilton Mtn member are up to ~18m in width, and dikes of the Tamarack Mtn (Tam Mtn) are up to 30m in width.

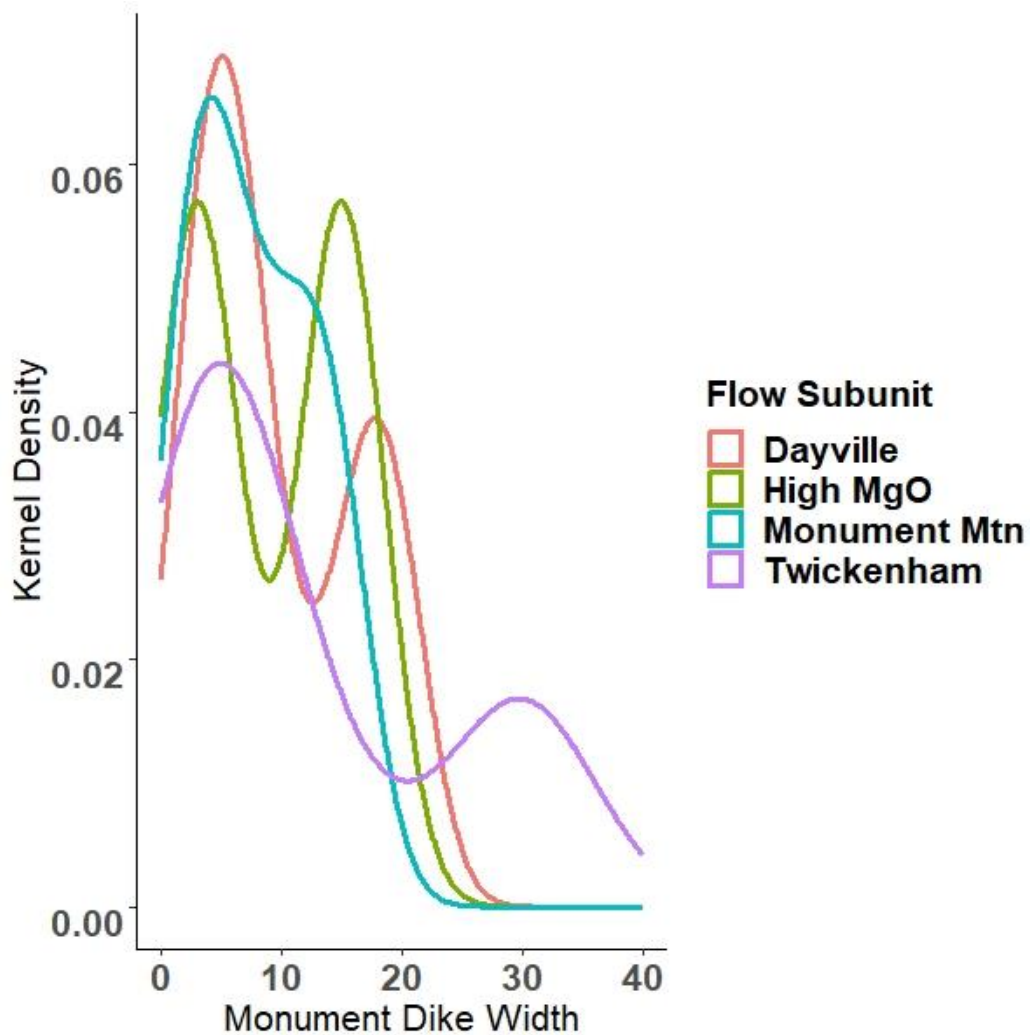


Figure 23: Subunit width distribution for sampled Monument Dikes.

Dike strike (Figure 24), across all subunits, largely parallel local normal faults. All dikes and nearby normal faults within < 3 km of the dike have a matching strike. The Twickenham and Dayville subunit dikes each have a mean strike of 305°, however, the Monument Mtn subunit dikes had a bimodal strike distribution, with some dikes striking between 305-315°, and a significant portion of the sampled dikes striking at 345°. There are outliers in all three subunits that strike nearly east-west, but this represents a small fraction of the sampled dikes.

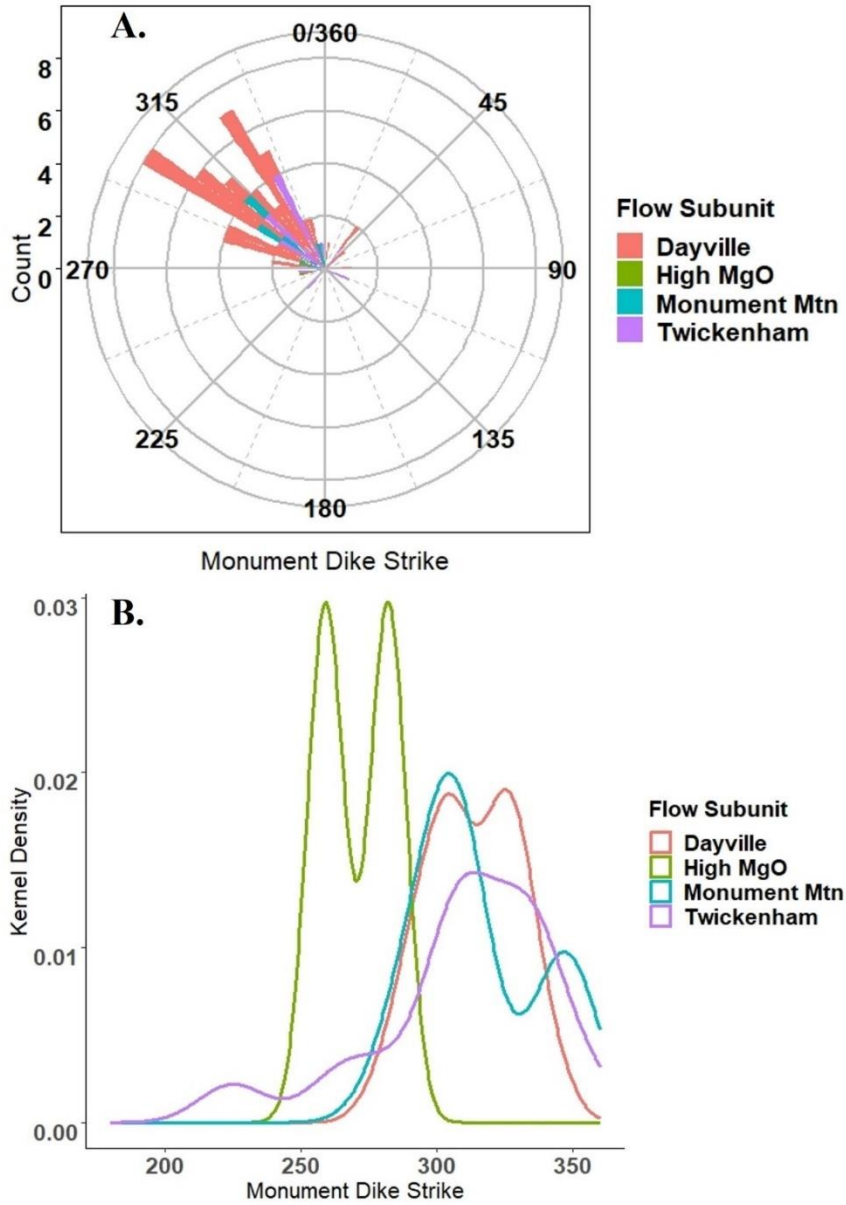


Figure 24: Rose diagram and distribution of sampled MDS dike strikes.  
 A: Rose diagram of the strikes of sampled Monument Dikes, colored by subunit. B: Distribution of the strike of sampled Monument dikes between 180-360°, by subunit.

No dikes were found that intruded or crosscut other dikes, apart from the two small sills and dike immediately west of the town of Monument, and two dikes immediately north of the town of Monument. Nearly all sampled intrusives showed uniform texture throughout the width of the dike, except for one sill of the Dayville subunit, which displayed glomerocrysts of olivine. Minimal to no zones of alteration were observed around most dikes, however, several that intrude into the John Day Formation showed small (5-10 m) zones of alteration, with the altered country rock enriched in Fe hydroxides and altered to clay minerals. Sills that intrude into the John Day formation also showed small to medium sized alteration zones in the country rock above the intrusion, similar to the effects of the dikes.

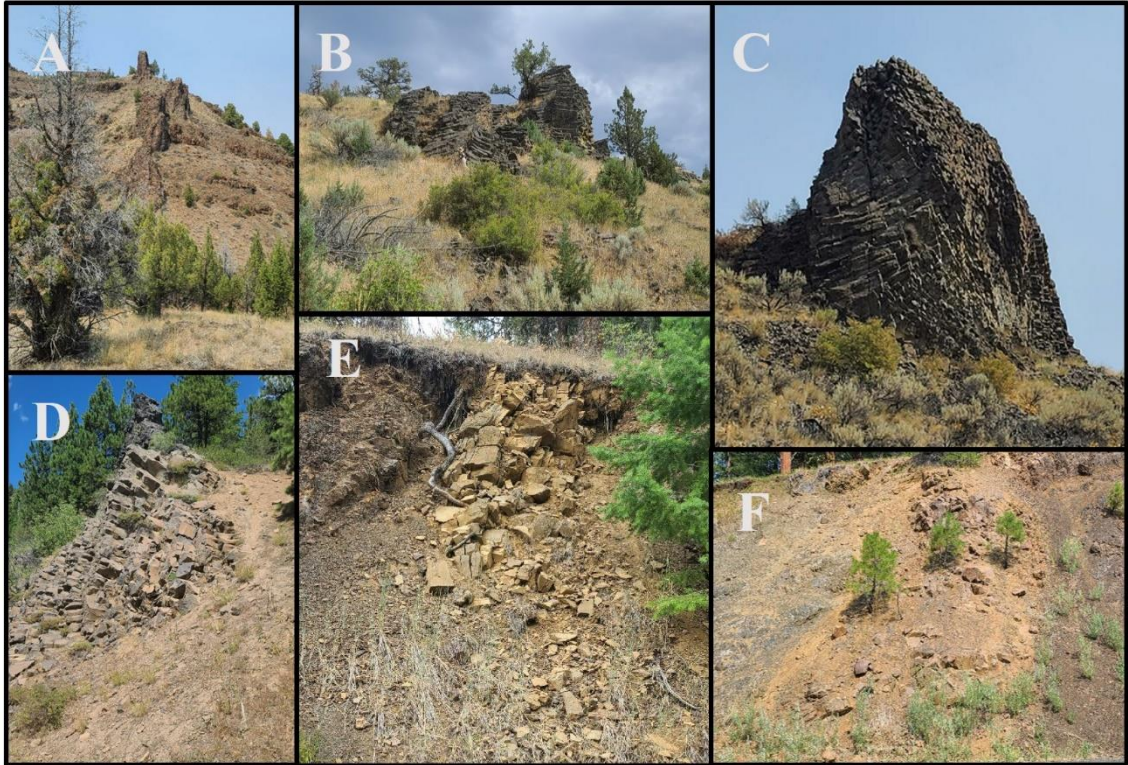


Figure 25: Monument dikes *in situ*.

A. Dike RS21M27, Dayville subunit, Monument Lookout flow member; B. RS22M44, Dayville subunit, Monument Lookout flow member. C. RS21M28, Twickenham subunit, Donnely Basin flow member; D. RS22M57, Monument Mountain subunit, Franklin Mtn flow member. E. RS21M32, Monument Mountain subunit, Camas Creek flow member. F. RS21M25, Dayville subunit, Hamilton flow member.

### ***STEENS DIKE SWARM***

A total of 19 new basaltic to basaltic andesite dikes were sampled (Figure 13, Figure 16). In addition to dikes, 15 samples along two transects of a newly discovered layered mafic-ultramafic intrusion (hereafter referred to as the Streck LMI) (Figure 26), and 5 hydrothermally altered dikes were sampled. Strike and dip were measured on all dikes observed in the field. Strike from the remaining 9 Moore and Grunder (2020a) dikes was determined through orthoimagery.

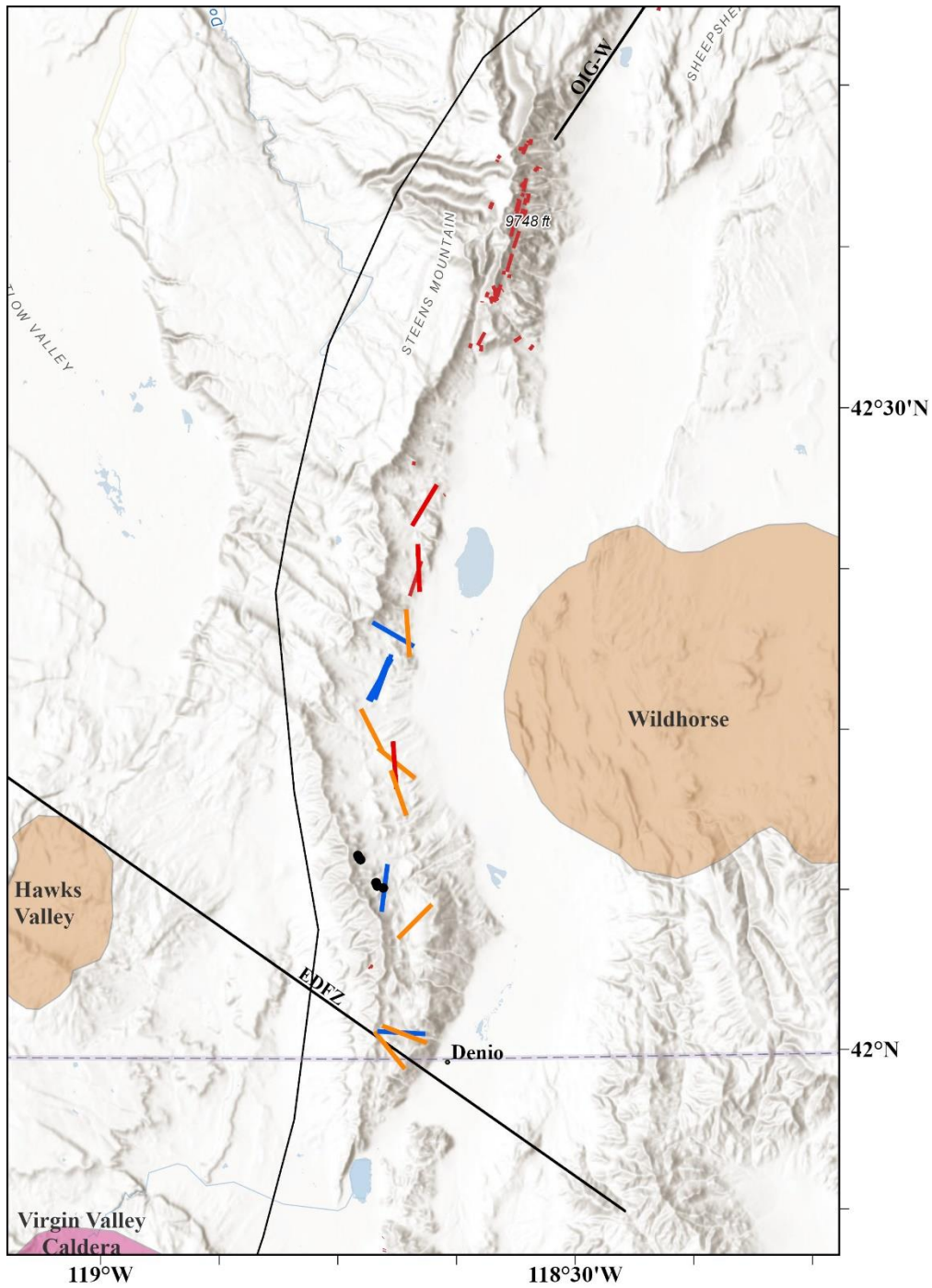


Figure 26: Map of Steens Dike Swarm field area.

Layered intrusive deposits: black points; Yellow lines: Pre-Steens subunit, oriented along strike; Green lines: Lower A Steens subunit, oriented along strike; Purple lines: Lower B Steens subunit oriented along strike; Pink lines: Upper Steens subunit oriented along strike; points indicated by stars were gathered by the author; points indicated by circles were gathered by Moore et al., 2020.; Gray lines: mapped normal faults of unknown age (Horton 2017); Solid red lines: Quaternary active faults (Machette et al., 2003); Light

orange polygons: co-eval felsic centers with a maximum age of 17.5 Ma (Streck et al. 2023); Magenta polygon: co-eval felsic centers with a maximum age of 15.8 Ma (Streck et al. 2023) Solid black line: terrane boundaries approximated from Dorsey and La Maskin, 2008, as well as Horton 2017; OFT: Olds Ferry Terrane; BRJT: Black Rock Jackson Terrane.

The widths of dikes of Lower A and Lower B Steens are primarily between 2-5 m (Figure 14), however, Upper Steens dikes are thicker, ranging between 3-7 m (Figure 15). No sills were discovered in the study region, however, to the south of Steens Mountain and the west of Pueblo Mountain a large, ~300-350m thick layered mafic-ultramafic intrusion was discovered (referenced as the Streck LMI hereafter) (Figure 16), with exposures extending across at least 5 km. Dike strike varies for all directly sampled subunits, paralleling normal faults in the region (Figure 14). Sixty-five dikes were mapped, and strike determined, through orthoimagery in the inaccessible regions of the SDS. Pre-Steens, Lower A Steens, and Lower B Steens dikes are exposed from the Oregon-Nevada border to the south and Pike Creek to the north, with strike ranging from ~350° to approximately 30°, following the curvature of the Steens Mountain Fault. The exception to this is the locations where the EDFZ, and a parallel lineament to the north, intersect the Steens Mountain Fault. Dikes exposed at these intersection points strike ~315°. Upper Steens dike exposures begin just to the north of the Pueblo Mountains and follow the same strike pattern as the Lower A and Lower B Steens. Dikes discovered through orthoimagery are classified as “undivided”, however, they are likely Upper Steens dikes, based on relative stratigraphy and cross cutting relationships, and strike between 15-25°.

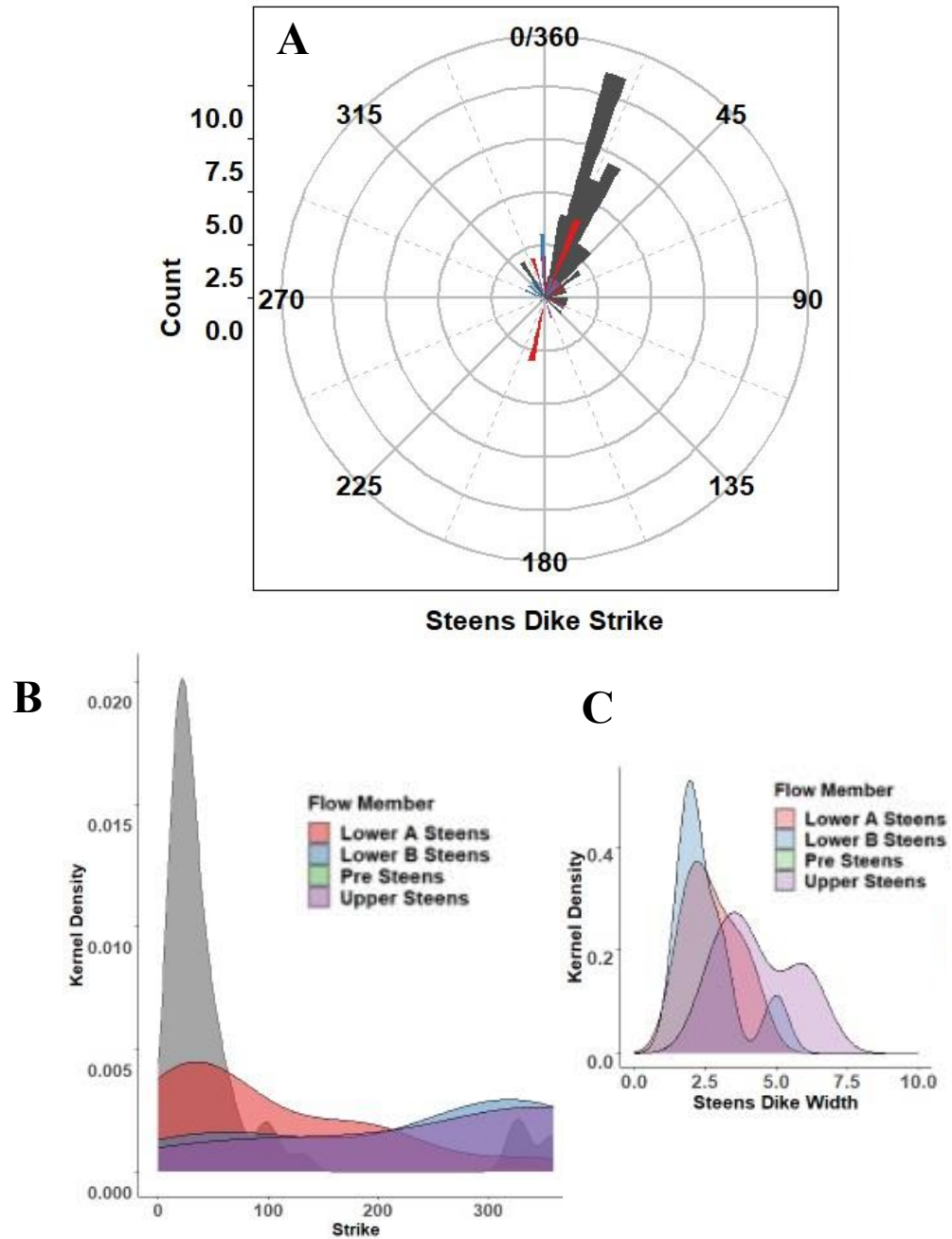


Figure 27: Rose diagram and distribution of strike and width of sampled Steens Dikes. A: Rose diagram of orthographically imaged dikes (gray) and sampled dikes, colored by flow member; B: Distribution of measured strikes, both orthographically (gray) and dikes sampled in this study, colored by flow member; C: Distribution of dike widths (in meters) by flow member.

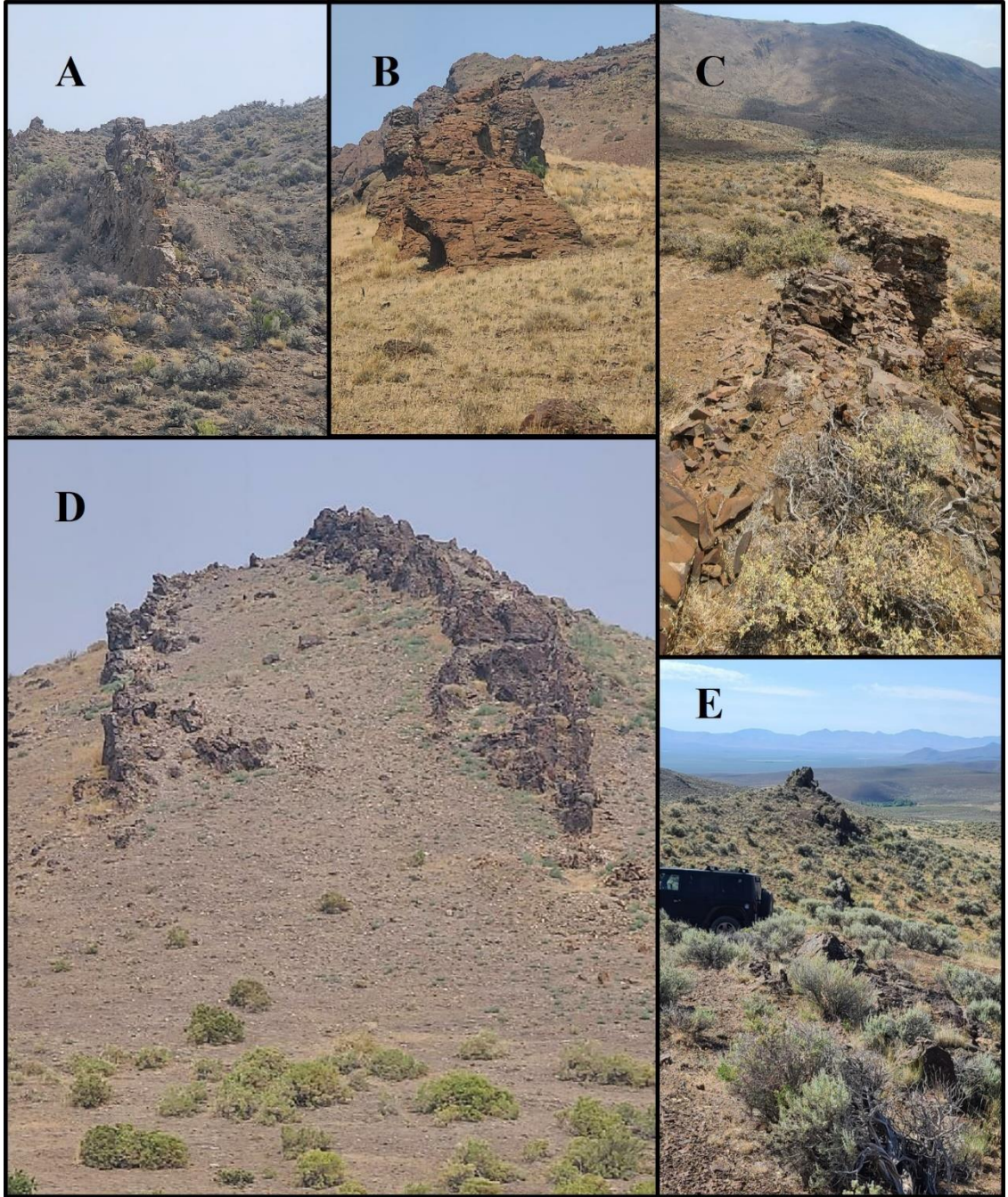


Figure 28: Steens dikes, in situ.

A: Dike RS21S05 (unknown subunit), with apparent argillic alteration. B: Upper Steens dike RS21S04. C: Lower B Steens dike RS21S18. D: Lower B Steens dikes RS21S02, RS21S03. E: Argillic altered dike RS22S20 (unknown subunit), running parallel to Catlow Valley Rd and the EDFZ.

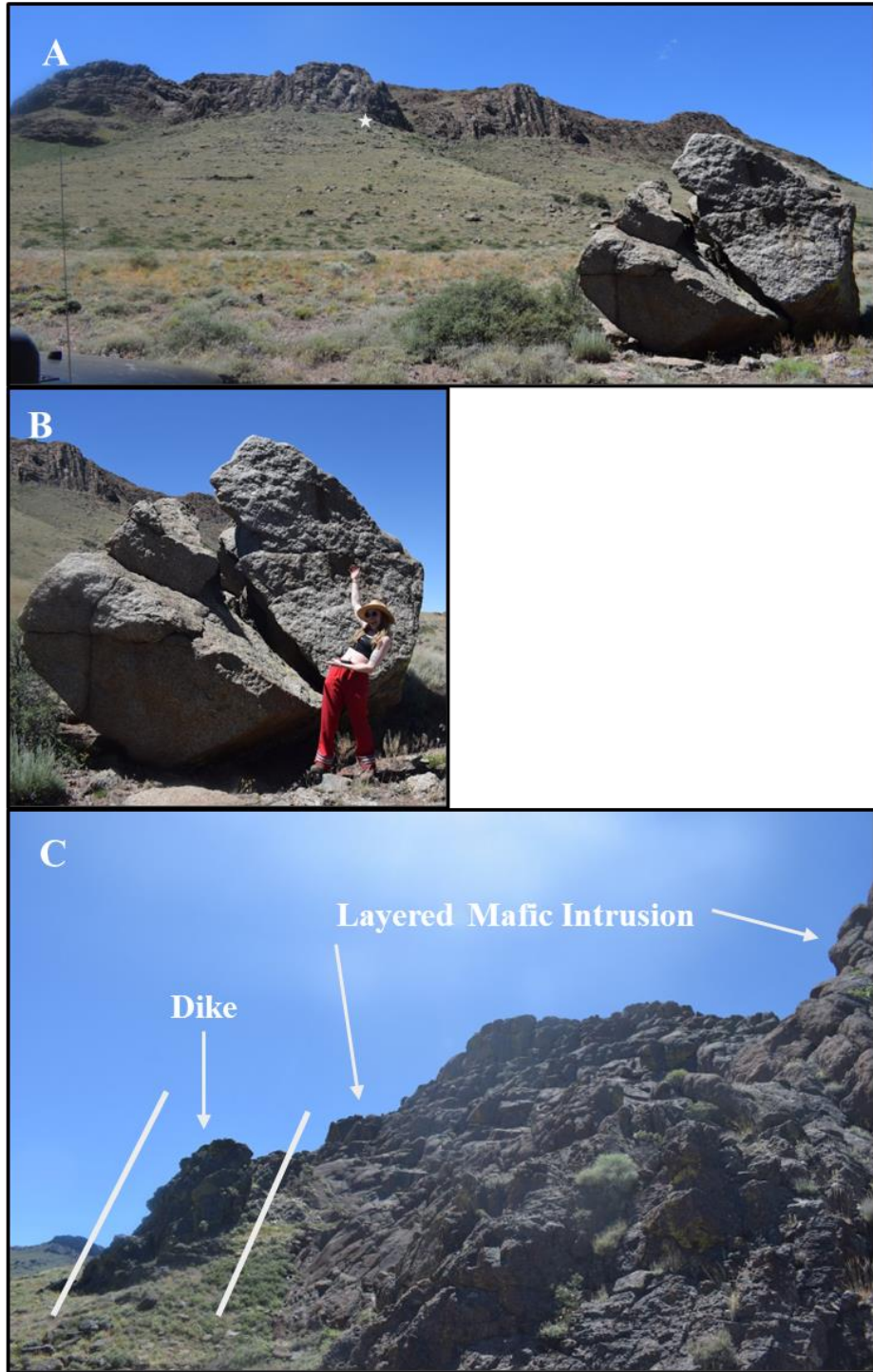


Figure 29: The Streck layered mafic intrusion.  
 A: The Streck layered mafic intrusion (Streck LMI), as the exposed cliff face in the background. B:  
 Boulder in foreground of A (rockfall of upper anorthosite layer) with field assistant Heather Ziff for scale.  
 C: Close up, side view of the Streck LMI, taken from the star in A.

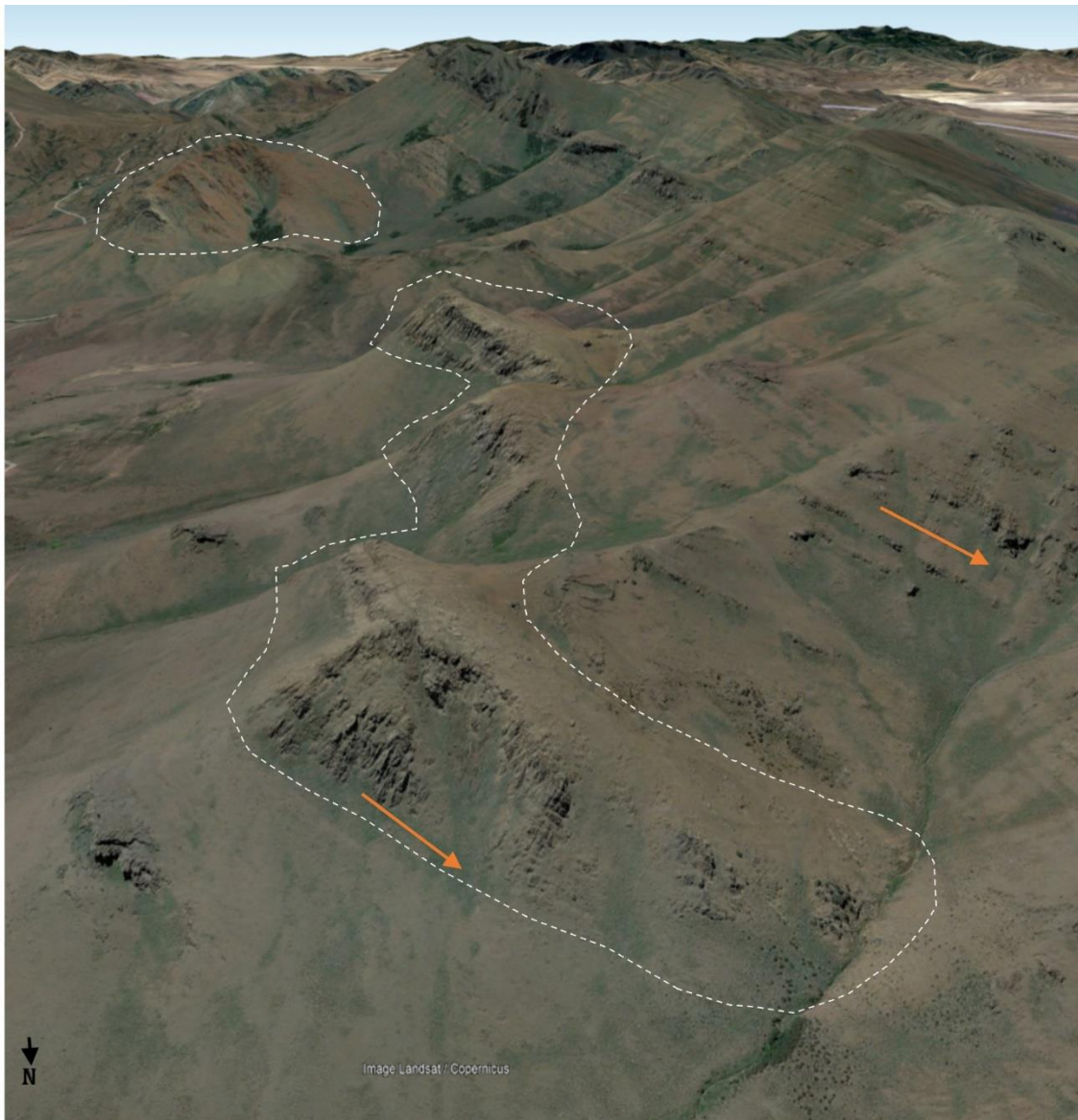


Figure 30: Google Earth view of the Streck LMI. White dashed polygon: exposures of the Streck LMI; Orange arrows: approximate dip angle of Streck LMI (lower) and Steens Basalts (upper).

Dikes primarily intrude through Black Rock-Jackson terrane and late Oligocene-early Miocene silicic volcanic rocks south of highway 205 (Catlow Valley Road). North of Catlow Valley Road, the dikes intrude through late Oligocene-early Miocene silicic volcanic rocks and Steens Basalt flows. Alteration, in the form of silicic, advanced

argillic to argillic, and propylitic alteration facies, is present throughout much of the southern portion of the study area. This large area and zonation of alteration appears to occur as a halo above and horizontally around the Streck LMI. This alteration halo extends from the eastern, northern, and southern implied borders of the Streck LMI, with the zones of greatest alteration occurring proximal to the exposure Streck LMI, and grading to zones of least alteration to the east of the Streck LMI. Abundant supergene mobilization of Cu and other base metals are present in the form of Fe hydroxides, chrysocolla, chalcocite, and malachite, with the number of exposures of these deposits increasing in proximity to the Streck LMI. Also proximal to the Streck LMI are numerous quartz-basalt-phyllite breccia veins and stringers that contain veins of base metal sulfides (chalcopyrite  $\pm$  bornite) and their oxidation products (Fe hydroxides, chalcocite, chrysocolla, malachite, azurite). Farther to the east are numerous quartz-phyllite-basalt breccia veins and stringers with abundant deposits of specular hematite and malachite.

## **PETROGRAPHY**

### ***MONUMENT DIKE SWARM***

A total of nine dikes and two sills from the Monument Dike Swarm were selected for petrographic thin sections. All sampled dikes can be loosely categorized by being either fine grained, medium coarse grained, very coarse grained, or porphyritic.

The overall texture of Twickenham dikes is primarily very coarse to porphyritic, with sample RS21M28 containing phenocrysts primarily of 3-5mm plagioclase  $\pm$  1-2 mm clinopyroxene with minor olivine (>1%), with phenocryst content approximately 15%.

Plagioclase phenocrysts are euhedral to subhedral in shape, while the clinopyroxenes ranged between subhedral to anhedral. The groundmass texture of this sample is intersertal, with glass and pyroxene surrounding plagioclase microlites.

The Monument Mountain, Holmes Creek sill sample (RS21M13) is phenocryst poor, with <1% of 2-4mm plagioclase phenocrysts. The groundmass is coarse (1-2 mm crystal size) and consists primarily of plagioclase (~60%) and pyroxene (orthopyroxene ~15%, and clinopyroxene ~10%) and Fe-oxides. The Holmes Creek member dike sample (RS21M19) shows a similar mineralogy; however, the texture is very different. This sample is medium coarse-grained with 2-4 mm groundmass and consisted of a large number of very embayed phenocrysts of clinopyroxene and plagioclase, and the overall texture is intersertal.

Most Dayville are texturally diverse, with some samples having a fine-grained, phenocryst poor groundmass, to medium coarse and porphyritic, with the Johnny Cake and Monument Lookout members being glomeroporphyritic. Olivine is largely absent as phenocryst phase in all samples, however sample RS21M21 contained pseudomorphs after olivine. Phenocryst phases throughout all samples, including the glomeroporphyritic samples, were dominated primarily by plagioclase  $\pm$  clinopyroxene. Phenocryst abundance was 20-25% in the Hamilton, Johnny Cake, and Monument Lookout flow members. Phenocryst abundance was significantly lower (3-10%) in the Dale, Branson Creek, and Hamilton flow members. Most flow members also show a relatively fine to medium (<1 mm - 1.5 mm) groundmass of plagioclase microlites or laths, with minor clinopyroxene, and are intergranular in texture. Most samples showed

no preferred orientation, for either groundmass or phenocrysts, however the two samples with plagioclase and clinopyroxene glomerocrysts (Monument Lookout and Johnny Cake) show preferred orientation of the phenocrysts and groundmass, respectively. Poikilitic texture was observed in the Branson Creek flow member sample and shows a fine groundmass of Fe-Ti oxide minerals and plagioclase microlites.

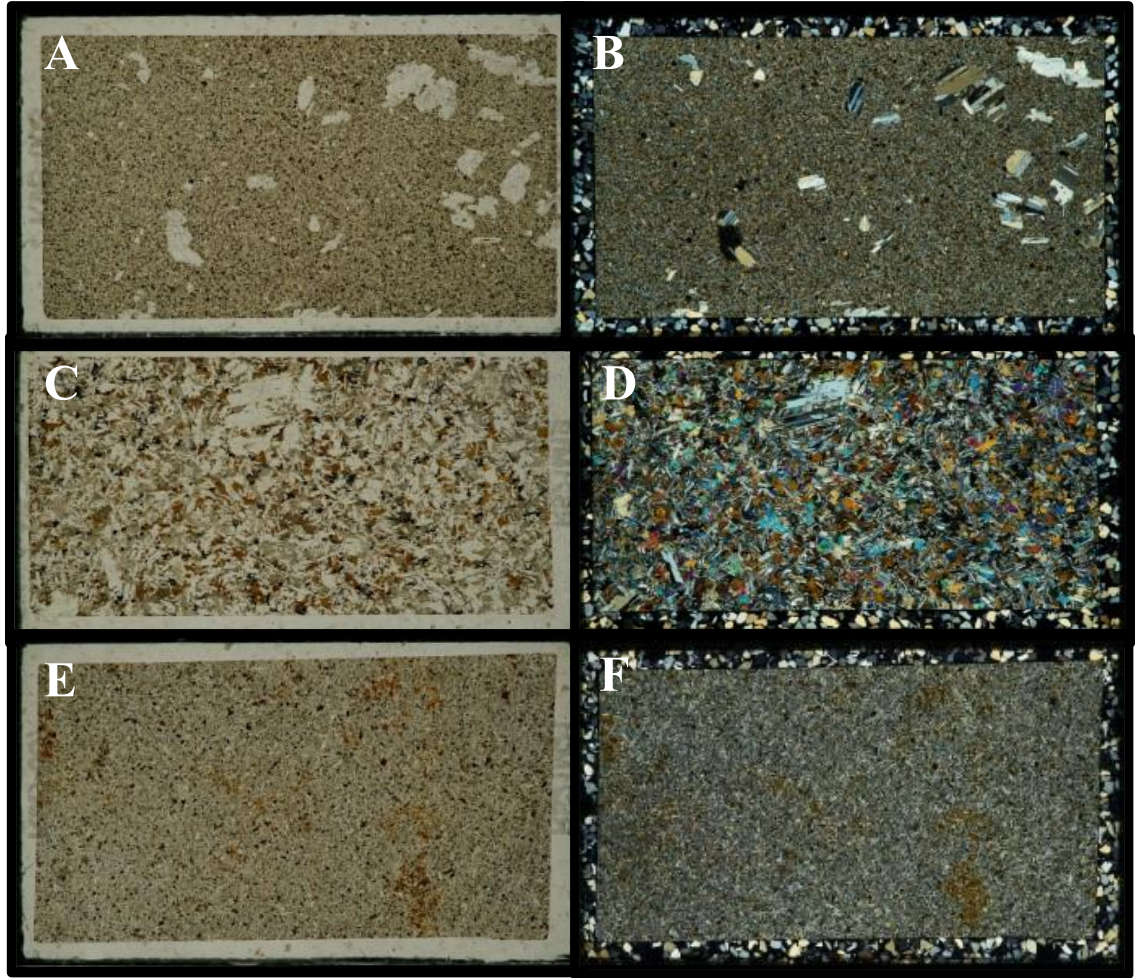


Figure 31: Petrographic images of fine grained, coarse grained, and porphyritic MDS samples. Field of view is 27x46mm in both plane polarized and cross polarized light (PPL and XPL respectively). A & B: Porphyritic textured RS21M15A in PPL and XPL (respectively), of the Dayville subunit and Branson Creek flow member. C & D: Very coarse textured RS21M19 in PPL and XPL (respectively), of the Monument Mtn subunit and Holmes Creek flow member. E & F: Fine grained, phenocryst poor RS21M21 in PPL and XPL (respectively), of the Hamilton flow member of the Dayville subunit.

### ***STEENS DIKE SWARM***

A single Lower A Steens sample (RS21S08) is characterized by a sub-ophitic groundmass of plagioclase and granular clinopyroxene + orthopyroxene-oxide crystals. The Lower B Steen subunit samples varied significantly. Sample RS21S01 is similar in texture and composition to the Lower A Steens, however, the plagioclase laths have intersertal olivine, clinopyroxene, and orthopyroxene crystals. Another sample, RS21S05 was also ophitic in texture, however, the pyroxene phenocrysts are almost entirely intergrown with 1mm plagioclase laths, and a very minor -4 mm plagioclase phenocrysts. Samples RS21S05 and RS21S01 were composed of ~40% plagioclase, 35% orthopyroxene and 15-20% clinopyroxene, with minor amounts of olivine ± Fe oxide minerals. Two samples (RS21S09 and RS21S18) are aphyric, with their groundmass composed nearly entirely of plagioclase, with small subeuhedral grains of clinopyroxene + Fe oxides in the interstices. Samples RS21S09 and RS21S18 were composed almost entirely of plagioclase with minor amounts of clinopyroxene + olivine + Fe oxide minerals.

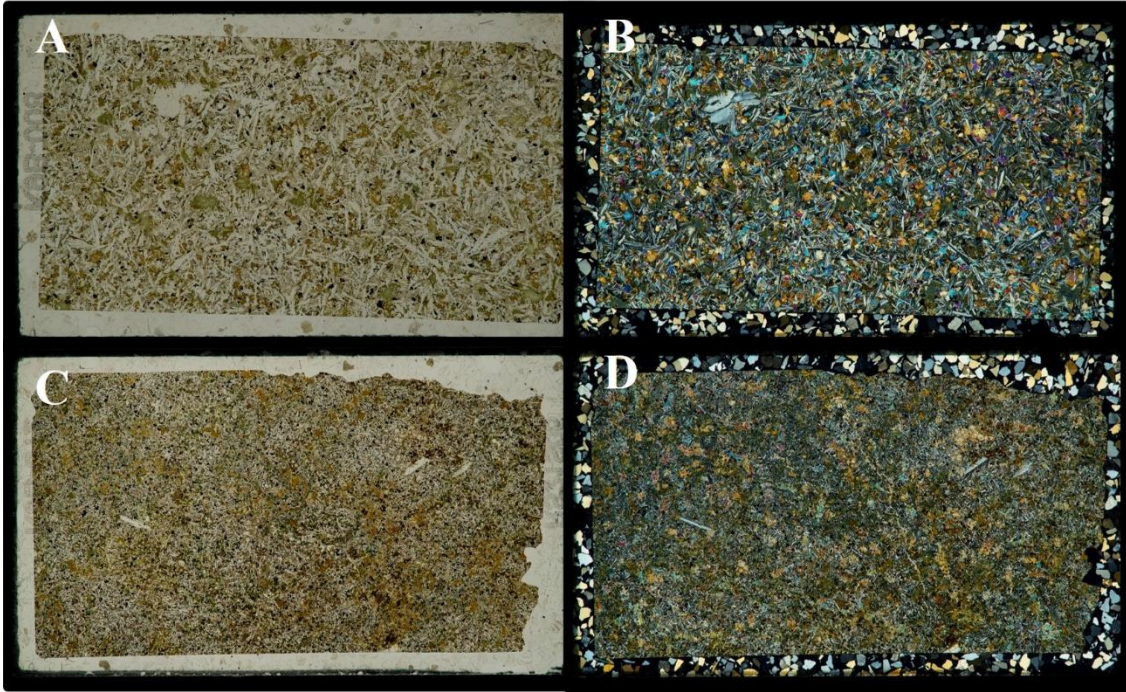


Figure 32: Petrographic images of select Steens dikes. Field of view is 27x46mm in both plane polarized and cross polarized light (PPL and XPL respectively). A & B: RS21S08 in PPL and XPL (respectively), of the Lower A Steens subunit. C & D: RS21S05 in PPL and XPL (respectively), of the Lower B Steens subunit.

### ***STRECK LAYERED MAFIC INTRUSION***

Samples of the Streck LMI exhibit a cumulus texture throughout, with varying mineral mode depending on stratigraphic position. The lower most layer of the first transect is in contact with the dike intruding the Streck LMI, sampled as RS22S28A and B, and RS22S30A and B, which shows an ophitic texture and mineral mode primarily of phenocrysts of plagioclase, orthopyroxene, olivine and minor clinopyroxene and Fe-Ti oxides. Groundmass crystal size grows larger towards the interior of the layered intrusion, as evidenced by RS22S28B2, which contains an anorthosite portion of the

layered intrusion as well as a portion of the dike that crosscuts the intrusion. Sample RS22S28C is an Fe-Ti anorthosite with large, elongated plagioclase phenocrysts that are largely euhedral to subhedral, 1-2 cm long, and that are complexly zoned and twinned (Figure 33C, 33F). Subhedral to anhedral Fe-Ti oxides, as well as minor clinopyroxene, orthopyroxene, olivine, 1-5 mm in size, are found in the interstices among plagioclase. Samples RS22S28D and RS22S28E (Figure 33E, 33F) contain slightly larger and more complexly twinned plagioclase, and lesser amounts of pyroxene minerals compared to RS22S28C in the interstices of the plagioclase crystals. The interstices of the plagioclase crystals are instead primarily composed of rounded grains of olivine and Fe-Ti oxides. There is a notable vein of larger disseminated subhedral Fe-Ti oxide crystals through the center of the sample RS22S28D. Phenocryst size grows even larger (>3cm), and the interstices are filled with rounded grains of olivine and clinopyroxene. Sample RS22S30C is an olivine melagabbro, and contains 30% clinopyroxene, 30% olivine, 30% plagioclase, and minor amounts of orthopyroxene and oxides (Figure 33A, 33B). This sample is the most olivine rich unit of the intrusion and appears to be the olivine and clinopyroxene cumulate layer. A portion of the sample RS22S30D contains much finer grains, grading from larger plagioclase (0.5 - 1 cm in length) and clinopyroxene crystals (2 - 4 mm in length) to finer 1 -2 mm plagioclase crystals with intergranular olivine and clinopyroxene. The larger phenocrysts are subhedral, and angular. The final sample, RS22S30E, is an anorthosite sample, with minor amounts of clinopyroxene. The majority of the clinopyroxene occurs in small, rounded crystals in the interstices of the plagioclase. A small population of clinopyroxene (three 0.75 - 1 cm crystals) show strong ophitic texture and are intergrown with 4 - 8 mm long plagioclase laths.

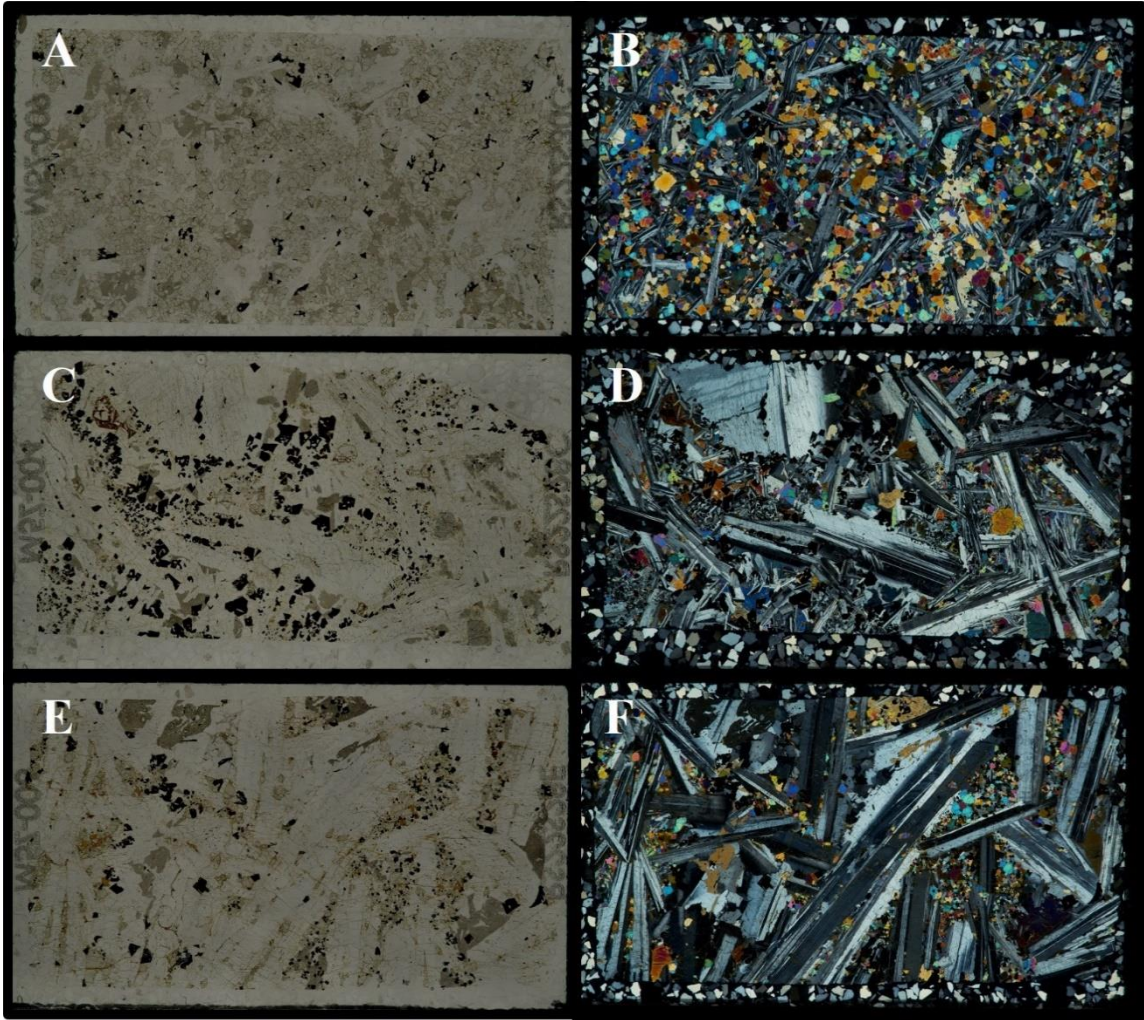


Figure 33: Petrographic images of select Streck LMI samples.

Field of view is 27x46mm in both plane polarized and cross polarized light (PPL and XPL respectively). A & B: RS22S30C, an olivine melagabbro layer, in PPL and XPL (respectively), showing accumulation of olivine and pyroxene. C & D: RS22S28C, an anorthosite layer in PPL and XPL (respectively), showing accumulation of Fe-Ti oxides interstitial to large phenocrysts of plagioclase. D & E: RS22S30E, outer anorthosite layer, in PPL and XPL (respectively), showing accumulation of plagioclase, primarily labradorite and bytownite.

## DISCUSSION

### PICTURE GORGE BASALT/MONUMENT DIKE SWARM

#### *CLASSIFICATION, GEOCHEMISTRY, AND GEOCHRONOLOGY*

Flow subunit classification of the samples gathered during this study had robust calculated accuracy and probability scores for each subunit, namely the Twickenham, Monument Mtn., and Dayville subunits (0.86-0.88 calculated accuracy using a random forest machine learning model). When plotted on geochemical discrimination diagrams (i.e. Figures 9-15), samples classified specifically by subunit (i.e. Twickenham, Dayville, etc.) largely conform to established trends and clusters from previous studies. Flow member classification also had robust calculated accuracy and probability scores. When plotted on geochemical discrimination diagrams, these also largely fell within previously established clusters from other workers, however, significantly greater scatter occurs when compared to the geochemical distributions of original flow member compositions established by Bailey (1989). That being said, on closer examination, there are several samples whose flow member designation of this study and previous studies were inconsistent (i.e. two samples from Cahoon 2020 and one sample from this study were classified as Monument Mtn, Stony Creek, but consistently plot on or very close to a sample classified as Alder by Bailey 1989). These inconsistencies are likely due to issues with the original stratigraphy and the classification system, rather than an error with the machine learning model. These errors are discussed in greater detail below.

The subunit/flow member classification system was established by Bailey (1989) based on 35 geochemical analyses of samples collected from the type locality of Picture Gorge region. He established subunits and flow members based on textural and phenocrystic characteristics as well as by  $\text{TiO}_2$  and  $\text{MgO}$  content combined with stratigraphic context. A potential source of classification errors is the fact that sampling bias was introduced in the following way. Many flow members are represented by a single sample while other flow members were disproportionately sampled (i.e. Donnelly Basin samples,  $n=9$ ). As machine learning is largely based on principal component analysis and k-means clustering, this disproportionately weights classification towards flow members with greater sample representation and away from flow members with fewer samples within the teaching dataset. This sampling bias is also further exacerbated by the fact that the Donnelly Basin member was a large flow that filled a basin, and as such, had a longer cooling history when some compositional differentiation may have occurred as suggested by Bailey (1989). If true, compositional variable flows would even further increase the uncertainty error, as this leads to greater compositional range and to overlap with other flow member introducing a bias into the training and classification methods for classifying any sample later based on data by Bailey. Wolff et al. (2008) reanalyzed 21 of Bailey (1989) samples, yielding high precision compositional data of a full suite of elements by XRF and ICPMS. Cahoon (2020) and Cahoon et al. (2023) increased this high precision compositional database by another 168 samples, effectively quadrupling the geochemical database, and a principal component analysis was utilized for subunit and flow member classification, based on Bailey (1989). The combined data by Wolff et al., Cahoon, and this study allow for better defining subunits. As a result, the subunit

designation by Bailey, as this was largely based on stratigraphic context, phenocryst content and composition, and textural variation between flows, is called into question. This in turn suggests that geochemical classification and assignments need to be revisited. One way to address this is to evaluate geochemical trends and clusters and use these to establish subunits. Doing so suggests there are two rather than three primary geochemical trends/clusters: the Dayville trend and the Twickenham-Monument Mountain trend (referred to hereafter as the Twickenham trend or subunit). During the original classification by Bailey (1989), the Dayville, Twickenham, and Monument Mtn subunits appear as distinct (albeit overlapping) clusters, which, at the time, implied that these were three distinct subunits, yet Bailey (1989) noted the similarities between Twickenham and Monument Mountain samples. With the addition of the data of Cahoon (2020) and this study, it becomes clear that samples classified as Dayville define a, more or less, single distinctive trend, and samples classified as Twickenham and Monument Mtn define a relatively distinctive trend, with *High MgO* samples plotting at the most primitive end of each respective trend (Figures 34, 35). In all geochemical diagrams (Figures 9 through 15), the Monument Mtn subunit seemingly represents the more evolved Twickenham compositions. Because of this, I propose here that the subunit of Monument Mountain should no longer be considered as a distinct subunit and should henceforth be merged with the Twickenham subunit. Consequently, this would lead to two subunits of Dayville and Twickenham, with the *High MgO* samples occurring as parental members of each trend. This helps to resolve issues with obtained radiometric ages of Cahoon (2020) and this study, as well as with the stratigraphy established by Bailey (1989). In the type locality of Picture Gorge, Twickenham forms the basal flows,

followed by Monument Mountain flows, and in turn followed by Twickenham flows. However, Cahoon (2020) found that in many locations, Monument Mountain flows are the stratigraphic basal unit with ages that make them coeval with Twickenham flows. Merging these two subunits would alleviate these inconsistencies and lead to stratigraphic integrity both in the type locality as well as in the extended distribution of Picture Gorge Basalt flows.

Flow member designation was also established by Bailey (1989), using the same methods discussed in previous sections of this study. In recognition of the much larger extended distribution established by Cahoon (2020), it is likely that there are more flow units than those within the area of the type locality. This, in turn, would imply that a re-evaluation of flow members is needed, with the likely outcome of new or revised flow member definitions. This, however, is not within the scope of this study at this time. Further discussion of the Picture Gorge Basalt will reflect these revised subunits and will not consider flow member classification. This can be revisited in later studies.

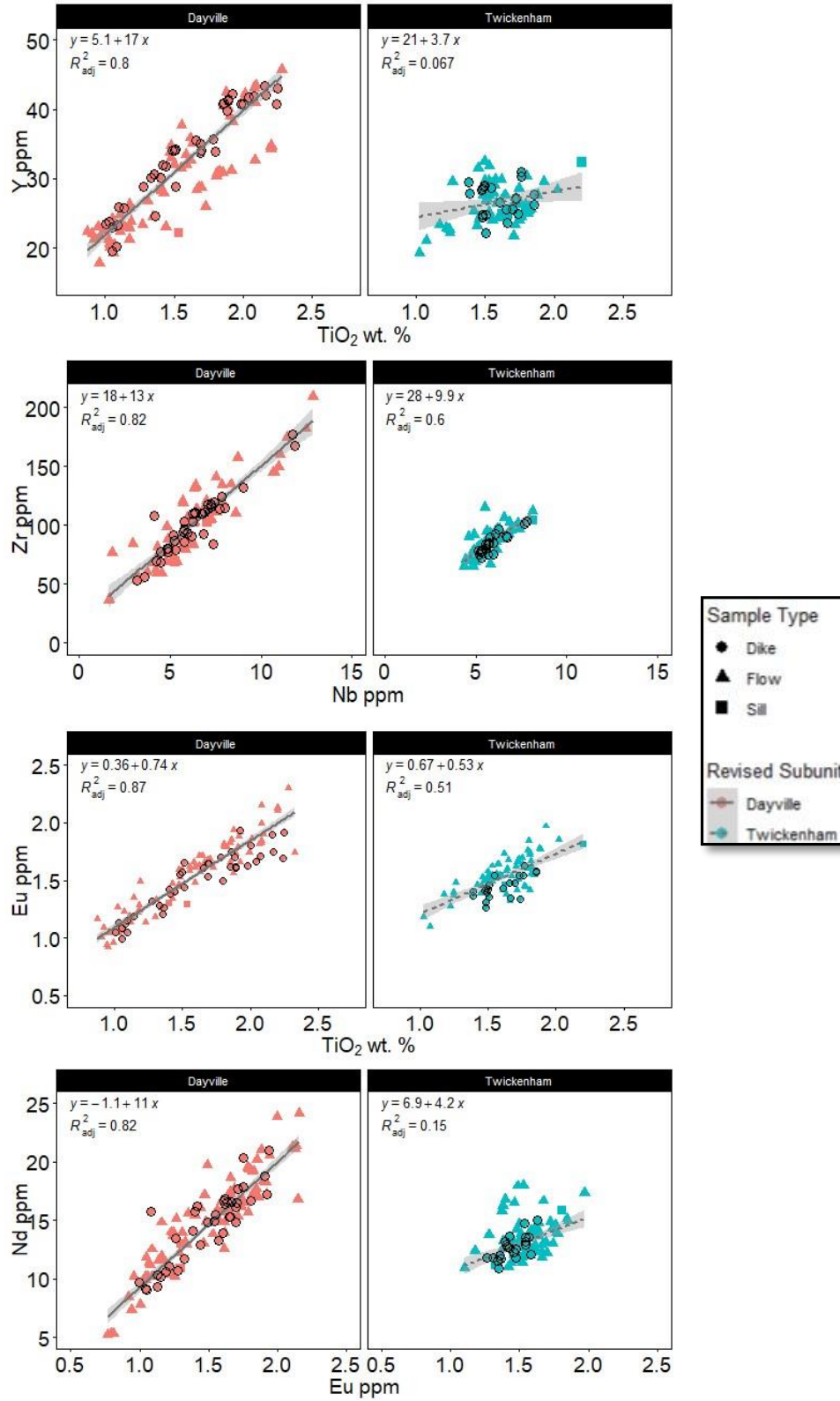


Figure 34: Elemental comparison diagrams of Twickenham, and Dayville trends.

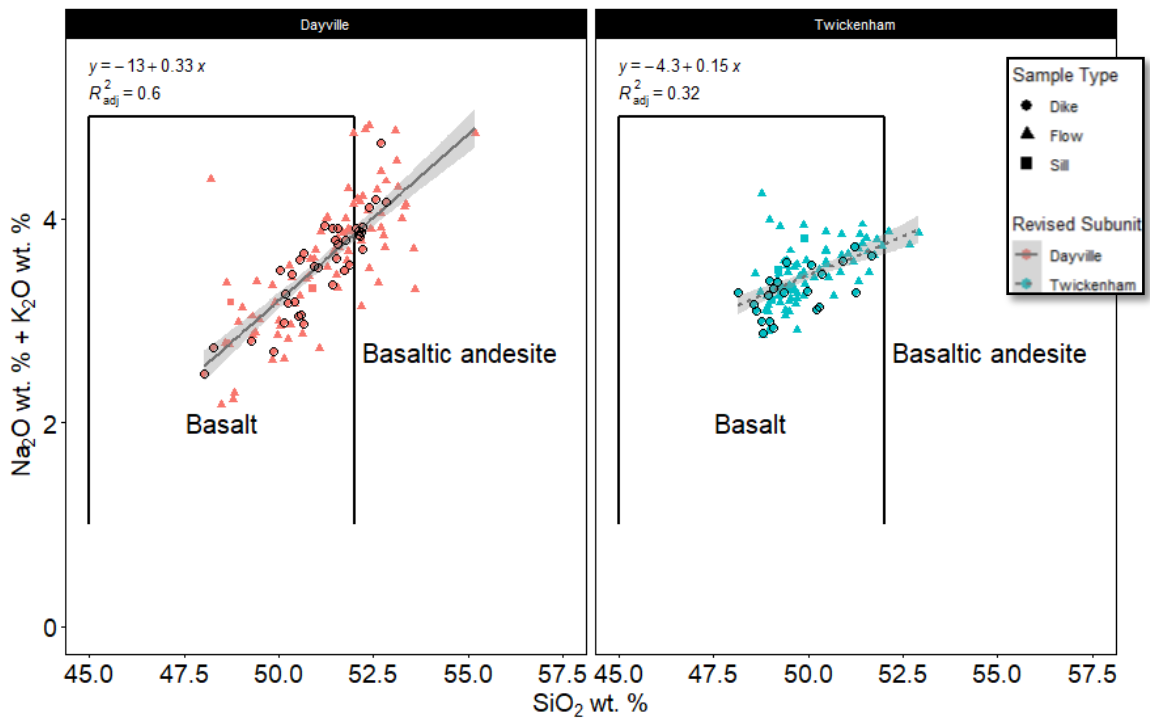


Figure 35: Total alkali-silica diagram (Le Bas et al., 1986) of PGB samples using new subunit classification.

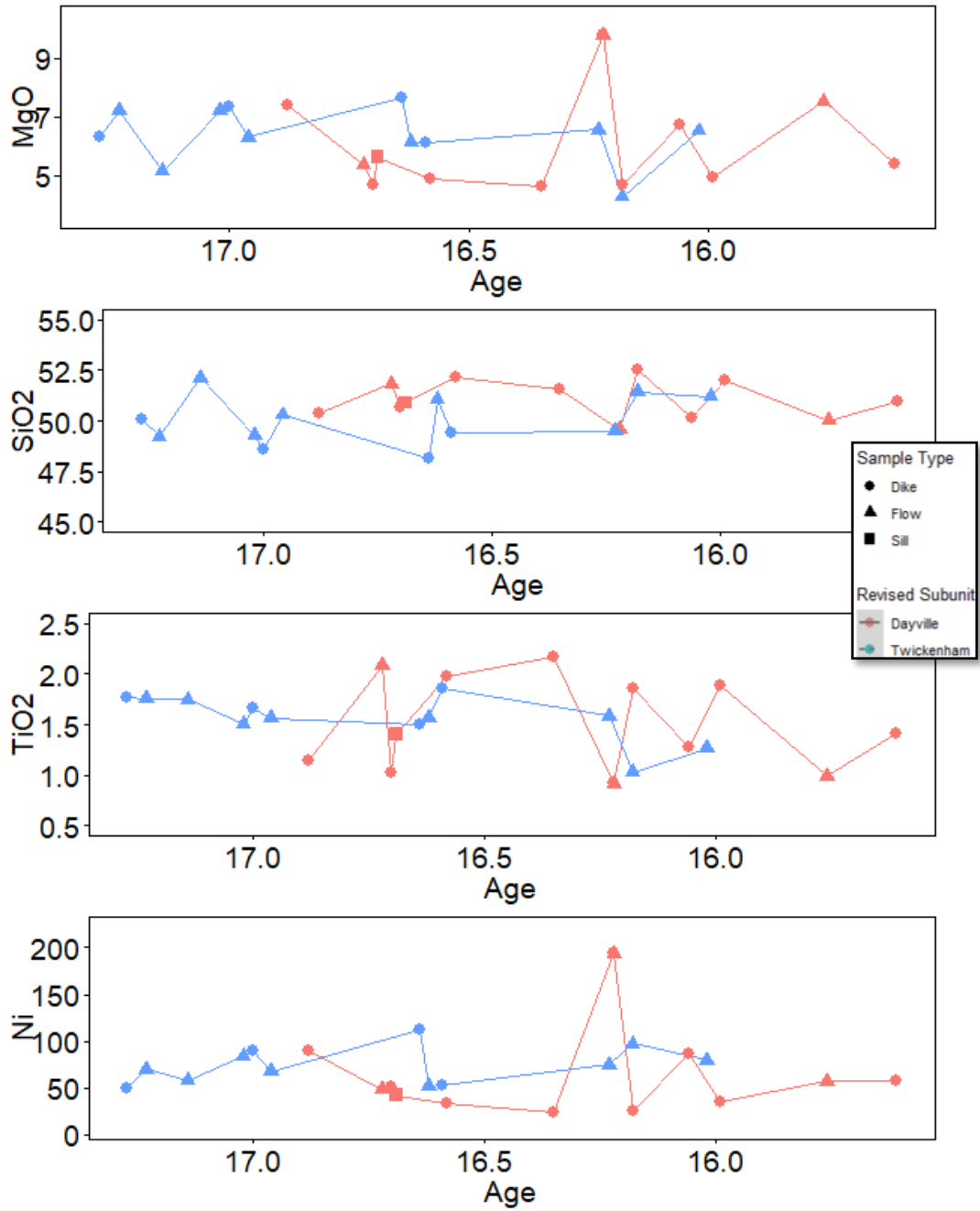


Figure 36: Element vs Age diagrams using revised subunit classification. Oxides are in weight percent, while trace elements are in ppm.

### ***Twickenham Trend***

The revised Twickenham subunit is the less incompatible element enriched overall trend of the Picture Gorge Basalt when comparing most trace elements against SiO<sub>2</sub> at SiO<sub>2</sub> values greater than 50 wt. %, as well as also being more depleted overall in high field strength elements (HFSE) when comparing HFSE against HFSE (i.e. Nb vs Zr, Figure 34). This subunit is also the older of the two on average, with dikes and flows dated up to 17.2 Ma (Cahoon et al., 2020; this study) with a lower age range ending at 16.02 Ma (Cahoon et al., 2020). Plotting various major and trace element concentrations against age suggests that recharge and fractionation and/or assimilation occurs at least three and up to five times throughout the lifecycle of the system, with samples having higher MgO and Ni and lower TiO<sub>2</sub> and SiO<sub>2</sub> occurring between three and five times (Figure 36). The oldest dated samples are comparatively more evolved than postulated recharging magmas. The Twickenham trend is subalkalic and is characterized by:

- TiO<sub>2</sub> and FeO\* content decreases with increasing SiO<sub>2</sub> content (Figure 11, 34)
- Higher HFSE concentration at lower SiO<sub>2</sub> (<50 wt. %), with a relatively flat trend with increasing SiO<sub>2</sub> when compared to Dayville, with Dayville having higher HFSE concentrations at SiO<sub>2</sub> >50 wt. %.
- Lower MgO concentration at lower SiO<sub>2</sub> (<50 wt. %) and higher MgO concentration at higher SiO<sub>2</sub> (>50 wt. %) when compared to Dayville.
- Total alkali content (Na<sub>2</sub>O + K<sub>2</sub>O) between 2-4, and a relatively flat trend when plotted against SiO<sub>2</sub>.

- Consistent FeO\* and CaO content between 10-12 wt %, regardless of SiO<sub>2</sub> content
- Lower Zr/Nb ratio and a steep declining Tb/Yb vs La/Yb ratio compared to the Dayville trend.
- Minor positive Eu anomaly (Figure 10).

Trends demonstrated by the Twickenham subunit were modeled for equilibrium crystallization using the MELTS 1.0.x Excel program (Gualda and Ghiorso 2015). The parent composition of High MgO sample CAH15-007 was used, and equilibrium crystallization models were run at 0.1 and 0.5 wt. % H<sub>2</sub>O. These equilibrium crystallization calculations assumed cooling from 1260-1000°C across constant pressure, with equilibrium crystallization calculated for 5, 10, 25, 50, 100, 200, 300, 400, 500, 600, 700, 800, 900, 1000, 1250, and 1500 MPa. These pressures correspond to depths of 0.175, 0.35, 0.875, 1.75, 3.5, 7, 10.5, 14.0, 17.5, 21.0, 24.5, 28.0, 31.5, 35, 43.7, and 52.5 km respectively. The mineral modes at each P-T combination were then used to calculate bulk partition coefficients for select trace elements, utilizing the partition coefficients in Table 6. These calculated bulk partition coefficients for select trace elements were then used to create models of fractional crystallization across the above selected temperatures and pressures. Fractionation models derived by MELTS calculations largely do not correspond to trends of the sample data across most major and trace element comparisons. Overall lack of fit to fractionation trends modelled in MELTS can be explained by:

- Parent composition uncertainty (i.e., mantle source heterogeneity, differences in partial melting of source mantle)
- Role of contamination is not accounted for by MELTS (including amount of contamination and differences in overall composition of various contaminants).

Cahoon (2020) largely eliminates many crustal contaminants through radiogenic isotope systematics and limits the degree of contamination with crustally derived material to be <10%. Extrapolating from the data from Soderberg and Wolff (2023) would seem to suggest that the Twickenham trend of this study would be most consistent with a more depleted, yet metasomatized MORB source component compared relative to the Dayville subunit. Furthermore, utilizing the bounds of partial melt vs residual garnet present during melting presented in Soderberg and Wolff (2023), the Tb/Yb vs La/Yb ratio (Figure 15) would indicate that there was between 3-5% partial melt with 1-2% of residual garnet present, which is distinctly different from the Dayville trend, discussed in the next section. Outliers of the Twickenham trend is still within the 1-2% residual garnet range, but at a partial melt percentage of approximately 2%. This would seem to indicate a distinctly different source mantle than the Dayville trend. Alternatively, recharge and mixing of a primitive, weakly metasomatized to depleted (MORB-like) source magma in the storage site(s) of the Twickenham trend could explain the various geochemical features discussed above, similar to what is seen in the Lower B Steens lavas (Moore et al. 2018). This latter explanation also conforms well to the geochemical trends through time (Figure 36).

### *Dayville Trend*

The revised Dayville subunit is subalkalic (Figure 35), with more evolved (greater SiO<sub>2</sub>) compositions trending towards weakly alkalic. Dayville rocks develop a more enriched overall trend when comparing various major, trace, and in particular HFSE concentrations, relative to the Twickenham subunit of the Picture Gorge Basalt for samples with SiO<sub>2</sub> values greater than 50 wt. %. This subunit is also slightly younger, with dikes and flows dated between 16.88 ± 0.06 Ma (Cahoon et al., 2020) to 15.61 ± 0.22 Ma (this study) in age. Also, elemental concentration vs age plots suggest that fractionation and/or assimilation dominate, with higher MgO and Ni occurring and lower TiO<sub>2</sub> and SiO<sub>2</sub> indicative of a recharge cycle occurring only three times in samples with geochronologic data (Figure 36). The most vigorous recharge event seems to occur at 16.18 Ma (Figure 36) with MgO and Ni concentrations increasing significantly (~2.5% and ~100 ppm, respectively). This unit is primarily characterized by:

- Higher HFSE concentration at higher SiO<sub>2</sub> (>50 wt. %), with a relatively steep trend with increasing SiO<sub>2</sub> when compared to Twickenham.
- Total alkali content (Na<sub>2</sub>O + K<sub>2</sub>O) ranges between 2-5, and a relatively steep positive trend when compared to SiO<sub>2</sub> as well as when compared to the Twickenham trend (Figure 35).
- Increasing TiO<sub>2</sub> and FeO\* content with increasing SiO<sub>2</sub> content (Figure 11) when compared to Twickenham trend.
- Higher Zr vs Nb and Y vs TiO<sub>2</sub> values when compared to the Twickenham trend

- Distinctly different Tb/Yb vs La/Yb trend when compared to the Twickenham trend.

Trends demonstrated by the samples of the Dayville subunit were modeled for fractionation using the parameters and methods discussed in the Twickenham Trend section of this paper. Models developed by MELTS largely do not correspond to the data of natural samples in terms of most major and trace element comparisons. Overall lack of a fit to fractionation trends modelled with MELTS can be explained a number of ways:

- Parent composition uncertainty (i.e., mantle source heterogeneity, differences in partial melting of source mantle)
- Role of contamination is not accounted for by MELTS (including amount of contamination and differences in overall composition of various contaminants).

As with the Twickenham trend, most crustal contaminants are largely excluded through isotope systematics and a max 10% limit is placed on those contaminants that would work (Cahoon, 2020). Extrapolating from Soderberg and Wolff (2023), a slightly greater portion of Innaha component to a more depleted MORB component could be inferred relative to the Twickenham trend. Lastly, fractionation and minor (<10% bulk content) contamination of a low degree partial melt of local country rock would explain trends seen in the Dayville subunit, especially relative increases in LILEs and HFSEs. This explanation also conforms well to the trends seen in geochronology vs geochemistry (Figure 36), as well as trends seen in the related Upper Steens flows and intrusives (Moore et al. 2018, Cahoon 2020). Furthermore, utilizing the bounds of partial melt vs

residual garnet present during melting presented in Soderberg and Wolff (2023), the Tb/Yb vs La/Yb ratio (Figure 15) would indicate that there were several stages of partial melting, with approximately 1-2% partial melting with approximately 2% residual garnet present, followed by partial melting between 2-10% with 0-2% residual garnet present, distinctly different from the Twickenham trend discussed previously. This would seem to imply a distinctly different source mantle than the Twickenham trend.

### **STEENS BASALT/STEEN DIKE SWARM**

#### *CLASSIFICATION AND GEOCHEMISTRY*

Flow subunit classification of the samples collected during this study had robust calculated accuracy and probability scores for each subunit. The subunits that samples were evaluated against are Lower A, Lower B, and Upper Steens. Subunit calculated accuracy was robust and are as follows with a calculated accuracy of 0.90 to 0.982 using a random forest machine learning model.

When compositional data are plotted on geochemical diagrams (i.e., Figures 16-21), dikes and other samples of this study largely conform to trends and clusters seen in data by previous studies of Moore et al. (2020) and Moore et al. (2018). Dike classifications of this study also conform well to geographic trends established for lavas by Camp et al. (2013) and others. Data of this study suggest dikes with Lower A and Lower B Steens compositions along the length of the study region in turn suggests possibly fissure eruptions along this distance, while dikes with Upper Steens compositions to be

concentrated around Steens Mountain in turn suggesting more centralized eruptions (Figure 26).

Chemical trends of Steens samples were modeled for fractional crystallization utilizing the methods and partition coefficients discussed in the Twickenham trend section of this paper, with the parent composition of Lower B Steens sample NMSB-15 used as the parent composition. Based on these model calculations, the following can be noted.

Fractionation lines of 0.5 wt. %  $H_2O$  largely conform to the observed data trends in plots of major element vs. major element and plots of HFSE vs HFSE (Figure 37). We can see the possible role of crustal contamination vs fractionation when we plot  $K_2O$  vs  $MgO$ , with elevated  $K_2O$  values relative to the fractionation curve and this could be indicative of contamination by partial crustal melts (Figure 18). When comparing  $MgO$  to  $Al_2O_3$ , Lower A and Lower B Steens samples primarily fall on the fractionation curves, but Upper Steens shows a sharp negative trend. This could be indicative of the formation of plagioclase  $\pm$  clinopyroxene cumulates within the crustal storage center, effectively lowering the overall  $Al_2O_3$  component of the eruptive products. This conforms to observed hand sample and field data as well, with Upper Steens lavas and dikes having lower plagioclase phenocryst content, as well as the observed composition of the implied Upper Steens age Streck LMI.

<b>ELEMENT</b>	<b>PLAGIOCLASE</b>	<b>OLIVINE</b>	<b>CLINOPYROXENE</b>	<b>ORTHOPYROXENE</b>
<b>Rb</b>	0.1	0.005	0.005	0.005
<b>Ta</b>	0	0.005	0.008	0.01
<b>Nb</b>	0	0.01	0.008	0.0013
<b>Th</b>	0.1	0.01	0.01	0.01
<b>Ba</b>	0.2	0.001	0.001	0.005
<b>La</b>	0.1	0.005	0.048	0.005
<b>Ce</b>	0.1	0.01	0.1	0.008
<b>Nd</b>	0	0.009	0.1	0.01
<b>Sm</b>	0	0.01	0.36	0.06
<b>Sr</b>	2	0	0.16	0.0012
<b>Eu</b>	0.2	0.01	0.39	0.07
<b>Tb</b>	0	0.01	0.4	0.16
<b>Y</b>	0	0.03	0.42	0.205
<b>Yb</b>	0	0.04	0.4	0.25
<b>Lu</b>	0	0.08	0.4	0
<b>Hf</b>	0.01	0.001	0.226	0.1
<b>Zr</b>	0.01	0.0047	0.28	0.032
<b>Zn</b>	0.06	0.77	0.2	0.9
<b>Sc</b>	0.014	0.4	3.94	1.3
<b>Cr</b>	0.12	1.4	10	2.6

Table 6: Partition coefficients of selected trace elements compiled from McKenzie and O’Nions (1991); Hart and Dunn (1993); Green (1994); Dunn and Sen (1994).

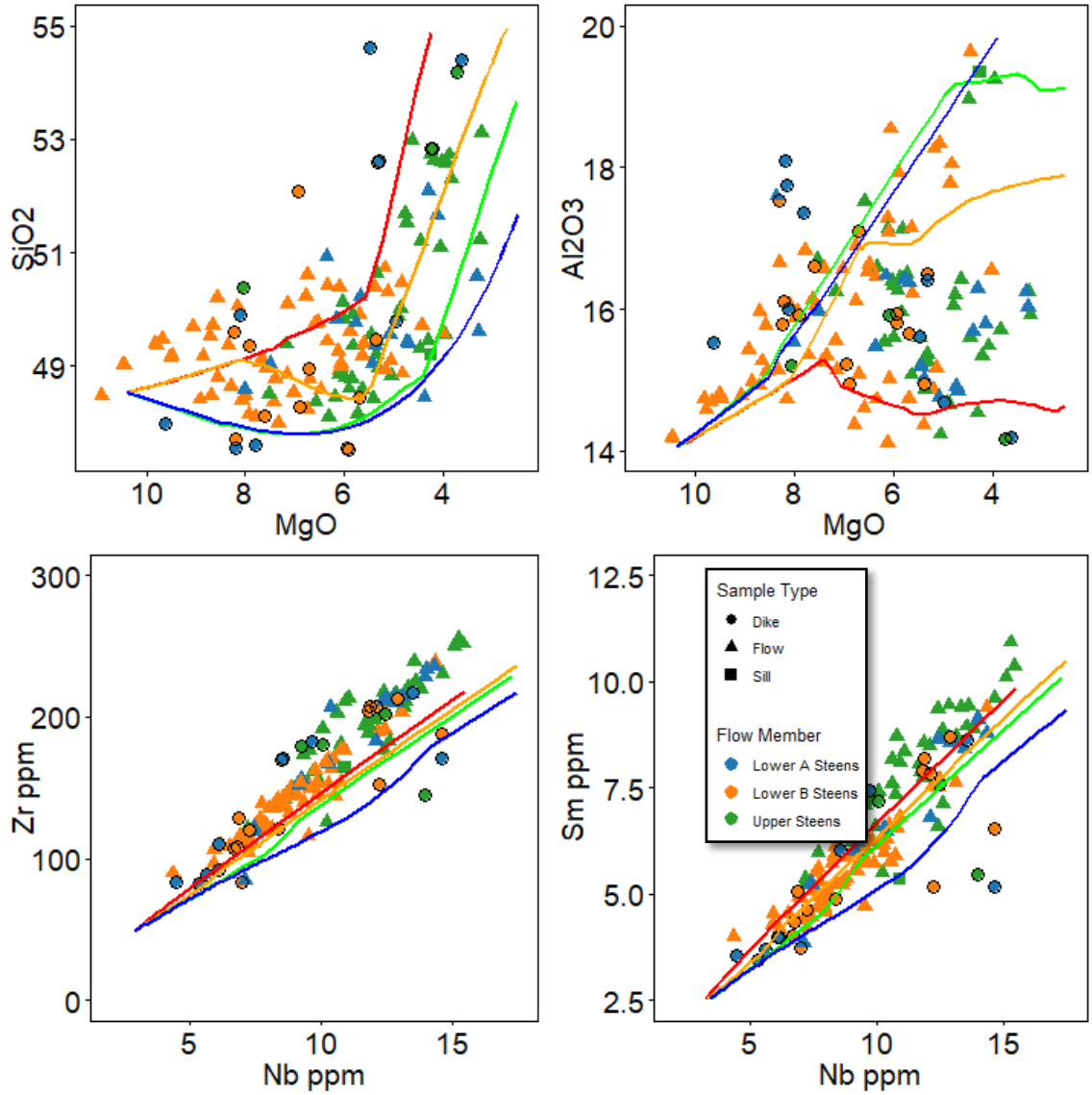


Figure 37: MELTS modelling of Steens Basalt. Red lines represent fractionation at 10 MPa; Orange lines represent fractionation at 250 MPa; Green lines represent fractionation at 500 MPa; Blue lines represent fractionation at 1000 MPa.

## **REGIONAL CONTEXT**

It has long been recognized that Picture Gorge Basalt type flows and intrusives are part of the Columbia River Basalt Group, however, it has also been noted by many workers that early lavas and intrusives of the Imnaha Basalt, specifically the lavas of the American Bar subunit and particularly the lavas of the basal American Bar subunit as found, for example, within the type locality of Dug Bar in northeastern Oregon (Hooper et al., 1984; Hooper 1988; Streck et al. 2023, and others), resemble lavas of the Picture Gorge Basalt. Other workers, however, note that Picture Gorge Basalt most closely resemble Steens type basalts as well as the nearby mafic lavas of the Strawberry Volcanics (Steiner and Streck, 2019; Cahoon et al., 2020, and others). As I propose in this study that PGB consists of two, rather than three, distinct geochemical subunits, namely the Twickenham and Dayville subunits, it is useful to discuss the Picture Gorge Basalt in relation to other Columbia River Basalt units.

### ***IMNAHA - PICTURE GORGE GEOCHEMICAL RELATIONSHIP***

As mentioned above, it has been noted by many workers that some Picture Gorge Basalt resemble early Imnaha lavas (Hooper et al. 1984; Hooper 1988; Wolff et al. 2008; Fredenberg 2022). This Imnaha main phase unit is subdivided into two geochemical units, the American Bar (AB) and the Rock Creek (RC) subunits, with the AB lavas showing the most similarities to PGB lavas. This is based on geochemical overlap between Imnaha Basalt subunits American Bar 1 & 2, located at Imnaha Basalt type locality of Dug Bar and other places in northeast Oregon, and the Picture Gorge Basalt.

However, these PGB and Innaha units are isotopically distinct (Wolff et al., 2008). Most notably, when plotted on most element covariant diagrams and element ratio plots, the Picture Gorge Basalt, Dayville subunit most consistently overlaps these units, specifically the South AB 1 or 2 units as designated by Streck et al. (2023), whereas there appears to be an overlap and/or trend continuation in many cases with the Twickenham subunit with the North AB 1 or 2 units as designated by Streck et al. (2023) (Figures 42, 43, 44, and 45). Overall, however, the Twickenham subunit of the Picture Gorge Basalt seems to be most geochemically similar to Innaha Basalt. While Dayville certainly overlaps Twickenham in nearly every covariant or ratio diagram, as well as follows similar trends, it also consistently shows significantly greater variability when compared to Twickenham. Twickenham, however, consistently forms a much tighter data cluster in most diagrams that often falls on the primitive end of the Innaha trend, and American Bar specifically, as can be seen in Figures 38 and 39. This would imply, that while commonalities between the three units certainly exist, Twickenham is the most “Innaha-like” of the two subunits. Conversely a Ba/Nb vs SiO<sub>2</sub> or Ba/Zr vs SiO<sub>2</sub> covariant diagram reliably discriminates between Picture Gorge Basalt and Innaha Basalt. PGB lavas and intrusives consistently have a greater ratio of LILEs to HFSEs and this shows as having a Ba/Nb ratio > 25 to 40 at SiO<sub>2</sub> content range of 48-53 wt. %, and Ba/Zr ratio >2 at similar SiO<sub>2</sub> compositional range. These comparisons can help differentiate PGB specifically from Innaha type deposits. These comparisons, specifically Ba/Nb and Ba/Zr vs. SiO<sub>2</sub> (Figure 38), as well as Tb/Yb vs La/Yb (Figure 39) would strongly indicate that, while similarities do exist between PGB and Innaha, that these two magmas are ultimately sourced from different mantle sources or mantle source ratios, with PGB

representing a more strongly metasomatized and depleted mantle relative to “Imnaha component” as defined by Wolff et al. (2008).

The lowest Ba/Nb values (20-45) are geographically located along what is presumably the lower-crustal cratonic decollement, as described by Cummings et al. (2000), as well as along the High Lava Plains-Snake River Plain fault lineament into the Picture Gorge region (Figure 40). Elevated Ba/Nb values (45-70) are located within the Picture Gorge region as well as throughout the Harney Basin. When all dikes are mapped by Ba/Nb ratio, we can see that the majority of Steens and Twickenham dikes largely fall within the low Ba/Nb category, with Twickenham dikes largely striking in parallel to the High Lava Plains-Snake River Plain fault lineament. Conversely, some Steens dikes and most Dayville dikes largely fall within the high Ba/Nb category, with Dayville dikes largely paralleling the central Harney Basin Fault lineament. This also geographically supports the assertion that, while there is overlap in composition between Steens, Imnaha, Twickenham, and Dayville, Twickenham is more “Imnaha-like” than “Steens-like”, with some exceptions, most notably with north and south AB1 and 2.

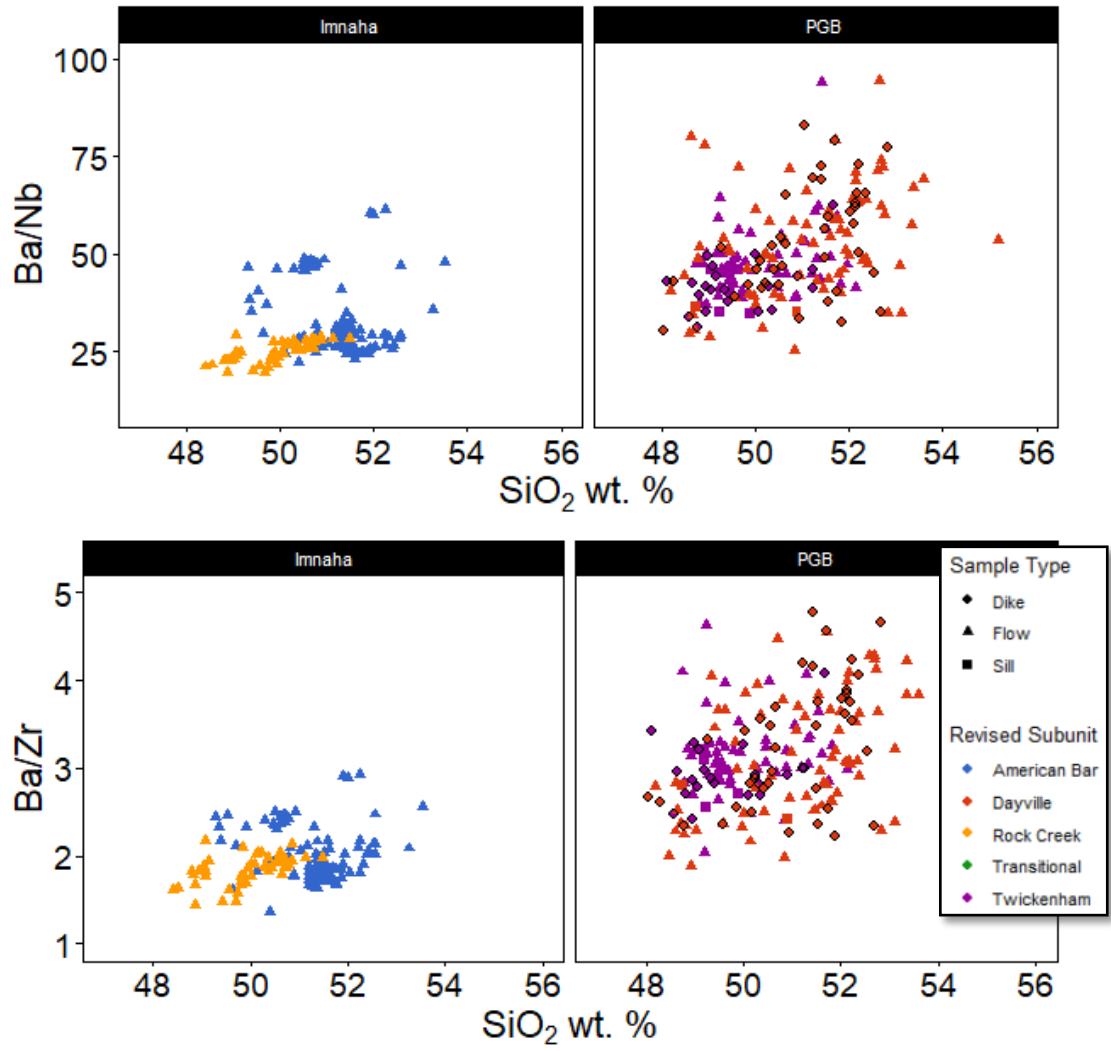


Figure 38: Ba/Nb and Ba/Zr vs SiO<sub>2</sub> comparison diagram of Picture Gorge and Imnaha Basalt.

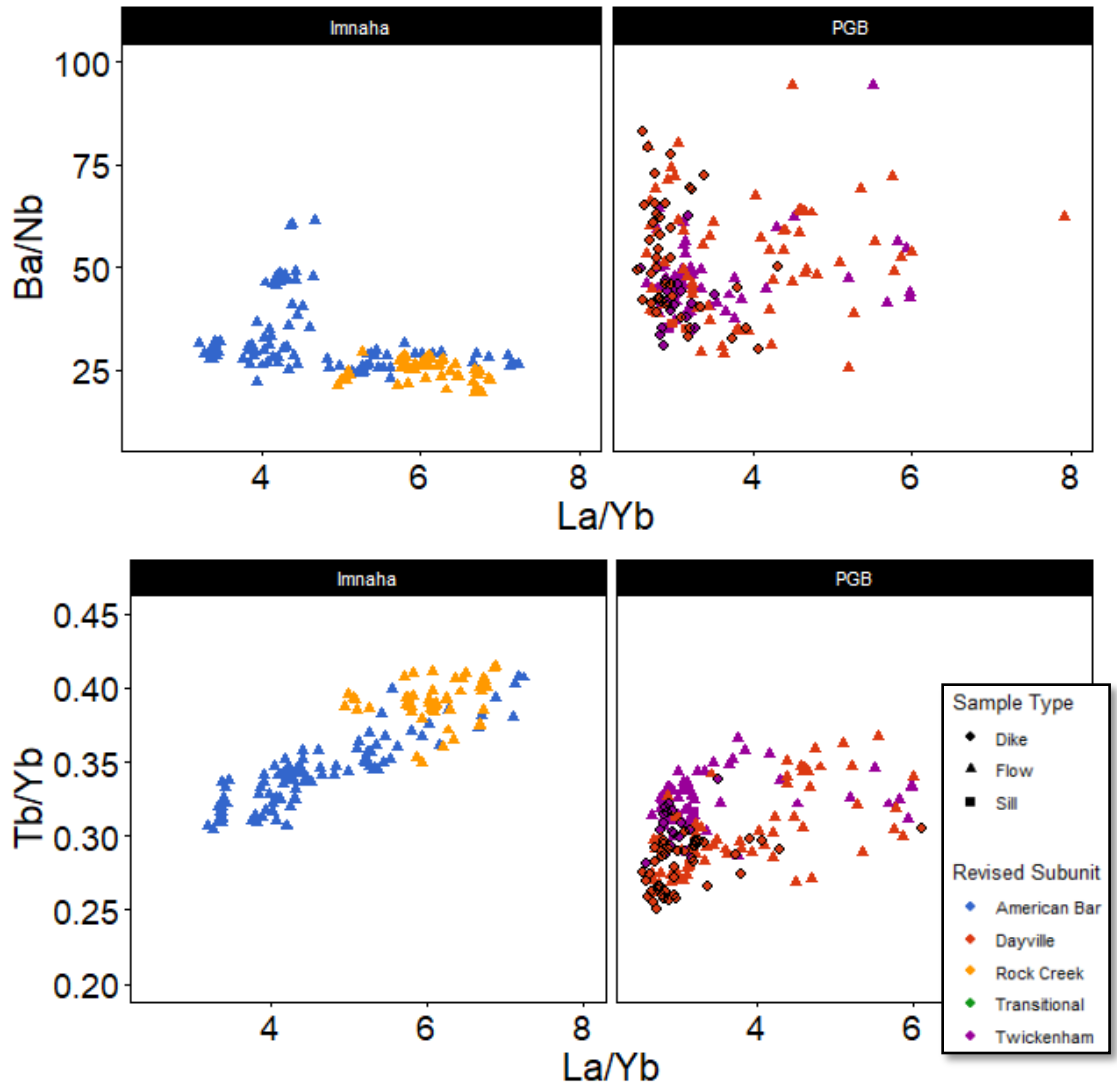


Figure 39: Ba/Zr vs SiO<sub>2</sub> comparison diagram of Picture Gorge and Imnaha Basalt.

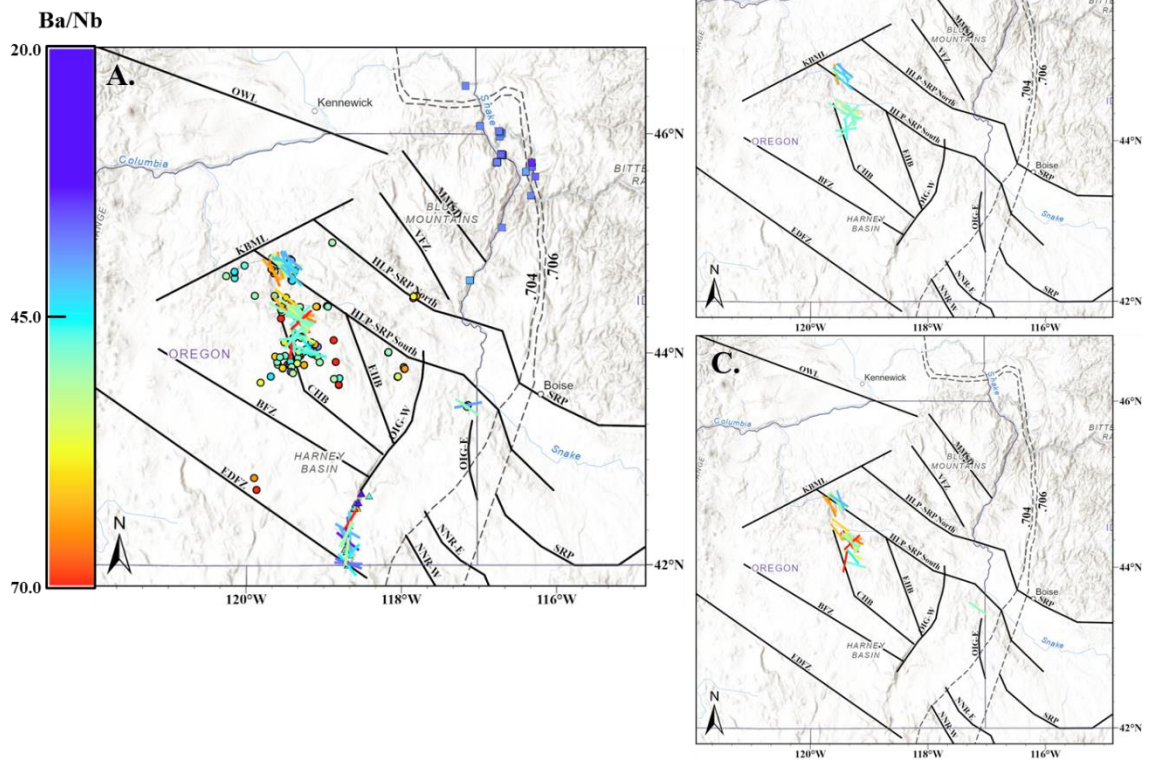


Figure 40: Geographic distribution of Ba/Nb ratios of primitive main phase Columbia River Basalt lavas and intrusives.

A. Geographic distribution of Ba/Nb ratios of primitive main phase Columbia River Basalt lavas (filled shapes) and dikes (colored lines). B. Geographic distribution of Twickenham dikes, colored using Ba/Nb scale of A. C. Geographic distribution of Dayville dikes, colored using Ba/Nb scale of A. Black lines in all maps represent normal fault lineaments. OWL: Olympic-Wallowa Lineament; VFZ: Vail Fault Zone; HLP-SRP: High Lava Plains-Snake River Plain; EHB: East Harney Basin; CHB: Central Harney Basin; BFZ: Brothers Fault Zone; EDFZ: Eugene-Denio Fault Zone; OIG-W and OIG-E: Oregon-Idaho Graben, west and east respectively; NNR-E and NNR-W: Northern Nevada Rift, east and west respectively.

### ***STEENS – PICTURE GORGE GEOCHEMICAL RELATIONSHIPS***

Some workers have noted that Picture Gorge Basalts isotopically resemble Steens type basalts, as well as the nearby mafic lavas of the Strawberry Volcanics (Wolff et al. 2008; Wolff and Ramos, 2013; Steiner and Streck, 2019; Cahoon et al., 2020). There is some geochemical overlap between lavas and intrusives primarily of the Dayville subunit of Picture Gorge and the lavas and intrusives of the Steens Basalt (e.g. Figures 41 and 42), primarily of Lower B Steens and some Upper Steens samples. In many of the major element vs major element and trace element vs trace element, the Dayville composition lavas and intrusives appear to loosely fall between Lower B Steens and Upper Steens lavas compositional values, with many primitive Dayville samples seemingly geochemically indistinguishable from Lower B Steens, and many evolved Dayville samples seemingly geochemically indistinguishable from Upper Steens lavas. This is compared to Twickenham, which largely either plots away from most Steens samples or shows differing trends. There are, however, areas where both Twickenham and Dayville compositions overlap Steens compositions (i.e. La/Nb vs SiO<sub>2</sub>, Figure 41). While Twickenham certainly overlaps Dayville in nearly every covariant or ratio diagram, as well as often follows similar trends, it also shows significantly less variability when compared to Dayville. This is in contrast to Steens Basalt samples, which show significant variability. This variability has been attributed to open system processes of fractionation, recharge, and crustal assimilation (Moore et al., 2018; Moore et al., 2020). This variation seen in Steens Basalt samples can also largely be seen in Dayville samples,

both intrusive and extrusive samples, and would seem to imply that, while similarities and geochemical overlap between Steens and the Picture Gorge Basalt subunits of Dayville and Twickenham certainly exists, it can be said that Dayville is, albeit weakly, the more “Steens-like” subunit of the Picture Gorge Basalt.

Conversely, a relatively reliable distinction between the Picture Gorge and Steens Basalt are seen on plots with Zr/Y vs SiO<sub>2</sub> or Ba/Nb vs La/Yb. Consistently PGB lavas and intrusives also show an enrichment in LILEs relative to HFSEs, and this can be seen in the Ba/Nb vs La/Yb plot of Figure 42 with a relatively narrow range of La/Yb values between 3-5, while the Ba/Nb values are all greater than 25. This contrasts with Steens Basalt samples, which show a range of La/Yb values between 4-10 and Ba/Nb ratios largely less than 50. We can also see greater enrichment Zr relative to Y in Steens Basalt samples compared to Picture Gorge Basalt samples, with PGB samples typically containing a Zr/Y ratio of 3-5 at SiO<sub>2</sub> compositions ranging between 47.5-55 wt. % a Zr/Y ratio of 4-6.5 across the same SiO<sub>2</sub> range for Steens lavas. These comparisons help to differentiate PGB specifically from Steens Basalt. Specifically, Zr/Y vs. SiO<sub>2</sub> and Ba/Nb vs. La/Yb (Figures 41, 42), as well as Th/Yb vs SiO<sub>2</sub> (Figure 42) strongly indicate that, while similarities do exist between PGB and Steens, that these two magmas are ultimately sourced from different mantle sources, with PGB representing a more metasomatized MORB-like mantle relative to Steens Basalt.

The highest Zr/Y values (4.0-6.5) are located along what is presumably the lower-crustal cratonic decollement (Cummings et al., 2000), as well as along the High Lava Plains-Snake River Plain fault lineament into the Picture Gorge region (Figure 43). Lower Zr/Y

values (1.5-4.0) are located within the Picture Gorge region as well as throughout the Harney Basin. When all dikes are mapped by Zr/Y ratio, we can see that the majority of Steens dikes and sampled Imnaha lavas largely fall within the high category (4.0-7.5), with Twickenham dikes having a Zr/Y ratio of near 4.0, and largely striking in parallel to the High Lava Plains-Snake River Plain fault lineament. Conversely, most Dayville dikes largely fall well within the low Zr/Y ratio category, with Dayville dikes largely paralleling the central Harney Basin Fault lineament.

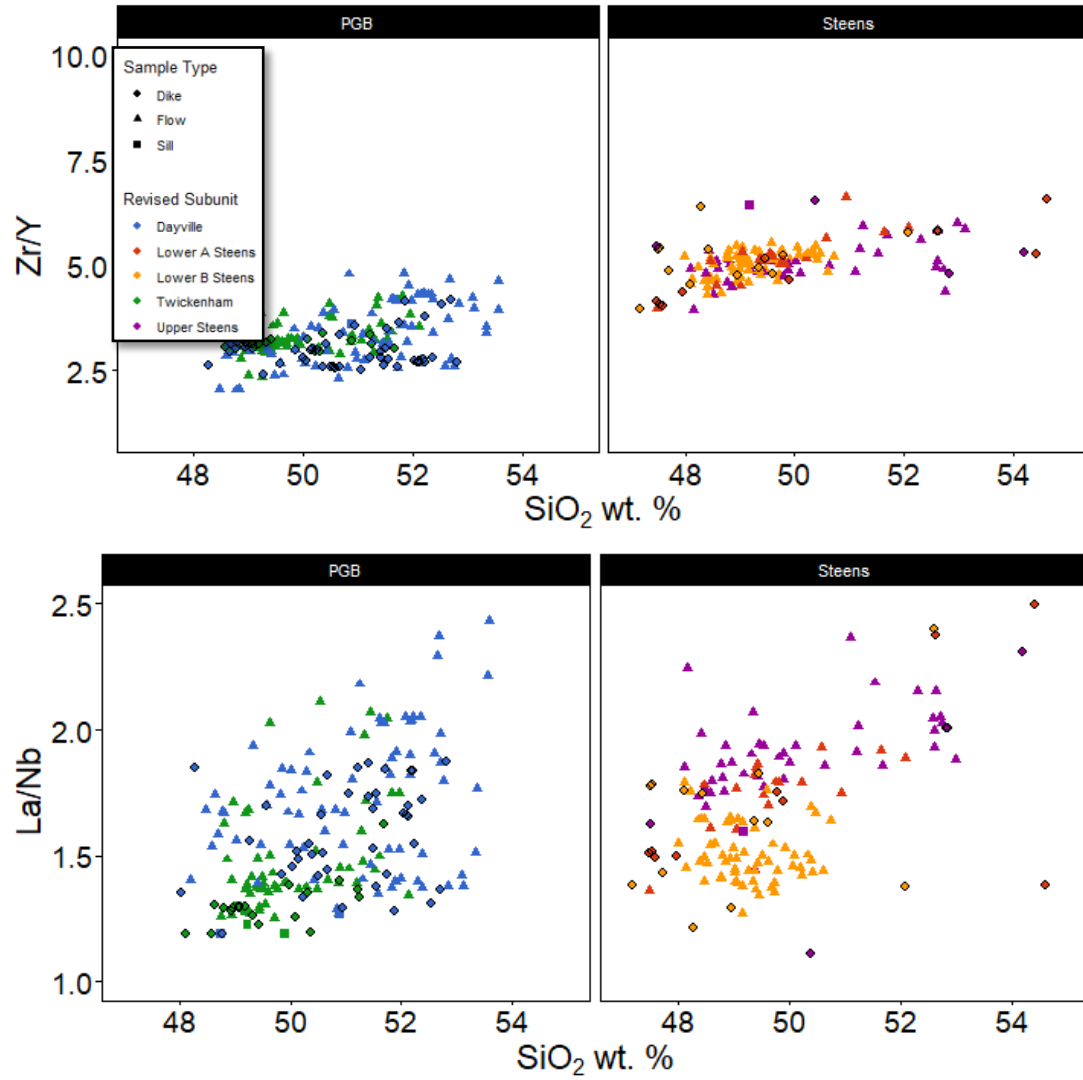


Figure 41: Zr/Y and La/Nb vs SiO<sub>2</sub> comparison diagram of Steens and Picture Gorge Basalt.

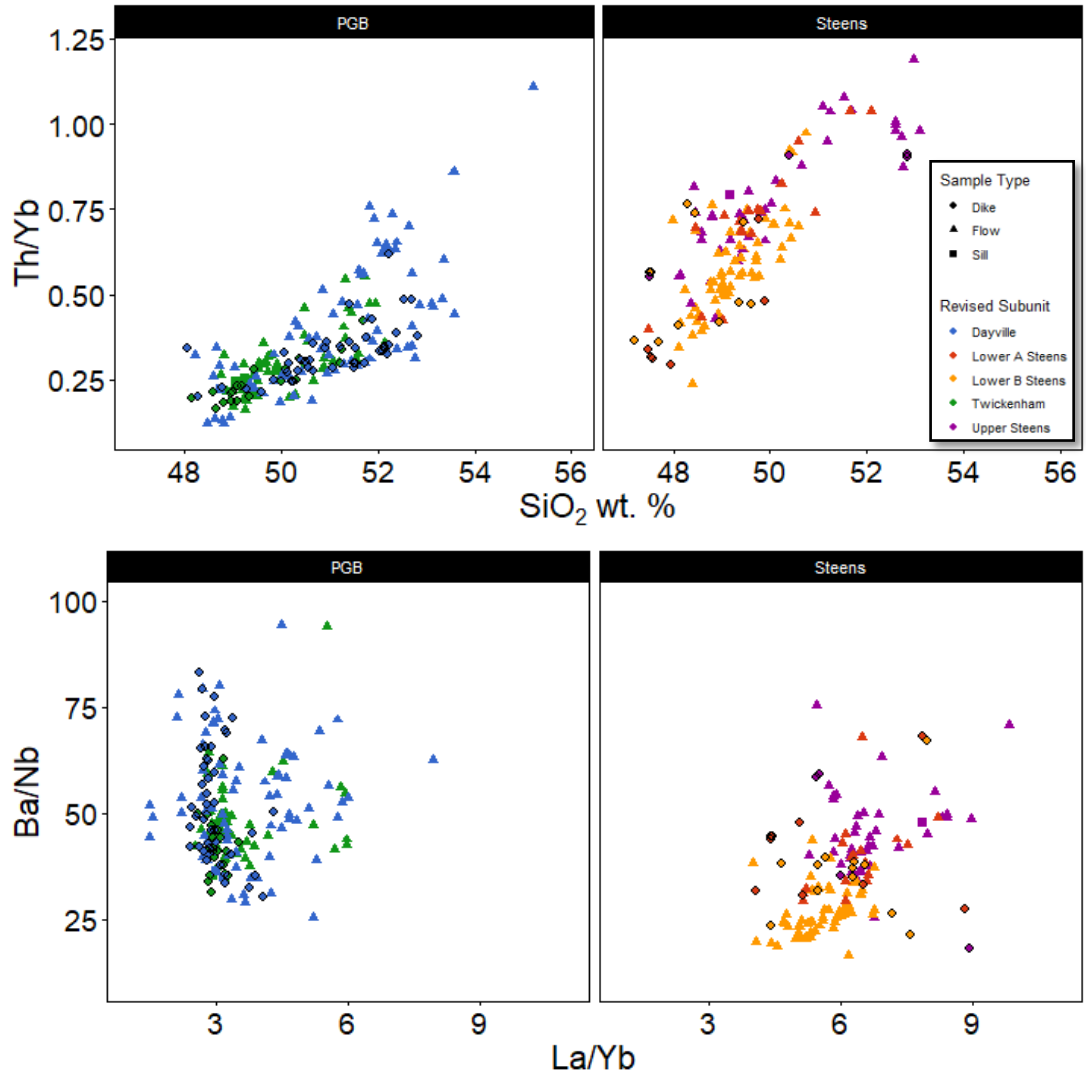


Figure 42: Th/Yb vs SiO<sub>2</sub> and Ba/Nb vs La/Yb comparison diagram of Steens and Picture Gorge Basalt.

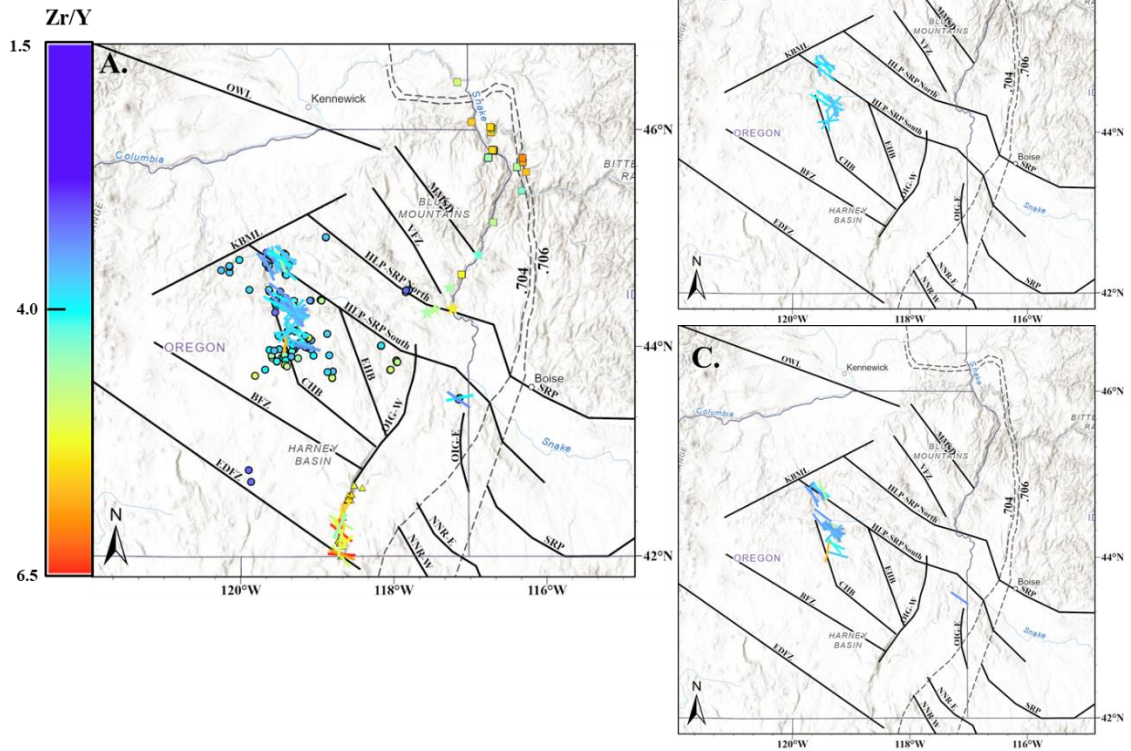


Figure 43: Geographic distribution of Zr/Y ratios of primitive main phase Columbia River Basalt lavas and intrusives.

A. Geographic distribution of Zr/Y ratios of primitive main phase Columbia River Basalt lavas (filled shapes) and dikes (colored lines). B. Geographic distribution of Twickenham dikes, colored using Zr/Y scale of A. C. Geographic distribution of Dayville dikes, colored using Zr/Y scale of A. Black lines in all maps represent normal fault lineaments. OWL: Olympic-Wallowa Lineament; VFZ: Vail Fault Zone; HLP-SRP: High Lava Plains-Snake River Plain; EHB: East Harney Basin; CHB: Central Harney Basin; BFZ: Brothers Fault Zone; EDFZ: Eugene-Denio Fault Zone; OIG-W and OIG-E: Oregon-Idaho Graben, west and east respectively; NNR-E and NNR-W: Northern Nevada Rift, east and west respectively.

## **MAGMA STORAGE AND TRANSPORT**

When comparing the two Picture Gorge Basalt subunits, Innaha, and Steens Basalt, we can see on a number of different discriminant diagrams that all four of these magmas ultimately come from distinctly different mantle sources from one another (e.g. Figures 38, 39, 41, 42) (Streck et al., 2023b). This implies that, for this to occur, there must be at least four (or more) main magmatic reservoirs that supplied these units. Using this knowledge, as well as incorporating field observations, geophysical data in the form of isostatic gravity and aeromagnetic data, mineral deposit database, and known structures (i.e. faults) within these regions, we can begin to ascertain more specific locations of mid- to upper- crustal storage locations for Columbia River Basalt Group magmas. We can surmise the following conclusions from field and geochemical data, as well as limitations provided by country rock conditions and local structure and use this to determine locations of storage more definitively:

- Twickenham, Dayville, Steens, and Innaha represents multiple storage locations sourced from distinct mantle compositions, as discussed in the prior sections.
- Work done by Wolff et al. (2008) and others genetically link Innaha and Grande Ronde chemical types, with Grande Ronde being the product of fractionated and crustally contaminated Innaha magmas. This would imply that, while there is significant evolution between the two, Innaha and Grande Ronde share the same storage system.
- Work done by Breuseke et al. (2007) as well as Camp (2003) and others have linked some lavas of Malheur Gorge, the Santa Rosa-Calico Volcanic Field, and

the northern Nevada Rift as having similar to, or identical, geochemical, and petrographic characteristics as Steens lavas and intrusives, and thus implies that they share the same storage system.

- Dikes strongly parallel normal fault lineaments in all regions, indicating that normal faults were likely used as transport and/or storage in the form of keel dikes and lopoliths for Columbia River Basalt Group magmas.
  - In the case of the Steens Basalts, these dikes follow the Western Nevada Shear Zone, which forms the boundary between the Olds Ferry Terrane and Black Rock-Jackson Terrane, as well as the prominent normal faults related to the Oregon Idaho Graben.
  - In the case of the Twickenham dikes, these largely seem to follow normal faulting of the Snake River-High Lava Plains fault trend, with some of the westernmost Twickenham dikes oriented along strike with the central Harney Basin fault lineament.
  - In the case of the Dayville dikes, these largely seem to follow the central Harney Basin fault lineament.
  - In the case of the Chief Joseph Dike Swarm (Imnaha and Grande Ronde Basalts), these dikes largely seem to parallel the north-northwest striking faults parallel to the Vail Fault Zone (Figures 7,8) (Morriss et al. 2020).
- Coeval felsic eruptions, and their felsic magma chambers act as buoyancy filters to ascending basaltic magma (Streck et al., 2015; Coble and Mahood, 2016).

- Thus, the outer edge of felsic eruptions or volcanic fields should approximately correspond to the extent of lower- to mid- crustal storage, with some exceptions.
- Conversely, the inner margin of co-eval felsic eruptions should approximately correspond to the extent of mid- to upper- crustal storage.
- Long term magmatic storage should create a robust hydrothermal system with base and precious metal deposition in the form of sulfide minerals within the upper crust.
  - This can be directly observed with the Streck LMI, as abundant crystalline quartz and base metal sulfides can be found in direct relation to the intrusive body.
  - This can also be seen with associations between the northern Nevada Rift intrusions and the bonanza style epithermal gold deposits that exist paralleling these intrusive deposits (Zoback et al. 1994; Ponce and Glen 2002, Kamenov et al., 2007). This would also seem to indicate that long term crustal storage of Columbia River Basalt magmas should generate a bonanza style epithermal deposit as a typical indicator of crustal storage within mafic terrane rock.
  - Exo-skarn style mineralization can be seen throughout the Wallowa region and can be used as a possible indicator of storage through interaction of hydrothermal and magmatic fluids and overlying carbonate deposits.

- Field observations of mineralization were supplemented by the Mineral Information Layer for Oregon, release 3 (MILO-3) (McClaughry et al. 2021), filtered for instances of Cu or Au mineralization, and further filtered to remove mineralization related to plutonic or metamorphic activity (i.e. tungsten or tin) that also contains Cu or Au instances.
- The Monument Dike Swarm shows minimal evidence of extended long-term local storage, with sills within the John Day Basin showing alteration consistent with that of a magmatic intrusion (i.e. baked contacts, enrichment in Fe hydroxides and clay minerals) but little indicators of long-term mineralization when compared to in situ mineralization present in the upper crustal Streck LMI. This is also reflected in the Monument Dike Swarm dikes as well, with most dikes showing minimal alteration halos, even in dikes of large size (> 5m). This would seem to indicate that little long-term storage has occurred within the immediate vicinity of this dike swarm and is instead reflective of some amount of distal transport. This also implies that sills of both Dayville and Twickenham geochemistry that are exposed in the John Day Basin are likely representative of magma transport or relatively quick cooling intrusive bodies and are not representative of long-term storage. This does not preclude possible mid- or lower- crustal storage, merely upper crustal storage.
  - The exception to this lack of apparent sulfide mineralization is possible epithermal deposits containing Cu and Au, on the southern side of Strawberry Mountain, located near the town of John Day, Oregon.

- Cu-Ni, Cr, and PGE deposits to the north of Strawberry Mountain, while commonly associated with layered intrusions, and hence magmatic storage, are most likely related to podiform chromite deposits typical of dunite pods within in ophiolites, which is representative of the composition of the Canyon Mountain Ophiolite that is within the field area (Mosier et al., 2012; McClaughrey et al. 2021).
- Positive aeromagnetic and isostatic gravity anomalies should exist within the storage system.
  - Cumulate material in the form of ultramafic cumulates are moderately to significantly denser than the surrounding crust, as are any large deposits of precipitated Fe-Ni or Cu-Ni sulfides and should show as a positive isostatic gravity anomaly.
  - Precipitation of oxides, such as the Fe-Ti oxide present in the anorthosite layer of the Streck LMI, should present as significant positive aeromagnetic anomalies.

Limitations of the aeromagnetic and isostatic gravity anomalies as seen today attempts to distinguish between aeromagnetic and gravity anomalies created by CRBG storage sites and those due to pre- and post- CRBG volcanism (i.e. High Lava Plains basaltic volcanism and Mid-Tertiary Ignimbrite volcanism), as well as anomalies that are related to accreted oceanic basaltic terranes (i.e. Baker Terrane and Canyon Mountain Ophiolite, Olds Ferry Terrane, etc.). By using the considerations listed above and keeping in mind

the mentioned limits, I postulate mid- to upper- crustal storage locations for main phase CRBG magmas, as shown in Figure 44.

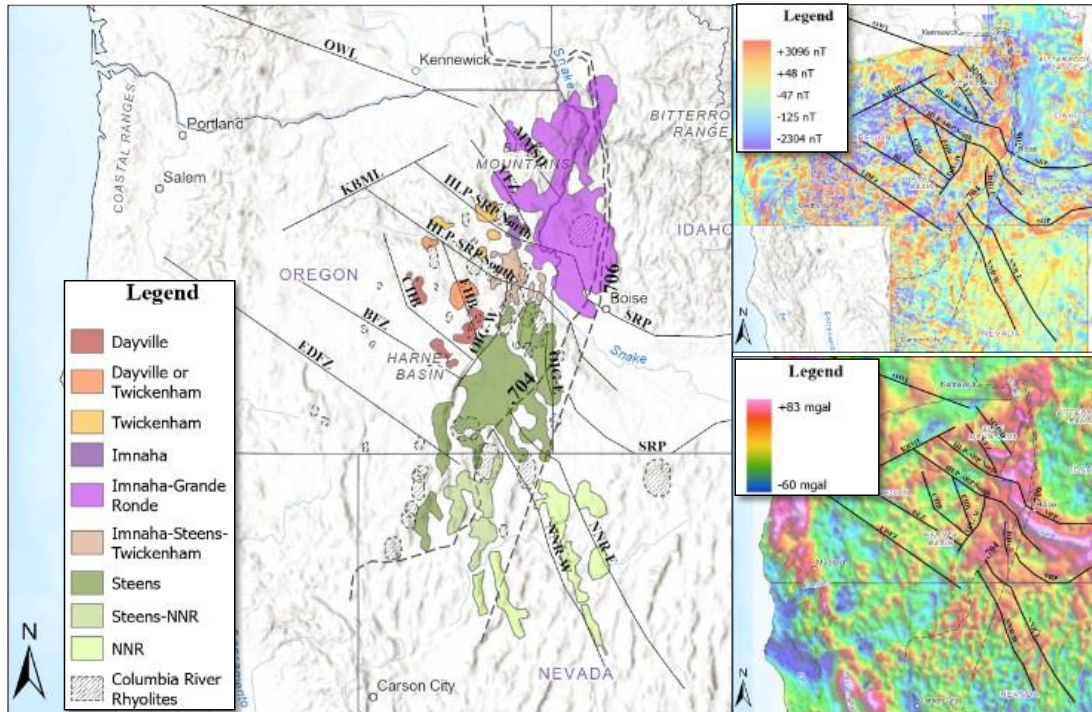


Figure 44: Regional mid- and upper- crustal storage locations for CRBG magmas.

A. Regional mid- and upper- crustal storage locations for CRBG magmas, overlain with fault lineaments and felsic eruption sites. EDFZ: Eugene-Denio Fault Zone; BFZ: Brothers Fault Zone; OIG: Oregon-Idaho Graben; OWL: Olympic-Wallowa Lineament; SRP: Snake River Plain; NNR: northern Nevada rift; KBML: Klamath-Blue Mountains Lineament (gravity); HLP-SRP: High Lava Plains-Snake River Plain; CHB & EHB: Central and eastern Harney Basin normal fault lineaments; MMSD: Fault lineament paralleling VFZ and other mid-Miocene stress direction normal fault lineaments; Black dashed line indicates .704 (westernmost) and .706 (easternmost)  $^{87/89}\text{Sr}$  isopleths; Dashed outline hatched polygons: Columbia River Rhyolites (Streck et al., 2023b). B. Aeromagnetic map of Oregon, Idaho, and Washington, overlain with fault lineaments for context. Data derived from Bankey et al. (2002). All fault lineaments correspond to A. C. Regional isostatic gravity anomaly map, overlain with fault lineaments for context. Data derived from Phillips et al. (1993).

Evidence suggests that the crustal storage of Imnaha-Grand Ronde Basalts terminates along the southern edge of the Snake River Plain. Storage and likely storage and transport of magmas extends north along the cratonic boundary as well as to the northwest (Morris et al. 2020), following normal fault lineaments that parallel the Vail Fault Zone (Figure 4) and other major pre-Miocene fault lineaments related to the rollback of the Farallon Plate (Zoback et al.,1994; Humphreys et al.,2006).

This can be compared with the magmatic storage and transport routes for the Steens, Warner, and northern Nevada Rift (NNR) basalts and intrusives, which primarily occurs as arcuate bands parallel to the middle-Miocene stress direction as determined by Zoback et al. (1994), and others, with the exception of storage occurring within the Oregon-Idaho Graben (OIG) (Figure 4). Evidence suggests that the joint Steens, Warner, and NNR crustal storage locations terminate at the northern end of the OIG and extends south into central Nevada. The OIG storage location of the Steens, Warner, and NNR magmas likely contained the bulk of the long-term magma storage, as evidenced by the size, longevity of the related felsic volcanism (Streck et al. 2023a) (Figure 5), as well as large amount of epithermal mineral deposits in the region.

Picture Gorge Basalt magmas appear to have been primarily stored within two general regions: the High Lava Plain-Snake River Plain (HLP-SRP) region, and along this axis; as well as along the central Harney Basin (CHB) and eastern Harney Basin (EHB) fault lineaments. As evidenced by geochemical relationships (Figures 47 and 53) and field evidence (Figures 24 and 27), it would appear that Twickenham magmas were stored primarily along the HLP-SRP axis, with possible overlap with Dayville magmas within

the Strawberry Mountains region. Conversely, Dayville magmatic storage likely occurred within the Harney Basin, with storage and transport accommodated primarily along and within the CHB and EHB normal fault lineaments.

## CONCLUSION

In this study we have reported on the geochemistry and geochronology of the dikes and sills of the Monument Dike Swarm (MDS), as well as their relationship to the subaerial lava flows of the Picture Gorge Basalt (PGB), with implications for crustal storage of these magmas. We have increased sampled intrusives and added compositional data of 48 dikes and several small sills of this study, as well as 10 new  $^{40}\text{Ar}/^{39}\text{Ar}$  ages of select MDS dikes to prior data. With new and previously published age data, we show that the age range of the Picture Gorge Basalt and its related intrusives span from  $17.27 \pm 0.05$  Ma to  $15.61 \pm 0.22$  Ma. Based on new compositional data, I propose to subdivide PGB into two compositional subunits, Twickenham and Dayville, based on differing trends observed in plots of, e.g., Zr vs Nb,  $\text{TiO}_2$  vs  $\text{SiO}_2$ , Y vs  $\text{TiO}_2$  and MgO vs  $\text{SiO}_2$ . This simplification resolves issues with ages and distribution of these geochemical subunits in the work of Cahoon et al. 2020, this study, and the stratigraphy established in the type locality by Bailey, 1989. Relevant to this new geochemical classification, compositional data indicates that the Twickenham and Dayville geochemical subunits are sourced from differing mantle compositions (e.g. Tb/Yb vs La/Yb). Picture Gorge Basalt dikes and other intrusives have compositions that largely match lava flows.

This study also adds data of 26 newly sampled Steens Basalt dikes to the existing dike data of Moore et al. 2018, with data evaluated to determine their compositional relationships to subaerial Steens Basalt flows, in part searching for evidence of crustal magma storage locations. Relevant to this, we also report for the first time the discovery of a compositionally zoned, mafic intrusive body related to the Steens Basalt, informally

referred to as the Streck Layered Mafic Intrusion by this author. This intrusive body is currently estimated to have a minimum extent of 125 km<sup>2</sup>, with lithologies including anorthosite, leucogabbro, and troctolite, and compositionally spans the range of picritic basalt, hawaiite, and mugearite. Steens Basalt dikes and others intrusives have compositions that match lava flows, except in cases where crystal accumulation is likely to dictate bulk compositions.

This new intrusive data acquired from both the Picture Gorge and Steens Basalt was integrated with available geochemical, geophysical, and geographic data for the region, and was used to determine a model of Columbia River Basalt Group mid- and upper-crustal magma storage locations.

## WORKS CITED

- Adam, J., & Green, T. (2006). Trace element partitioning between mica- and amphibole-bearing garnet lherzolite and hydrous basanitic melt: 1. Experimental results and the investigation of controls on partitioning behaviour. *Contributions to Mineralogy and Petrology*, 152(1), 1–17. <https://doi.org/10.1007/s00410-006-0085-4>
- Arndt, N. T., Leshner, C. M., & Czamanske, G. K. (2005). Mantle-Derived Magmas and Magmatic Ni-Cu-(PGE) Deposits. In J. W. Hedenquist, J. F. H. Thompson, R. J. Goldfarb, & J. P. Richards, *One Hundredth Anniversary Volume*. Society of Economic Geologists. <https://doi.org/10.5382/AV100.02>
- Bailey, M. M. (1989). Revisions to stratigraphic nomenclature of the Picture Gorge Basalt Subgroup, Columbia River Basalt Group. In *Geological Society of America Special Papers* (Vol. 239, pp. 67–84). Geological Society of America. <https://doi.org/10.1130/SPE239-p67>
- Bankey, V., Cuevas, A., Daniels, D., Finn, C. A., Hernandez, I., Hill, P., Kucks, R., Miles, W., Pilkington, M., Roberts, C., Roest, W., Rystrom, V., Shearer, S., Snyder, S., Sweeney, R. E., Velez, J., Phillips, J. D., & Ravat, D. K. A. (2002). *Airborne measurement of the earth's magnetic field over all of North America provides gridded data describing the magnetic anomaly caused by variations in earth materials and structure*. (Open-File Report 2002–414; pp. 45-1-47–4). U.S. Geological Survey. [doi.org/10.3033/ofr02414](https://doi.org/10.3033/ofr02414)
- Bea, F. (1996). Behavior of Trace Elements During Magma Genesis and Evolution. *Geology*, Volume II, 4.

- Benson, T. R., Mahood, G. A., & Grove, M. (2017). Geology and  $^{40}\text{Ar}/^{39}\text{Ar}$  geochronology of the middle Miocene McDermitt volcanic field, Oregon and Nevada: Silicic volcanism associated with propagating flood basalt dikes at initiation of the Yellowstone hotspot. *GSA Bulletin*, *129*(9–10), 1027–1051. <https://doi.org/10.1130/B31642.1>
- Best, M. G., Christiansen, E. H., de Silva, S., & Lipman, P. W. (2016). Slab-rollback ignimbrite flareups in the southern Great Basin and other Cenozoic American arcs: A distinct style of arc volcanism. *Geosphere*, *12*(4), 1097–1135. <https://doi.org/10.1130/GES01285.1>
- Biasi, J., & Karlstrom, L. (2021). Timescales of magma transport in the Columbia River flood basalts, determined by paleomagnetic data. *Earth and Planetary Science Letters*, *576*, 117169. <https://doi.org/10.1016/j.epsl.2021.117169>
- Bindeman, I. N., Greber, N. D., Melnik, O. E., Artyomova, A. S., Utkin, I. S., Karlstrom, L., & Colón, D. P. (2020). Pervasive Hydrothermal Events Associated with Large Igneous Provinces Documented by the Columbia River Basaltic Province. *Scientific Reports*, *10*(1), 10206. <https://doi.org/10.1038/s41598-020-67226-9>
- Brandon, A. D., Hooper, P. R., Goles, G. G., & Lambert, R. S. (1993). Evaluating crustal contamination in continental basalts: The isotopic composition of the Picture Gorge Basalt of the Columbia River. *Contributions to Mineralogy and Petrology*, *114*(4), 452–464. <https://doi.org/10.1007/bf00321750>
- Brooks, H. C. (1994). Geology of the Blue Mountains region of Oregon, Idaho, and Washington: Stratigraphy, physiography, and mineral resources of the Blue Mountains region. In *Geology of the Blue Mountains region of Oregon, Idaho, and*

- Washington: Stratigraphy, physiography, and mineral resources of the Blue Mountains region* (USGS Numbered Series 1439; Professional Paper, Vol. 1439). U.S. Geological Survey. <https://doi.org/10.3133/pp1439>
- Brueseke, M. E., Hart, W. K., & Heizler, M. T. (2008). Diverse mid-Miocene silicic volcanism associated with the Yellowstone–Newberry thermal anomaly. *Bulletin of Volcanology*, 70(3), 343–360. <https://doi.org/10.1007/s00445-007-0142-5>
- Brueseke, M. E., Heizler, M. T., Hart, W. K., & Mertzman, S. A. (2007). Distribution and geochronology of Oregon Plateau (U.S.A.) flood basalt volcanism: The Steens Basalt revisited. *Journal of Volcanology and Geothermal Research*, 161(3), 187–214. <https://doi.org/10.1016/j.jvolgeores.2006.12.004>
- Cahoon, E. (2020). Distribution, Geochronology, and Petrogenesis of the Picture Gorge Basalt with Special Focus on Petrological Relationships to the Main Columbia River Basalt Group. *Dissertations and Theses*. <https://doi.org/10.15760/etd.7481>
- Cahoon, E. B., Barry, P. H., & Koppers, A. A. P. (2015). Geochronology and geochemistry of basalts from the Austral Islands, French Polynesia: Implications for Pacific plate evolution. *Geochemistry, Geophysics, Geosystems*, 16(3), 831–847. <https://doi.org/10.1002/2014GC005649>
- Cahoon, E. B., Streck, M. J., & Koppers, A. A. P. (2023). Picture Gorge Basalt: Internal stratigraphy, eruptive patterns, and its importance for understanding Columbia River Basalt Group magmatism. *Geosphere*, 19(2), 406–430. <https://doi.org/10.1130/GES02508.1>

- Cahoon, E. B., Streck, M. J., Koppers, A. A. P., & Miggins, D. P. (2020). Reshuffling the Columbia River Basalt chronology—Picture Gorge Basalt, the earliest- and longest-erupting formation. *Geology*, 48(4), 348–352. <https://doi.org/10.1130/G47122.1>
- Camp, V. E. (1995). Mid-Miocene propagation of the Yellowstone mantle plume head beneath the Columbia River basalt source region. *Geology*, 23(5), 435–438. [https://doi.org/10.1130/0091-7613\(1995\)023<0435:MMPOTY>2.3.CO;2](https://doi.org/10.1130/0091-7613(1995)023<0435:MMPOTY>2.3.CO;2)
- Camp, V. E. (2015). *Radiating Volcanic Migrations: An example from the Pacific Northwest, U.S.A.* [https://www.academia.edu/95176187/www\\_MantlePlumes\\_org\\_MantlePlumes\\_org\\_Radiating\\_Volcanic\\_Migrations\\_An\\_example\\_from\\_the\\_Pacific\\_Northwest\\_U\\_S\\_A](https://www.academia.edu/95176187/www_MantlePlumes_org_MantlePlumes_org_Radiating_Volcanic_Migrations_An_example_from_the_Pacific_Northwest_U_S_A)
- Camp, V. E., & Hanan, B. B. (2008). A plume-triggered delamination origin for the Columbia River Basalt Group. *Geosphere*, 4(3), 480.
- Camp, V. E., & Ross, M. E. (2004). Mantle dynamics and genesis of mafic magmatism in the intermontane Pacific Northwest. *Journal of Geophysical Research: Solid Earth*, 109(B8). <https://doi.org/10.1029/2003JB002838>
- Camp, V. E., Ross, M. E., Duncan, R. A., Jarboe, N. A., Coe, R. S., Hanan, B. B., & Johnson, J. A. (2013). The Steens Basalt: Earliest lavas of the Columbia River Basalt Group. In S. P. Reidel, V. E. Camp, M. E. Ross, J. A. Wolff, B. S. Martin, T. L. Tolan, & R. E. Wells, *The Columbia River Flood Basalt Province*. Geological Society of America. [https://doi.org/10.1130/2013.2497\(04\)](https://doi.org/10.1130/2013.2497(04))
- Camp, V. E., Ross, M. E., & Hanson, W. E. (2003). Genesis of flood basalts and Basin and Range volcanic rocks from Steens Mountain to the Malheur River Gorge,

- Oregon. *GSA Bulletin*, 115(1), 105–128. [https://doi.org/10.1130/0016-7606\(2003\)115<0105:GOFBAB>2.0.CO;2](https://doi.org/10.1130/0016-7606(2003)115<0105:GOFBAB>2.0.CO;2)
- Camp, V., Reidel, S., Ross, M., Brown, R., & Self, S. (2017). *Field-trip guide to the vents, dikes, stratigraphy and structure of the Columbia River Basalt Group, eastern Oregon and southeastern Washington*. <https://doi.org/10.3133/sir20175022N>
- Camp, V., & Wells, R. (2021). The Case for a Long-Lived and Robust Yellowstone Hotspot. *GSA Today*, 31(1), 4–10. <https://doi.org/10.1130/GSATG477A.1>
- Cities and Towns of the United States, 2014 in EarthWorks*. (2014). <https://earthworks.stanford.edu/catalog/stanford-bx729wr3020>
- Coble, M. A., & Mahood, G. A. (2016). Geology of the High Rock caldera complex, northwest Nevada, and implications for intense rhyolitic volcanism associated with flood basalt magmatism and the initiation of the Snake River Plain–Yellowstone trend. *Geosphere*, 12(1), 58–113. <https://doi.org/10.1130/GES01162.1>
- Colby, T., Northrup, C., Schmitz, M., & Snyder, W. (2018). *Correlation of the Black Rock and Olds Ferry arc terranes? New detrital zircon from the Boulder Creek Beds in the Jackson Mountains, NW Nevada, USA*. <https://doi.org/10.1130/abs/2018AM-323978>
- Cox, D. P., & Singer, D. A. (1986). *Mineral Deposit Models*. <https://pubs.usgs.gov/bul/b1693/html/bullfrms.htm>
- Cruz, M., & Streck, M. (2018). *Report on geologic mapping of Calamity Butte 7.5" quadrangle, Grant and Harney Counties, Oregon, USA* (Unpublished). Portland State University Department of Geology. [https://ngmdb.usgs.gov/Prodesc/proddesc\\_109645.htm](https://ngmdb.usgs.gov/Prodesc/proddesc_109645.htm)

- Cummings, M. L., Evans, J. G., Ferns, M. L., & Lees, K. R. (2000). Stratigraphic and structural evolution of the middle Miocene synvolcanic Oregon-Idaho graben. *GSA Bulletin*, 112(5), 668–682. [https://doi.org/10.1130/0016-7606\(2000\)112<668:SASEOT>2.0.CO;2](https://doi.org/10.1130/0016-7606(2000)112<668:SASEOT>2.0.CO;2)
- Darold, A. (2013). Upper mantle seismic structure beneath the Pacific Northwest\_ A plume-triggered delamination origin for the Columbia River flood basalt eruptions. *Earth and Planetary Science Letters*, 11.
- Debon, F., & Le Fort, P. (1988). A cationic classification of common plutonic rocks and their magmatic associations: Principles, method, applications. *Bulletin de Minéralogie*, 111(5), 493–510. <https://doi.org/10.3406/bulmi.1988.8096>
- Dorsey, R., & LaMaskin, T. (2008). Mesozoic collision and accretion of oceanic terranes in the Blue Mountains Province of northeastern Oregon: New insights from the stratigraphic record. *Arizona Geol. Soc. Dig.*, 22.
- Dunn, T., & Sen, C. (1994). Mineral/matrix partition coefficients for orthopyroxene, plagioclase, and olivine in basaltic to andesitic systems: A combined analytical and experimental study. *Geochimica et Cosmochimica Acta*, 58(2), 717–733. [https://doi.org/10.1016/0016-7037\(94\)90501-0](https://doi.org/10.1016/0016-7037(94)90501-0)
- Eby, G. N. (1992). Chemical subdivision of the A-type granitoids: Petrogenetic and tectonic implications. *Geology*, 20(7), 641. [https://doi.org/10.1130/0091-7613\(1992\)020<0641:CSOTAT>2.3.CO;2](https://doi.org/10.1130/0091-7613(1992)020<0641:CSOTAT>2.3.CO;2)
- Elliott, T. (2004). Tracers of the Slab. In *Inside the Subduction Factory* (pp. 23–45). American Geophysical Union (AGU). <https://doi.org/10.1029/138GM03>

- Ernst, R. E., Liikane, D. A., Jowitt, S. M., Buchan, K. L., & Blanchard, J. A. (2019). A new plumbing system framework for mantle plume-related continental Large Igneous Provinces and their mafic-ultramafic intrusions. *Journal of Volcanology and Geothermal Research*, 384, 75–84. <https://doi.org/10.1016/j.jvolgeores.2019.07.007>
- Fruchter, J. S., & Baldwin, S. F. (1975). Correlations between Dikes of the Monument Swarm, Central Oregon, and Picture Gorge Basalt Flows. *GSA Bulletin*, 86, 3. [https://doi.org/10.1130/0016-7606\(1975\)86<514:CBDOTM>2.0.CO;2](https://doi.org/10.1130/0016-7606(1975)86<514:CBDOTM>2.0.CO;2)
- Gerlach, D., Lallemand, H., & Leeman, W. (1981). An island arc origin for the Canyon Mountain ophiolite complex, eastern Oregon, U.S.A. *Earth and Planetary Science Letters*, 53, 255–265. [https://doi.org/10.1016/0012-821X\(81\)90158-8](https://doi.org/10.1016/0012-821X(81)90158-8)
- Glazner, A., Bartley, J., & Coleman, D. (2019). A More Informative Way to Name Plutonic Rocks. *GSA Today*, 29(2), 4–10. <https://doi.org/10.1130/GSATG384A.1>
- Glen, J. M. G., & Ponce, D. A. (2002). Large-scale fractures related to inception of the Yellowstone hotspot. *Geology*, 30(7), 647–650. [https://doi.org/10.1130/0091-7613\(2002\)030<0647:LSFRTI>2.0.CO;2](https://doi.org/10.1130/0091-7613(2002)030<0647:LSFRTI>2.0.CO;2)
- Green, T. H. (1994). Experimental studies of trace-element partitioning applicable to igneous petrogenesis—Sedona 16 years later. *Chemical Geology*, 117(1), 1–36. [https://doi.org/10.1016/0009-2541\(94\)90119-8](https://doi.org/10.1016/0009-2541(94)90119-8)
- Gualda, G. A. R., & Ghiorso, M. S. (2015). *MELTS\_Excel: A Microsoft Excel-based MELTS interface for research and teaching of magma properties and evolution* (1.0.x) [Microsoft Excel]. <https://melts.ofm-research.org/excel.html>

Hart, S. R., & Dunn, T. (1993). Experimental cpx/melt partitioning of 24 trace elements.

*Contributions to Mineralogy and Petrology*, 113(1), 1–8.

<https://doi.org/10.1007/BF00320827>

Henry, C. D., Castor, S. B., Starkel, W. A., Ellis, B. S., Wolff, J. A., Laravie, J. A.,

McIntosh, W. C., & Heizler, M. T. (2017a). Geology and evolution of the

McDermitt caldera, northern Nevada and southeastern Oregon, western USA.

*Geosphere*, 13(4), 1066–1112. <https://doi.org/10.1130/GES01454.1>

Henry, C. D., Castor, S. B., Starkel, W. A., Ellis, B. S., Wolff, J. A., Laravie, J. A.,

McIntosh, W. C., & Heizler, M. T. (2017b). Geology and evolution of the

McDermitt caldera, northern Nevada and southeastern Oregon, western USA.

*Geosphere*, 13(4), 1066–1112. <https://doi.org/10.1130/GES01454.1>

Hill, R. I., Campbell, I. H., Davies, G. F., & Griffiths, R. W. (1992). Mantle Plumes and

Continental Tectonics. *Science*, 256(5054), 186–193.

<https://doi.org/10.1126/science.256.5054.186>

Hooper, P. R. (1988). Crystal Fractionation and Recharge (RFC) in the American Bar

Flows of the Innaha Basalt, Columbia River Basalt Group. *Journal of Petrology*,

29(5), 1097–1118. <https://doi.org/10.1093/petrology/29.5.1097>

Hooper, P. R., Kleck, W. D., Knowles, C. R., Reidel, S. P., & Theissen, R. L. (1984).

Innaha Basalt, Columbia River Basalt Group. *Journal of Petrology*, 25(2), 473–500.

<https://doi.org/10.1093/petrology/25.2.473>

Horton, J. D. (2017). *The State Geologic Map Compilation (SGMC) Geodatabase of the*

*Conterminous United States* [dataset]. U.S. Geological Survey.

<https://doi.org/10.5066/F7WH2N65>

- Hu, J.-H., Liu, J.-W., Song, T., & Shi, B.-S. (2020). Magma Plumbing System of Emeishan Large Igneous Province at the End-Permian: Insights from Clinopyroxene Compositional Zoning and Thermobarometry. *Minerals*, 10(11), Article 11. <https://doi.org/10.3390/min10110979>
- Humphreys, E. (2006). Relation of flat subduction to magmatism and deformation in western USA. *Geochimica Et Cosmochimica Acta - GEOCHIM COSMOCHIM ACTA*, 70. <https://doi.org/10.1016/j.gca.2006.06.548>
- Isom, S., & Streck, M. (2017). *Report on Geologic Mapping of Telephone Butte Quadrangle, Harney County, Oregon, USA*. Portland State University Department of Geology. [https://ngmdb.usgs.gov/Prodesc/proddesc\\_109646.htm](https://ngmdb.usgs.gov/Prodesc/proddesc_109646.htm)
- Jones Crafford, A. E. (2008). Paleozoic tectonic domains of Nevada: An interpretive discussion to accompany the geologic map of Nevada. *Geosphere*, 4(1), 260–291. <https://doi.org/10.1130/GES00108.1>
- Kamenov, G. D., Saunders, J. A., Hames, W. E., & Unger, D. L. (2007). Magmas as sources for gold in middle Miocene epithermal deposits of the northern Great Basin, United States: Evidence from Pb isotope compositions of native gold. *Economic Geology*, 102(7), 1191–1195. <https://doi.org/10.2113/gsecongeo.102.7.1191>
- Le Bas, M. J. L., Le Maitre, R. W., Streckeisen, A., Zannetin, B., & IUGS Subcommittee on the Systematics of Igneous Rocks. (1986). A Chemical Classification of Volcanic Rocks Based on the Total Alkali-Silica Diagram. *Journal of Petrology*, 27(3), 745–750. <https://doi.org/10.1093/petrology/27.3.745>

Machette, M. N., Haller, K. M., Dart, R. L., & Rhea, S. B. (2003). Quaternary fault and fold database of the United States. *Open-File Report*, Article 2003–417.

<https://doi.org/10.3133/ofr03417>

Mahood, G. A., & Benson, T. R. (2017). Using  $^{40}\text{Ar}/^{39}\text{Ar}$  ages of intercalated silicic tuffs to date flood basalts: Precise ages for Steens Basalt Member of the Columbia River Basalt Group. *Earth and Planetary Science Letters*, 459, 340–351.

<https://doi.org/10.1016/j.epsl.2016.11.038>

McClaughry, J. D., Ferns, M. L., Streck, M. J., Patridge, K. A., & Gordon, C. L. (2009). Paleogene calderas of central and eastern Oregon: Eruptive sources of widespread tuffs in the John Day and Clarno Formations. In J. E. O'Connor, R. J. Dorsey, & I. P. Madin, *Volcanoes to Vineyards*. Geological Society of America.

[https://doi.org/10.1130/2009.fld015\(20\)](https://doi.org/10.1130/2009.fld015(20))

McClaughry, J., Duda, C., & Ferns, M. (2019). *Geologic map of the Poison Creek and Burns 7.5' quadrangles, Harney County, Oregon*. Oregon Department of Geology and Mineral Industries.

McClaughry, J., Niewendorp, C., Franczyk, J., Duda, C., & Madin, I. (2021). *Mineral Information Layer for Oregon, release 3 [MILO-3]*.

McKenzie, D., & O'Nions, R. K. (1991). Partial Melt Distributions from Inversion of Rare Earth Element Concentrations. *Journal of Petrology*, 32(5), 1021–1091.

<https://doi.org/10.1093/petrology/32.5.1021>

Middlemost, E. A. K. (1994). Naming materials in the magma/igneous rock system.

*Earth-Science Reviews*, 37(3–4), 215–224. [https://doi.org/10.1016/0012-](https://doi.org/10.1016/0012-8252(94)90029-9)

[8252\(94\)90029-9](https://doi.org/10.1016/0012-8252(94)90029-9)

- Misseri, M., & Boudier, F. (1985). Structures in the Canyon Mountain Ophiolite indicate an island-arc intrusion. *Tectonophysics*, *120*(3–4), 191–209.  
[https://doi.org/10.1016/0040-1951\(85\)90051-4](https://doi.org/10.1016/0040-1951(85)90051-4)
- Moore, N. E., Grunder, A. L., & Bohrsen, W. A. (2018). The three-stage petrochemical evolution of the Steens Basalt (southeast Oregon, USA) compared to large igneous provinces and layered mafic intrusions. *Geosphere*, *14*(6), 2505–2532.  
<https://doi.org/10.1130/GES01665.1>
- Moore, N. E., Grunder, A. L., Bohrsen, W. A., Carlson, R. W., & Bindeman, I. N. (2020). Changing Mantle Sources and the Effects of Crustal Passage on the Steens Basalt, SE Oregon: Chemical and Isotopic Constraints. *Geochemistry, Geophysics, Geosystems*, *21*(8), e2020GC008910. <https://doi.org/10.1029/2020GC008910>
- Morriss, M. C., Karlstrom, L., Nasholds, M. W. M., & Wolff, J. A. (2020). The Chief Joseph dike swarm of the Columbia River flood basalts, and the legacy data set of William H. Taubeneck. *Geosphere*, *16*(4), 1082–1106.  
<https://doi.org/10.1130/GES02173.1>
- Muirhead, J. D., Airoidi, G., Rowland, J. V., & White, J. D. L. (2011). Interconnected sills and inclined sheet intrusions control shallow magma transport in the Ferrar large igneous province, Antarctica. *Geological Society of America Bulletin*, *124*(1–2), 162.
- Phillips, J. D., Duval, J. S., & Ambroziak, R. A. (1993). National geophysical data grids; gamma-ray, gravity, magnetic, and topographic data for the conterminous United States. In *Data Series* (9). U.S. Geological Survey. <https://doi.org/10.3133/ds9>

- Pirajno, F. (2000). Intracontinental Magmatism, Anorogenic Metamorphism, Ore Systems and Mantle Plumes. *Ore Deposits and Mantle Plumes*, 291–321.
- Ponce, D. A., & Glen, J. M. G. (2002). Relationship of Epithermal Gold Deposits to Large Scale Fractures in Northern Nevada. *Economic Geology*, 97, 3–9.
- Ponce, D., & Glen, J. (2001). Large-scale Crustal Features, Epithermal Gold Deposits, and the Yellowstone Hotspot, Western U.S. *AGU Fall Meeting Abstracts*.
- Reidel, S. P., Camp, V. E., Ross, M. E., Wolff, J. A., Martin, B. S., Tolan, T. L., & Wells, R. E. (2013). *The Columbia River Flood Basalt Province*. Geological Society of America. <https://doi.org/10.1130/SPE497>
- Roback, R. C., Meulen, D. B. V., King, H. D., Plouff, D., Munts, S. R., & Willett, S. L. (1987). Mineral resources of the Pueblo Mountains Wilderness Study Area, Harney County, Oregon, and Humboldt County, Nevada. In *Bulletin (1740-B)*. U.S. G.P.O., <https://doi.org/10.3133/b1740B>
- Sarewitz, D. (1983). Seven Devils terrane: Is it really a piece of Wrangellia? *Geology*, 11(11), 634–637. [https://doi.org/10.1130/0091-7613\(1983\)11<634:SDTIIR>2.0.CO;2](https://doi.org/10.1130/0091-7613(1983)11<634:SDTIIR>2.0.CO;2)
- Schulz, K., Chandler, V., Nicholson, S., Piatak, N., Seal, R., Woodruff, L., & Zientek, M. (2010). *Magmatic-Sulfide-Rich Nickel-Copper Deposits Related to Picrite and (or) Tholeiitic Basalt Dike-Sill Complexes: A preliminary Deposit Model* (Open-File Report 2010–1179; Open-File Report, p. 31). United States Geologic Survey. <https://pubs.usgs.gov/of/2010/1179/pdf/ofr2010-1179.pdf>
- Schwartz, J. J., Snoke, A. W., Cordey, F., Johnson, K., Frost, C. D., Barnes, C. G., LaMaskin, T. A., & Wooden, J. L. (2011). Late Jurassic magmatism,

metamorphism, and deformation in the Blue Mountains Province, northeast Oregon. *Geological Society of America Bulletin*, 123(9–10), 2083–2111.

<https://doi.org/10.1130/B30327.1>

Schweitzer, P. N. (2020). *Isostatic residual gravity anomaly data grid for the conterminous US*. U.S. Geological Survey.

<https://mrdata.usgs.gov/metadata/usgraviso.faq.html#who>

Shellnutt, J. G., Ma, G. S.-K., & Qi, L. (2015). Platinum-group elemental chemistry of the Baima and Taihe Fe–Ti oxide bearing gabbroic intrusions of the Emeishan large igneous province, SW China. *Geochemistry*, 75(1), 35–49.

<https://doi.org/10.1016/j.chemer.2014.06.002>

Sheth, H. (2016). Giant plagioclase basalts: Continental flood basalt–induced remobilization of anorthositic mushes in a deep crustal sill complex. *GSA Bulletin*, 128(5–6), 916–925. <https://doi.org/10.1130/B31404.1>

Sheth, H. C. (2007). ‘Large Igneous Provinces (LIPs)’: Definition, recommended terminology, and a hierarchical classification. *Earth-Science Reviews*, 85(3–4), 117–124. <https://doi.org/10.1016/j.earscirev.2007.07.005>

Smith, W., & Maier, W. (2021a). The geotectonic setting, age and mineral deposit inventory of global layered intrusions. *Earth-Science Reviews*, 220, 103736.

<https://doi.org/10.1016/j.earscirev.2021.103736>

Smith, W., & Maier, W. (2021b). The geotectonic setting, age and mineral deposit inventory of global layered intrusions. *Earth-Science Reviews*, 220, 103736.

<https://doi.org/10.1016/j.earscirev.2021.103736>

- Soderberg, E., & Wolff, J. (2023). Mantle source lithologies for the Columbia River flood basalt province. *Contributions to Mineralogy and Petrology*, 178. <https://doi.org/10.1007/s00410-023-01993-2>
- Stefano, C. J., Mukasa, S. B., & Cabato, J. A. (2019). Elemental abundance patterns and Sr-, Nd- and Hf-isotope systematics for the Yellowstone hotspot and Columbia River flood basalts: Bearing on petrogenesis. *Chemical Geology*, 513, 44–53. <https://doi.org/10.1016/j.chemgeo.2019.03.012>
- Steiger, R. H., & Jäger, E. (1977). Subcommittee on geochronology: Convention on the use of decay constants in geo- and cosmochemistry. *Earth and Planetary Science Letters*, 36(3), 359–362. [https://doi.org/10.1016/0012-821X\(77\)90060-7](https://doi.org/10.1016/0012-821X(77)90060-7)
- Steiner, A., & Streck, M. J. (2019). Voluminous and compositionally diverse, middle Miocene Strawberry Volcanics of NE Oregon: Magmatism cogenetic with flood basalts of the Columbia River Basalt Group. In M. P. Poland, M. O. Garcia, V. E. Camp, & A. Grunder, *Field Volcanology: A Tribute to the Distinguished Career of Don Swanson*. Geological Society of America. [https://doi.org/10.1130/2018.2538\(03\)](https://doi.org/10.1130/2018.2538(03))
- Streck, M. J., Ferns, M. L., & McIntosh, W. (2015). Large, persistent rhyolitic magma reservoirs above Columbia River Basalt storage sites: The Dinner Creek Tuff Eruptive Center, eastern Oregon. *Geosphere*. <https://doi.org/10.1130/GES01086.1>
- Streck, M. J., Fredenberg, L. J., Fox, L. M., Cahoon, E. B., & Mass, M. J. (2023). Province-Wide Tapping of a Shallow, Variably Depleted, and Metasomatized Mantle to Generate Earliest Flood Basalt Magmas of the Columbia River Basalt, Northwestern USA. *Minerals*, 13(12), 1544. <https://doi.org/10.3390/min13121544>

- Streck, M., Swenton, V., McIntosh, W., Ferns, M., & Heizler, M. (2023). Columbia River Rhyolites: Age-Distribution Patterns and Their Implications for Arrival, Location, and Dispersion of Continental Flood Basalt Magmas in the Crust. *Geosciences*, *13*, 46. <https://doi.org/10.3390/geosciences13020046>
- Sun, S. -s., & McDonough, W. F. (1989). Chemical and isotopic systematics of oceanic basalts: Implications for mantle composition and processes. *Geological Society, London, Special Publications*, *42*(1), 313–345. <https://doi.org/10.1144/GSL.SP.1989.042.01.19>
- Sweeten, R., Streck, M. J., Wolff, J. A., & Muirhead, J. D. (2022, October 10). *The Picture Gorge and Steens Basalt: A tale of two magmatic systems*. GSA Connects 2022 meeting in Denver, Colorado. <https://gsa.confex.com/gsa/2022AM/webprogram/Paper383922.html>
- Thieme, C., Streck, M. J., Steiner, A., & Sweeten, R. (2021, October 12). *A newly documented major mid-Miocene rhyolite field associated with Columbia River Basalt Magmatism, eastern Oregon, USA: The Strawberry Rhyolites*. GSA Connects 2021 in Portland, Oregon. <https://gsa.confex.com/gsa/2021AM/meetingapp.cgi/Paper/370252>
- Thomas, R., & Sears, J. W. (2007). Extraordinary Middle Miocene crustal disturbance in southwest Montana: Birth record of the Yellowstone hot spot? *Northwest Geology*, *36*, 133333–142.
- Walker, G. W., & Repenning, C. A. (1965). Reconnaissance geologic map of the Adel quadrangle, Lake, Harney, and Malheur Counties, Oregon. *IMAP*, Article 446. <https://doi.org/10.3133/i446>

- Wallace, R. E. (1956). *Reconnaissance geologic map of the Izee and Logdell quadrangles, Oregon*. <https://doi.org/10.3133/mf82>
- Watt, J. T., Glen, J. M. G., John, D. A., & Ponce, D. A. (2007). Three-dimensional geologic model of the northern Nevada rift and the Beowawe geothermal system, north-central Nevada. *Geosphere*, 3(6), 667–682. <https://doi.org/10.1130/GES00100.1>
- Wells, R. E., & McCaffrey, R. (2013). Steady rotation of the Cascade arc. *Geology*, 41(9), 1027–1030. <https://doi.org/10.1130/G34514.1>
- Wolff, J. A., Ramos, F. C., Hart, G. L., Patterson, J. D., & Brandon, A. D. (2008). Columbia River flood basalts from a centralized crustal magmatic system. *Nature Geoscience*, 1(3), 177–180. <https://doi.org/10.1038/ngeo124>
- Zhang, M., O'Reilly, S. Y., Wang, K.-L., Hronsky, J., & Griffin, W. L. (2008). Flood basalts and metallogeny: The lithospheric mantle connection. *Earth-Science Reviews*, 86(1–4), 145–174. <https://doi.org/10.1016/j.earscirev.2007.08.007>
- ZOBACK, M. L., McKEE, E. H., BLAKELY, R. J., & THOMPSON, G. A. (1994). The northern Nevada rift: Regional tectono-magmatic relations and middle Miocene stress direction. *GSA Bulletin*, 106(3), 371–382. [https://doi.org/10.1130/0016-7606\(1994\)106<0371:TNNRRT>2.3.CO;2](https://doi.org/10.1130/0016-7606(1994)106<0371:TNNRRT>2.3.CO;2)

## APPENDIX

The following supplemental files accompany this thesis:

“Geochemical Database.xlsx”

This excel file is the geochemical database used for this study. This geochemical database contains location (latitude/longitude in decimal degrees), data source, major element measurements using XRF, trace element measurements using ICPMS, as well as select trace and major element ratios. All major elements have been normalized on a volatile free basis. Some geochemical units have been renamed or simplified to maintain data integrity.

File Type: Excel Workbook

File Name: GeochemicalDatabase.xlsx

File Size: 713 kB

Required Software: Microsoft Excel